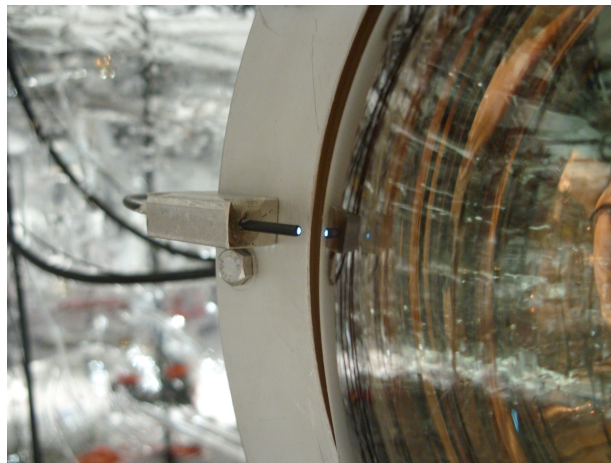# Analysis of the GERDA Muon Veto — First Light

Dissertation

der Mathematisch-Naturwissenschaftlichen Fakultät
der Eberhard Karls Universität Tübingen
zur Erlangung des Grades eines
Doktors der Naturwissenschaften
(Dr. rer. nat.)

vorgelegt von
Dipl. Phys. Florian Ritter
aus Tübingen

Tübingen
2011

EBERHARD KARLS
UNIVERSITÄT
TÜBINGEN

Analysis of the GERDA Muon Veto — First Light

Das Experiment GERmanium Detector Array (GERDA) sucht nach dem neutrinolosen doppelten Betazerfall von ^{76}Ge. Wenn Neutrinos Majorana-Teilchen sind, dann sollte dieser sehr seltene Prozess der schwachen Wechselwirkung stattfinden. Bis jetzt konnte nur der doppelte Betazerfall mit Aussendung von zwei Neutrinos beobachtet werden, dies jedoch in mehreren Isotopen. Einzig ein Teil der Heidelberg-Moskau Kollaboration behauptet, den neutrinolosen doppelten Betazerfall beobachtet zu haben. Abgesehen davon beträgt die momentan beste untere Grenze der Halbwertszeit des neutrinolosen doppelten Betazerfalls von ^{76}Ge $T_{1/2}^{0\nu} > 1.9 \cdot 10^{25}$ y [KK01b].

GERDA hat vor kurzem mit den ersten Messungen mit drei in ^{76}Ge angereicherten Detektoren angefangen. Sobald etwa 15 (kg y) an Daten gesammelt wurden, sollte GERDA die behauptete Beobachtung des Zerfalls überprüfen können. In einer zweiten Phase wird die Untergrundrate um einen weiteren Faktor 10 gesenkt und die Masse an ^{76}Ge erhöht werden, um die untere Grenze für die Halbwertszeit auf $T_{1/2} > 2 \cdot 10^{26}$ y zu erhöhen.

Um die benötigte Sensitivität zu erreichen, muss der Untergrund auf eine Rate von $10^{-3} \frac{\text{Ereignissen}}{\text{keV} \cdot \text{kg} \cdot \text{Jahr}}$ reduziert werden. Dies wird durch verschiedene Maßnahmen zur Untergrundunterdrückung bzw. -identifizierung wie zum Beispiel Pulsform-Analyse und ein aktives Myonenveto erreicht werden.

In dieser Arbeit werden die Datennahme und die ersten Daten des Cherenkov Myonveto Detektors präsentiert. Verschiedene Analysealgorithmen wurden entwickelt und werden ebenfalls vorgestellt. Von den ersten Daten wurde eine Myondetektionseffizienz abgeleitet und eine offline-Schwelle für die Myonenidentifikation definiert. Zusätzlich wird ein Kalibrationssystem für den Myonendetektor vorgestellt.

Analysis of the GERDA Muon Veto — First Light

The experiment GERmanium Detector Array (GERDA) is searching for the neutrinoless double beta decay of ^{76}Ge. If the neutrino is a Majorana particle, this very rare process of the weak interaction should be observed. Up to now, the double beta decay with emission of two neutrinos was found in several isotopes. Only a part of the Heidelberg-Moscow experiment claims to have observed the neutrinoless double beta decay. Despite the claim, the currently best limit for neutrinoless double beta decay of ^{76}Ge is $T_{1/2}^{0\nu} > 1.9 \cdot 10^{25}$ y [KK01b].

GERDA just started a physics run with three germanium diodes enriched in ^{76}Ge. As soon as an exposure of 15 (kg y) is reached, GERDA should be able to test the claim. In a second phase, the background of GERDA will be reduced by an additional factor of 10 and the ^{76}Ge mass will be increased to push the limit for the halflife time to $T_{1/2} > 2 \cdot 10^{26}$ y.

To reach the needed sensitivity, the background has to be reduced to a rate of $10^{-3} \frac{\text{counts}}{\text{keV} \cdot \text{kg} \cdot \text{year}}$. This will be achieved through different background reduction (and identification) techniques, like pulse shape analysis or an active muon veto.

In this work, the data acquisition and first data of the Cherenkov muon veto are presented. Different analysis tools have been developed and will be shown. A muon detection efficiency is derived from the very first data, and an offline muon cut threshold is presented. In addition, a calibration system for the muon detector system will be presented.

Contents

Chapter 1

Introduction

In the year 1930, Wolfgang Pauli introduced a hypothetical neutral particle to save the law of energy conservation in the beta decay. Since then, experimental physicists built up huge detectors, first to detect these particles (the *"neutrinos"*), then to reveal their properties. Nowadays, it is well established, that there are three neutrino flavor eigenstates (ν_e, ν_μ and ν_τ), which become measurable as soon as a neutrino interacts with matter. But the neutrinos propagate as their mass eigenstates ν_1, ν_2 and ν_3, while the flavor eigenstates are superpositions of the mass eigenstates. This leads to flavor transitions, so called *neutrino oscillation*. Here, a huge effort is done to precisely measure the three different mixing angles.

But still, several properties of the neutrinos are unknown. Mid of September 2011 measurements of the OPERA experiment suggested that neutrinos are traveling with a velocity at 20 ppm **above** the speed of light. This intriguing result, if confirmed by other experiments, would have a very huge impact on the physical view of the world. At the moment, the OPERA collaboration itself is not convinced fully by the result of their measurement, thus, the next years are expected to be very exciting.

Recently (November 2011), the DoubleChooz collaboration presented their preliminary result on the mixing angle θ_{13} on the LowNu workshop in Seoul. Now, three experiments (T2K, MINOS and DoubleChooz) have data indicating $\theta_{13} > 0$.

Despite these new turns in neutrino physics, there are still open questions concerning the neutrino. For example, their mass is not measured, only upper bounds are given. And in addition, it is not known, if neutrinos are Dirac particles or Majorana particles. If they were Dirac particles, the neutrino and its anti-particle would be two distinguishable particles. But if they are Majorana particles, there is no difference in the two particles. This would need an extension of the standard model of particle physics, as each particle is assumed to have their specific anti-particle (only for the photon, there exists no "anti-photon").

The experiment GERDA is built to test the hypothesis of Majorana neutrinos. For several isotopes as for example ^{76}Ge, which is used in GERDA, the standard single beta decay is energetically forbidden, thus, these isotopes can only decay by undergoing a double beta decay. If neutrinos are Majorana particles, the *neutrinoless double beta decay* ($0\nu\beta\beta$) should be possible. In that case, the neutrino from one beta decay could trigger the other decay while being absorbed by a neutron. Thus, only the two produced electrons would escape the nucleus. This results in a peak at the endpoint of the double beta decay spectrum, which is at $Q_{\beta\beta} = 2039$ keV for ^{76}Ge. As this is a very rare decay (the best limit up to now is $T_{1/2}^{0\nu} > 1.9 \cdot 10^{25}$ y [KK01b]), one needs as much ^{76}Ge

as possible, a run time of the experiment, which is as long as possible and a background, which is as low as possible. To reduce the background, GERDA was built in one of the world's largest underground laboratories, the LNGS in Italy. The rock coverage of 1400 m reduces the muon flux from 100 - 200 $\mu/(\text{m}^2 \text{ s})$ to $1 \mu/(\text{m}^2 \text{ h})$. In addition, GERDA also uses an innovative shielding design, using mainly low-Z material close to the detectors. This helps in reducing the amount of signals due to the remaining muons. Also, pulse shape analysis helps in reducing background events, since $0\nu\beta\beta$ events would produce a different pulse shape as most of the background events. Nevertheless, the background induced by the remaining muons is still an issue, especially if one wants to increase the sensitivity of the experiment. Therefore, the GERDA muon veto was developed. It consists of a water Cherenkov detector (a water tank surrounding the actual experiment, equipped with 66 light detectors) and 36 plastic scintillator panels covering a possible "blind spot" of the Cherenkov veto.

This work was mainly focused on the development of a data acquisition system creating a trigger for the signals of the muon veto detectors and reading out the data. A second focus was on the first analysis of the recorded events. Therefore, a conversion tool was developed to "translate" the data from the DAQ system to a format readable for the analysis. As the experiment is planned to run for several years, also a calibration system was designed and installed during this work.

Some terms are defined here:

- **PMT**: photomultiplier tube, the light detector.

- **photon**: optical photon, if not further specified.

- **photoelectron (p.e.)**: electronic response of a PMT, if one photon reaching the photo-cathode has triggered an avalanche of electrons towards the anode. The number of photo-electrons is proportional to the number of photons, which reached the photocathode, but it is not equal the amount of photons, due to quantum efficiency and other losses.

Chapter 2

Theory

This chapter presents the theoretical background of GERDA. In the first part, a short overview about the *Standard Model of Particle Physics* (SM) is given, since this model was tested several times, and up to now, it is the most comprehensive description of particle physics. Nevertheless, a lot of observations in the universe lead to the conclusion, that the SM is not complete. For example, in the SM, neutrinos do not have a mass, but several experiments could independently prove the existence of neutrino mixing, which is only possible, if neutrinos do have a mass. Also, the existence of neutrinoless double beta decay ($0\nu\beta\beta$) would mean that the lepton number is not conserved. The observation of $0\nu\beta\beta$ is the aim of GERDA. Also, the SM fails in the explanation of the dark matter and dark energy content of the universe. Several theories are trying to expand the SM to deal with that. The supersymmetry (SUSY) is one of these theories. There, each particle gets its own supersymmetric partner, the superpartners of fermions are bosons and vice versa.

Neutrinos are the topic of the second part of this chapter. These elementary particles were predicted in 1930 by Wolfgang Pauli in a letter to his "radioactive friends" in Tübingen, and 26 years later, they were experimentally detected. Although a vast number of experiments have been performed to discover all secrets of the neutrinos, still, these "ghost particles" as frequently dubbed by the media are a mystery themselves. The goal of GERDA is to discover $0\nu\beta\beta$, or at least push the lifetime limit further; a detection of this decay would answer a question, which is almost as old as the theory of the neutrinos: are neutrinos and anti-neutrinos the same particles or not?

The third part is related to the GERDA muon veto. This "detector around the main detector" is needed to identify muons, which otherwise would contribute to the background of the GERDA experiment and therefore might limit its sensitivity. The origins of muons will be explained, as well as the detection principle, the Cherenkov effect.

2.1 The standard model of particle physics

The *Standard Model of Particle Physics* (SM) describes the known elementary particles and the interactions between them. It was developed in the middle of the last century, and describes electromagnetic, strong and weak interaction. A unified description of electromagnetic and weak interaction can also be found in the SM. Only the gravitation still refuses to get into this picture. The SM explains the known part of the universe on a particle scale, it describes 12 elementary particles with spin 1/2, the so-called fermions (three families with two particles in the quark- and

the same in the lepton sector), their anti-particles and the gauge bosons, the force carriers with spin 1. In fig. 1, all elementary particles are listed.

Fermions
matter constituents
spin = 1/2, 3/2, 5/2, ...

Leptons spin =1/2

Flavor		Mass GeV/c^2	Electric charge
ν_L	lightest neutrino*	$(0-0.13) \times 10^{-9}$	0
e	electron	0.000511	−1
ν_M	middle neutrino*	$(0.009-0.13) \times 10^{-9}$	0
μ	muon	0.106	−1
ν_H	heaviest neutrino*	$(0.04-0.14) \times 10^{-9}$	0
τ	tau	1.777	−1

Quarks spin =1/2

Flavor		Approx. Mass GeV/c^2	Electric charge
u	up	0.002	2/3
d	down	0.005	−1/3
c	charm	1.3	2/3
s	strange	0.1	−1/3
t	top	173	2/3
b	bottom	4.2	−1/3

Bosons
force carriers
spin = 0, 1, 2, ...

Unified Electroweak spin = 1

Name	Mass GeV/c^2	Electric charge
γ photon	0	0
W$^-$	80.39	−1
W$^+$ W bosons	80.39	+1
Z^0 Z boson	91.188	0

Strong (color) spin =1

Name	Mass GeV/c^2	Electric charge
g gluon	0	0

Figure 1: Lepton and quark families. For clarity reasons, the associated anti-particles are left out. Here, the neutrinos are labeled $\nu_{L,M,H}$ to account for the mass eigenstates (see Sec. 2.2). Fig. from [CPE].

2.2 The neutrino

As mentioned above, in a letter to his "radioactive friends" in Tübingen in the year 1930, Wolfgang Pauli postulated the existence of an additional neutral particle [1]. In that time, only the existence of electrons and protons was confirmed. The continuous spectrum of the electrons emitted in the β decay could not be explained, since for such a two body interaction, one would expect to have one discrete line. This was the reason for Wolfgang Pauli to introduce a new particle. Such

---

[1] an English translation of the letter can be found here:
http://lappweb.in2p3.fr/neutrinos/aplettre.html

a light, neutral and only weakly interacting particle would carry away the "missing energy" and thus save the energy conservation principle just because it is invisible for the detectors. Pauli himself called this particle "neutron". When the "real" neutron was detected, it was clear, that the particle postulated by Pauli has to be a different neutral particle. Enrico Fermi then called it "neutrino" (ital. "the small neutron"). But the prediction of Pauli was, that the neutrino never could be detected, as its cross section with standard matter is so low, that it would be too unlikely that interaction with matter takes place. Thus, he thought of it as a working hypothesis. It took 26 years, when Clyde L. Cowan and Frederick Reines could prove the existence of the neutrino in their *Poltergeist* experiment in 1956. But still, several properties of the neutrino could not be determined. In the 1960s, Raymond Davis Jr. built up an experiment to measure the neutrino flux coming from the sun [Dav02]. As nuclear fusion takes place in the core of the sun and transitions from protons to neutrons by inverse beta decay are needed, neutrinos should be released and therefore should be detected on earth. The ambitious Homestake experiment (also known as *Davis experiment*) was located around 1500 m underground, it consisted of 615 t tetrachlorethylen. In this huge volume ($380\,\mathrm{m}^3$), it should happen that neutrinos from the sun are captured on chlorine atoms, leading to a production of argon ($\nu_e + {}^{37}Cl \rightarrow {}^{37}Ar + e$). This argon isotope is radioactive, decaying back to chlorine with a half life time of 35 days. Thus, the argon isotopes can be trapped and then their decay may be detected. As the cross section of neutrinos on matter is very small, it was expected that the count rate is very low, in the order of 2.5 SNU (*Solar Neutrino Units*; events per second and 10^{36} atoms in the detector) [MP]. This translates to around 2 events per day in the Homestake experiment. But the published values were only 1/3 of the theoretically expected values calculated from the assumptions about the fusion reactions in the sun. Thus, either the energy production in the sun was different to the theoretical models, or the experiment had a much lower efficiency in detecting neutrinos. As several other experiments also measured a deficit later, this problem was soon called the *solar neutrino problem*. In 1998, the experiments Gallex, SNO and Super-Kamiokande could solve this problem with a strong evidence for neutrino oscillations. This means, a neutrino emitted in the sun as electron-neutrino has a 2/3 probability to be detected in an earthbound detector as a muon- or tau-neutrino. In 2001, the SNO experiment could give a first clear evidence that neutrinos oscillate by measuring the ν_e flux which is reduced and the flux of all ν's, which is not reduced. But neutrino oscillation only can occur, if neutrino have mass. This is in contradiction to the SM, where neutrinos are massless. Nevertheless, the mass of neutrinos has to be small. To explain neutrino oscillations, the idea is to have mass ($\nu_{1,2,3}$) and flavor ($\nu_{e,\mu,\tau}$) eigenstates. Each flavor eigenstate is a linear combination of the three mass eigenstates and vice versa. Emitted as one flavor eigenstate, the propagation is described as propagation of the mass eigenstates, but detection is only possible for flavor eigenstates.

The *Pontecorvo-Maki-Nakagawa-Sakata matrix* (PMNS matrix) describes the neutrino mixing. Equation 2.1 shows the mathematical description of the linear combination. Here, $|\nu_\alpha\rangle$ are the flavor eigenstates, and $|\nu_i\rangle$ are the mass eigenstates.

$$|\nu_\alpha\rangle = \sum_i U_{\alpha i}|\nu_i\rangle \tag{2.1}$$

One can think of the neutrino mixing as a three-dimensional rotation of the eigenvector. Thus, one has to define three rotation angles θ_{12}, θ_{23} and θ_{13}. In addition, there are three phases for the CP violation. δ is the Dirac CP violation phase, and α_{21} and α_{31} are the Majorana CP violation

phases. If the neutrino is a Dirac particle (i.e. $\nu_i \neq \bar{\nu}_i$), only the Dirac phase is present. On the other hand, if the neutrino is a Majorana particle (i.e. $\nu_i \equiv \bar{\nu}_i$), also the Majorana phases are present.

The PMNS matrix can be written as shown in Equation 2.2, where $c_{ij} = cos(\theta_{ij})$, $s_{ij} = sin(\theta_{ij})$ with the mixing angles θ_{ij}.

$$
\begin{aligned}
U_{\alpha i} &= \begin{bmatrix} U_{e1} & U_{e2} & U_{e3} \\ U_{\mu 1} & U_{\mu 2} & U_{\mu 3} \\ U_{\tau 1} & U_{\tau 2} & U_{\tau 3} \end{bmatrix} \\
&= \begin{bmatrix} 1 & 0 & 0 \\ 0 & c_{23} & s_{23} \\ 0 & -s_{23} & c_{23} \end{bmatrix} \begin{bmatrix} c_{13} & 0 & s_{13}e^{-i\delta} \\ 0 & 1 & 0 \\ -s_{13}e^{i\delta} & 0 & c_{13} \end{bmatrix} \begin{bmatrix} c_{12} & s_{12} & 0 \\ -s_{12} & c_{12} & 0 \\ 0 & 0 & 1 \end{bmatrix} \begin{bmatrix} 1 & 0 & 0 \\ 0 & e^{i\alpha_{21}/2} & 0 \\ 0 & 0 & e^{i\alpha_{31}/2} \end{bmatrix}
\end{aligned}
\tag{2.2}
$$

The effective mass of the neutrino could basically be derived from the kinematics of double beta decays. It calculates to

$$
\langle m_{\nu_\alpha} \rangle = \sum_i |U_{\alpha i}|^2 |\nu_i\rangle
$$

but up to now, only upper limits could be given. From neutrino oscillation measurements, one gets the mass difference $\Delta m_{ij}^2 \equiv (m_i^2 - m_j^2), i \neq j$, nevertheless, the sign of the mass difference is not known. In Tab. 1, the present status is summarized.

	best value
$sin^2\theta_{12}$	0.304
$sin^2\theta_{13}$	< 0.035 *
$sin^2\theta_{23}$	0.5
Δm_{21}^2	$7.65 \cdot 10^{-5}\,eV^2$
Δm_{31}^2	$2.40 \cdot 10^{-3}\,eV^2$

Table 1: The current best data for the three mixing angles and the two mass differences [Nak10].*: this year, the three experiments T2K, MINOS and DobleChooz presented best fit values, indicating a $\theta_{13} > 0$.

As one can see, two mass differences (Δm_{21}^2 and Δm_{31}^2) are measured, while Δm_{32}^2 is not yet measured. Depending on the missing mass difference, three scenarios are possible:

- the **normal hierarchy**, $m_1 \ll m_2 < m_3$;

- the **inverted hierarchy**, $m_3 \ll m_1 < m_2$;

- the **quasi-degenerate** scenario, where $m_1 \cong m_2 \cong m_3$.

In figure 2, the normal and the inverted hierarchy are schematically drawn.
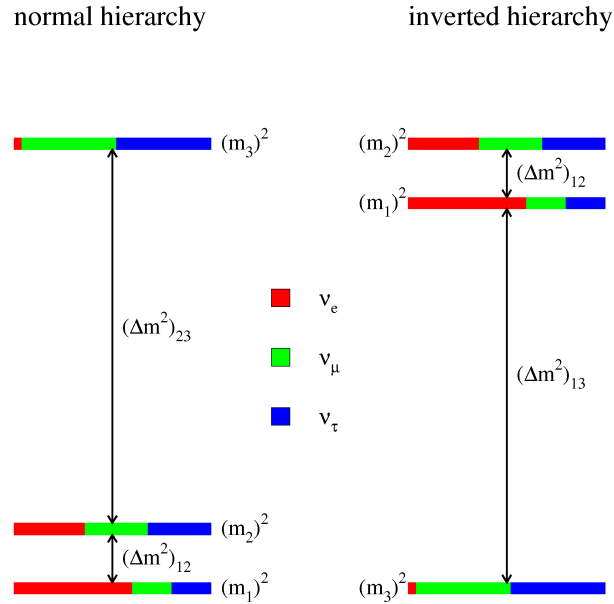
Figure 2: left: the normal hierarchy, with m_1 as the lightest neutrino mass eigenstate; right: the inverted mass hierarchy with m_3 as the lightest neutrino mass eigenstate. Fig. from [GJK05].

2.3   Neutrinoless double beta decay

2.3.1   "Standard" double beta decay

With help of the semi-empirical mass formula (also known as "Bethe-Weizsäcker formula", Equation 2.3, [Wei35, Bet36]), one can derive the binding energy of each nucleus.

$$M(A, Z) = N M_n + Z M_p + Z m_e - a_v A + a_s A^{2/3} + a_c \frac{Z^2}{A^{1/3}} + a_a \frac{(N - Z)^2}{4A} + \frac{\delta}{A^{1/2}} \qquad (2.3)$$

The formula consists of several different summands (after [Pov09]):

- $N M_n, Z M_p, Z m_e$: Sum of all constituents (neutrons, protons, electrons).

- $a_v A$, **volume term**: assuming a constant density, this term is proportional to the mass number A. It describes the force between the neighboring nucleons.

- $a_s A^{2/3}$, **surface term**: this term is a correction to the volume term, since the nuclei on the surface have less neighbors than those in the bulk. As the surface is proportional to volume$^{2/3}$, this term is proportional to A$^{2/3}$.

- $a_c \frac{Z^2}{A^{1/3}}$, **Coulomb term**: as there is an electrostatic repulsion between the protons, this repulsion destabilizes the nucleus. This is proportional to $Z^2 \cdot A^{-1/3}$.

- $a_a \frac{(N-Z)^2}{4A}$, **Asymmetric term**: for small mass numbers, nuclei with the same amount of protons and neutrons are preferred (^{12}C for example consists of six protons and six neutrons). To compensate the coulomb repulsion, nuclei with higher A are more and more asymmetric in the sense to house more neutrons than protons (e.g. $^{208}_{82}$Pb).

- $\frac{\delta}{A^{1/2}}$, **Pairing term**: this term accounts for spin-coupling of two protons or neutrons. If there is an even number of protons, the nucleus is most stable, if both numbers of protons with spin up and with spin down are equal, same for the neutrons. If there is a remaining proton (or neutron), the nucleus is less bound.

$$\delta = \begin{cases} -11.2\,MeV/c^2 & \text{for even-even nuclei} \\ 0\,MeV/c^2 & \text{for odd-even or even-odd nuclei} \\ +11.2\,MeV/c^2 & \text{for odd-odd nuclei} \end{cases}$$

For nuclei with the same total number of nucleons, but different composition ("isobars"), the mass number A is constant, and the summed mass of the constituents is almost constant, thus the main difference in the binding energy derives from the three last summands. As one sees, the Coulomb- and the asymmetric term lead to a parabolic curvature, if one plots the binding energy versus the number of protons (Z). In addition, for nuclei with an odd number of nucleons, there is only one parabola, as $\delta = 0$. The single parabola leads to one most stable isobar. The isobars with less protons than the most stable isobar (i.e. the left part of the parabola) undergo β^- decay, while those on the right side (those with more protons) undergo electron capture (EC) or β^+ decay. For nuclei with an even number of nucleons (such as A=76), two parabolas exist, one for odd-odd nuclei (odd number of protons, odd number of neutrons) and another parabola for even-even nuclei. In this case, it might occur, that there are two stable isobars. Figure 3 shows a schematic drawing of the isobar chain for A=76.

As one can see, ^{76}Ge is more stable than its right neighbor ^{76}As, so, the β^- decay ($^{76}_{32}Ge \rightarrow {}^{76}_{33}As + e^- + \bar{\nu}_e$) is energetically forbidden. Nevertheless, a double beta decay with emission of two electron-antineutrinos ($2\nu\beta\beta$) to ^{76}Se ($^{76}_{32}Ge \rightarrow {}^{76}_{34}Se + 2e^- + 2\bar{\nu}_e$) is still possible. This is a second order process, so the half life time is much higher than for a "standard single beta decay". In fact, the $2\nu\beta\beta$ of ^{76}Ge was observed, its halflife is $T^{2\nu\beta\beta}_{1/2} = (1.78\pm0.01)\cdot10^{21}$ y [Bak05], which is one of the longest half life time of a radioactive decay ever measured. As the two neutrinos can escape the detector without depositing energy, the spectrum is continuous (analogue to the single beta decay). One can describe the double beta decay as:

$$^A_Z X \rightarrow {}^A_{Z+2} Y + 2e^- + 2\bar{\nu}_e$$
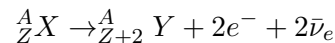
Up to now, $2\nu\beta\beta$ was detected for eleven nuclei: ^{48}Ca, ^{76}Ge, ^{82}Se, ^{96}Zr, ^{100}Mo, ^{116}Cd, ^{128}Te, ^{130}Te, ^{136}Xe, ^{150}Nd and ^{238}U, in addition, the $2\nu\beta\beta$ decay of ^{100}Mo and ^{150}Nd to the 0^+ excited state of their daughter nuclei (^{100}Ru and ^{150}Sm) and a ECEC(2ν) process in ^{130}Ba were detected [Bar11b, Ack11].

2.3.2   Neutrinoless double beta decay

In the year 1937, Ettore Majorana proposed that there is only one neutrino, so $\nu_e \equiv \bar{\nu}_e$ [Maj37]. In this case, the theory of a single beta decay remains unchanged, while offering a new possibility for the double beta decay. If the neutrino is the same particle as the anti-neutrino, a neutrinoless

Figure 3: A schematic drawing of the ground levels for isobars wit A = 76. Dark blue are the β^- decays, β^+ decays are shown in cyan. The decay $^{76}_{32}Ge \rightarrow^{76}_{33} As$ is energetically forbidden, while the double beta decay $^{76}_{32}Ge \rightarrow^{76}_{34} Se$ (in red) is energetically allowed. Schematic drawing after [Sin95].

double beta decay ($0\nu\beta\beta$) could be possible as well. In this decay, only two electrons would be emitted, meaning that the spectrum of $0\nu\beta\beta$ would be a discrete line at a defined energy ($Q_{\beta\beta} = 2039$ keV for ^{76}Ge, see Tab. 2). There are several isotopes, whose Q-value is well above the maximal γ energy from natural radioactivity (2.615 MeV for ^{208}Tl). These isotopes offer a good chance to detect $0\nu\beta\beta$ with low background contribution. Figure 4 shows the Feynman graphs of $2\nu\beta\beta$ and $0\nu\beta\beta$. The expected spectra of the two double beta decays are shown in fig. 5. If $0\nu\beta\beta$ exists, it leads to the conclusion, that the lepton number is not conserved, as $\Delta L_{0\nu\beta\beta} = 2$. This opens a new window to physics beyond the standard model.

Once the half life time of $0\nu\beta\beta$ ($T^{0\nu}_{1/2}$) is measured, one can derive the effective neutrino mass ($\langle m_\nu \rangle$) with this formula [DKT85]:

$$\frac{1}{T^{0\nu}_{1/2}} = G^{0\nu}(E_0, Z) \left| M^{0\nu}_{GT} - \frac{g^2_V}{g^2_A} M^{0\nu}_F \right|^2 \langle m_\nu \rangle^2 \tag{2.4}$$

where $G^{0\nu}(E_0, Z)$ is the phase-space integral, $M^{0\nu}_{GT}$ and $M^{0\nu}_F$ are the nuclear matrix elements, and $\langle m_\nu \rangle$ is the effective neutrino mass. In theoretical particle physics, the calculation of the nuclear matrix elements (NME) is a vital field. In fig. 6, the NME for different elements and different approaches are plotted. As one can see, in some cases, there is a relatively good agreement of the

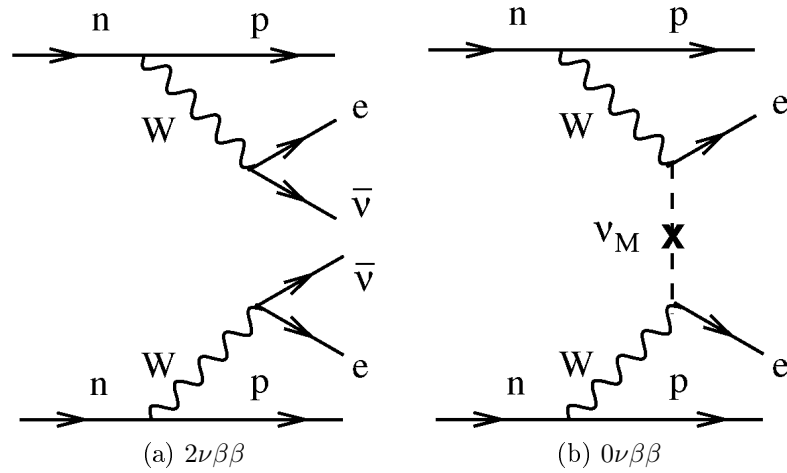(a) $2\nu\beta\beta$ (b) $0\nu\beta\beta$

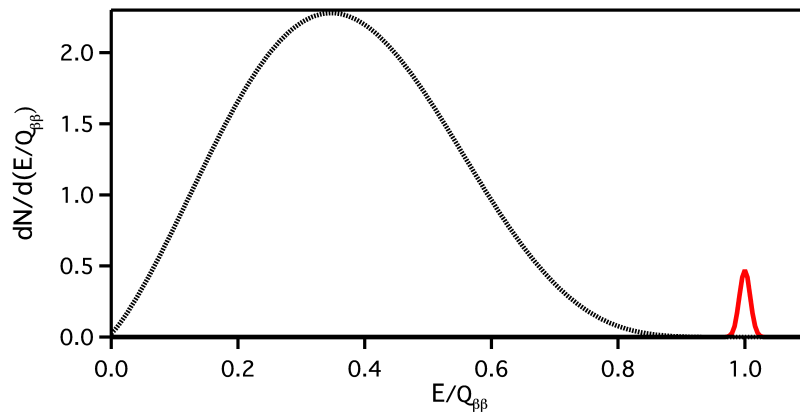Figure 4: The Feynman graphs for $2\nu\beta\beta$ and $0\nu\beta\beta$, taken from [AEE08]

Figure 5: The theoretical spectra of the two different double beta decays. Dotted black line: $2\nu\beta\beta$, solid red line: $0\nu\beta\beta$. It was assumed, that the energy resolution for 1σ is $2\,\%$ and that the relative intensity of $0\nu\beta\beta$ is $1\,\%$ of the $2\nu\beta\beta$. The plot is taken from [AEE08].

different approaches, while in other cases, they differ by a factor of 2.

2.3.3 $0\nu\beta\beta$ experiments

In the last decades, several experiments were performed, aiming for the detection of $0\nu\beta\beta$. Up to now, only lower limits could be achieved. Nevertheless, part of the Heidelberg-Moscow experiment claims to have observed $0\nu\beta\beta$ in ^{76}Ge, but this claim is widely discussed and criticized. During the years, $T^{0\nu}_{1/2}$ slightly changed from $1.5 \cdot 10^{25}$ y [KK01a] to $2.23^{+0.44}_{-0.31} \cdot 10^{25}$ y [KKK06]. Here, just a very brief overview of some experiments is given, since a nice overview about the history, present and future of double beta decay searches can be found in [Bar11a, Bar11b]. The GERDA

Table 2: The $Q_{\beta\beta}$ values for the double beta decay candidates [NNDC08].

nucleus	$Q_{\beta\beta}$ in keV	nat. Abundance in %
^{48}Ca	4274	0.19
^{76}Ge	2039	7.83
^{82}Se	2996	8.73
^{96}Zr	3348	2.80
^{100}Mo	3035	9.63
^{110}Pd	2004	11.72
^{116}Cd	2809	7.49
^{124}Sn	2288	5.79
^{128}Te	868	31.74
^{130}Te	2530	34.08
^{136}Xe	2462	8.86
^{150}Nd	3368	5.60
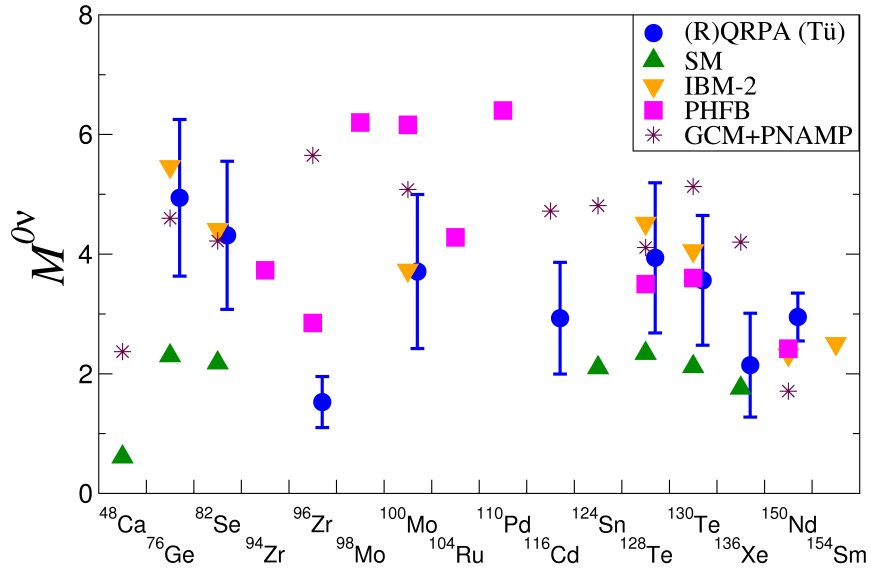
Figure 6: The calculated nuclear matrix elements for different isotopes. Five different calculations are shown. (R)QRPA: (Renormalized) Quasi-particle Random Phase Approximation; SM: Shell Model; IBM-2:Interacting Boson Model; PHFB: Projected Hartree-Fock-Bogoliubov and GCM+PNAMP: PHFB with the Generator Coordinate Method (GCM) with deformations. The plot is taken from [Fae11].

experiment will be described in Chapter 3.

- **Heidelberg-Moscow and IGEX**: Both experiments used germanium detectors enriched in ^{76}Ge. Heidelberg-Moscow (HdM, active 1995-2003) was located in the LNGS[2], while IGEX (**I**nternational **G**ermanium **EX**periment, run from 1994-2000) was located in the LSC[3] in Spain. The setup of both experiments was quite similar, the detectors themselves were put into an onion-like structure of different shieldings (innermost ultrapure copper and lead, then polyethylene, and in the case of IGEX plastic scintillators as active muon veto). To get rid of ^{222}Rn and its daughter nuclei, the setups could be flushed by nitrogen, replacing the Rn-contaminated air. IGEX gave a lower limit of $T^{0\nu}_{1/2} > 1.57 \cdot 10^{25}$ y [Aal02], the lower limit given by HdM was $T^{0\nu}_{1/2} > 1.9 \cdot 10^{25}$ y.

- **Majorana experiment**: This experiment will be located at the DUSEL[4]. Basically, its setup is the same (standard) setup as in HdM or IGEX. It is aiming for a 500 kg experiment, where half of the germanium mass will be natural germanium for background studies, so 250 kg of enriched detectors have to be produced. The detectors will be placed in four modules. These modules are mounted in a copper cryostat and then shielded by a huge amount of copper, lead and polyethylene. The very first module, the "Demonstrator", is planned to be operational in 2013. The long term aim is, to join GERDA and Majorana to a world wide 1 t scale $0\nu\beta\beta$ experiment. GERDA and Majorana are already jointly using the MAGE framework, a simulation tool developed for both experiments [Gui11].

- **NEMO**: the **N**eutrino **E**ttore **M**ajorana **O**bservatory was located in the Frejus underground laboratory[5]. Data taking of NEMO-3 was from 2003 to January 2011, searching for $0\nu\beta\beta$ in ^{82}Se and ^{100}Mo. SuperNemo is planned to be fully functional in 2014, searching with ^{82}Se. The SuperNEMO detector has a modular concept, consisting of around 20 planar units with typically 5 kg of isotope per $5 \times 4 \times 1$ m^3 module. The double beta decay isotopes are located on thin foils. The electrons are emitted from the foil and then traverse a tracking chamber with around 3000 wire drift cells. At the end, there is a calorimeter measuring the energy of the electrons [Shi08].

- **CUORE / CUORICINO**: CUORE (**C**ryogenic **U**nderground **O**bservatory for **R**are **E**vents; ital. for "heart") and its pilot experiment CUORICINO (ital. "small heart") are searching for $0\nu\beta\beta$ in ^{130}Te. Both experiments are located at the LNGS. The test-experiment CUORICINO was measuring from 2003 to 2008, and at the moment, CUORE is being built. At the end of the construction phase (2013), it will house 988×750 g TeO$_2$ bolometers in 19 towers of 52 crystals each. The setup of CUORICINO consists of one of these towers. On one surface of the cubic TeO$_2$ crystals, NTD[6]-Germanium thermometers are located. The whole setup is cooled down to a temperature of 7 - 10 mK. Here, an energy deposition in the crystal is recorded as a thermal rise. Besides $0\nu\beta\beta$, CUORE is also searching for cold dark matter, solar axions and rare nuclear decays [Arn08].

---

[2]**L**aboratori **N**azionali del **G**ran **S**asso, http://www.lngs.infn.it
[3]**L**aboratorio **S**ubterráneo de **C**anfranc, http://www.lsc-canfranc.es/
[4]**D**eep **U**nderground **S**cience and **E**ngineering **L**aboratory in the former Homestake Mine, http://www.dusel.org/
[5]**L**aboratoire **S**outerrain de **M**odane, http://www-lsm.in2p3.fr/
[6]NTD = Neutron Transmutation Doped

- **EXO**: the **E**nriched **X**enon **O**bservatory. As the name is suggesting, this experiment searches for the $0\nu\beta\beta$ in ^{136}Xe. It is currently being built up at the WIPP[7]. The detector is a time projection chamber, where liquid Xenon is detector and source. It houses 175 kg liquid Xenon, enriched to $80.6 \pm 0.1\,\%$ in ^{136}Xe. Most recently, EXO-200 published $T_{1/2}^{2\nu\beta\beta} = 2.11 \pm 0.04(stat) \pm 0.21(sys) \cdot 10^{21}$ y [Ack11].

- **SNO+**: The SNO+ will be located in the Sudbury mine[8], where also SNO was located. SNO+ will re-use the acrylic sphere, PMTs and PMT-support structure from SNO. The innermost volume, the acrylic sphere with 12 m diameter, will be filled with 800 t liquid scintillator. It is placed inside a large cylindrical volume filled with water. Besides searching for $0\nu\beta\beta$, SNO+ also wants to study low energy solar neutrinos, reactor neutrinos, geo neutrinos, and supernova neutrinos. To detect $0\nu\beta\beta$, 56 kg of ^{150}Nd will be mixed into the liquid scintillator, so the scintillator will be doped with $0.1\,\%$ natural Nd. In a second stage, it is foreseen to enlarge the amount of Nd up to 500 kg. The filling of the water volume is planned for April 2012 [Che08].

- **COBRA**:The **C**admium Zinc Telluride **0**-Neutrino Double-**B**eta **R**esearch **A**pparatus uses CdZnTe room-temperature semiconductor detectors. For $0\nu\beta\beta$, nine candidate isotopes are contained in CdZnTe, where ^{116}Cd and ^{130}Te isotopes are the most promising. As the detectors are operated at room temperature, no complicated cooling system has to be used. So, in principle, it is quite simple to expand the detector/source mass. Thus, the final stage of COBRA will hold up to 64000 of such detectors (each $1 \times 1 \times 1\,\text{cm}^3$, 10 g), giving a total detector mass of 640 kg. Up to 2010, a prototype test with 64 detectors has been performed at LNGS, where COBRA is located. Also different detector types, such as CPG (coplanar grid) and TimePix (128 $\times$128 pixel) have been tested at LNGS. A scientific proposal is foreseen for 2012 [COB10].

2.4 Muons

2.4.1 Origin of muons

As already described, muons are a part of the class of leptons, together with electrons, tauons and the three neutrinos. They have a rest mass of $m_\mu = 105.658367\,\text{MeV}$ and a mean life time of $\tau = 2.197034\,\mu$s [Nak10]. Muons, which can be measured on the surface of the earth are secondary particles produced by so called **cosmic radiation**.

2.4.1.1 Cosmic radiation

In 1912, Victor Hess measured the ionization rate at different altitudes in the atmosphere. At that time, radioactive elements in the earth and their gaseous daughter nuclides were assumed to be the origin of atmospheric electricity. Therefore, he expected to measure a decreasing ionization while reaching higher altitudes. He measured however that the ionization increases with the altitude.

---

[7]**W**aste **I**solation **P**ilot **P**lant, http://www.wipp.energy.gov/
[8]also known as SNOLAB, http://www.snolab.ca/

His conclusion was, that there has to be high energy radiation, which is entering the atmosphere from the outside, i. e. cosmos.

The primary *cosmic rays* mostly consist of protons or hydrogen nuclei ($\approx 89\,\%$), $10\,\%$ helium nuclei (alpha particles) and $1\,\%$ heavier elements. These highly energetic particles (up to $10^{20}\,\mathrm{eV}$) interact with molecules in the upper atmosphere, mostly oxygen and nitrogen. These collisions lead to a production of secondary particles such as $\gamma, \mu^{\pm}, \pi^{0,\pm}$, as shown in figure 7. The pions ($m_{\pi^{\pm}} = 139.57018\,\mathrm{MeV}$, $m_{\pi^0} = 134.9766\,\mathrm{MeV}$) have a mean life time of $\tau_{\pi^{\pm}} = 26.033\,\mathrm{ns}$ and $\tau_{\pi^0} = 8.4 \cdot 10^{-17}\,\mathrm{s}$. The primary decay for the charged pions is:

$$\pi^+ \rightarrow \mu^+ + \nu_{\mu}, \pi^- \rightarrow \mu^- + \bar{\nu}_{\mu}$$

with a fraction of 0.9998770, while the most prominent decay of the neutral pion is an electromagnetic decay into two gamma rays [Nak10]. On their way to the sea level, secondary particles can again decay or produce other particles, at the end, an extensive air shower reaches the earth's surface. In general, one can divide the secondary particles into three groups:

- "soft" component, electromagnetic shower, consisting mainly of γ's from the decay of π^0 and annihilation of e^+ and e^-.

- "hard" or "muonic" component, consisting of muons.

- "hadronic" component, mainly p and n.

All three components of the air shower can be measured on the earth's surface. $80\,\%$ of the charged component consists of muons. The soft and the hadronic component can be shielded with a few meters of soil or rock, while muons can penetrate the rock quite easily and thus can be detected even in deep underground laboratories.

2.4.2   Cherenkov effect

A charged particle such as a muon, traversing a dielectric medium at a speed greater than the phase velocity of light in the respective medium is causing electromagnetic radiation. Pavel A. Cherenkov discovered this phenomenon in the year 1934 when he observed a bottle of water emitting a bluish light, when it was penetrated by the radiation of a radium source. In 1958, Cherenkov was awarded with the Nobel price in physics, together with Il'ja M. Frank and Igor Y. Tamm *"for the discovery and the interpretation of the Cherenkov effect"*. The refractive index n of water is 4/3, thus, the phase velocity of light in water is 3/4 of c. While a charged particle is traversing the medium at a speed greater than the phase velocity of light in this medium, the molecules of the medium get polarized by the throughgoing particle. By emitting electromagnetic radiation, the molecules relax to their ground state. The electromagnetic radiation emitted on different points of the particle track interfere. And, analogous to the sonic boom of an aircraft traveling with supersonic velocity, if the velocity of the particle is more than c/n, the radiation interferes constructively in a cone with a specific angle θ_c, depending on the velocity v of the particle (fig. 8) [Gru05]. The specific angle is calculated to $\theta_c = arccos\ \frac{c_0}{nv}$.

The Cherenkov angle for a relativistic particle ($v/c_0 \approx 1$) in water therefore is $42°$. The muons reaching the GERDA water tank have a mean energy of 270 Gev [Ahl93], in other words a mean velocity of only 10^{-7} less than c, thus they are highly relativistic.
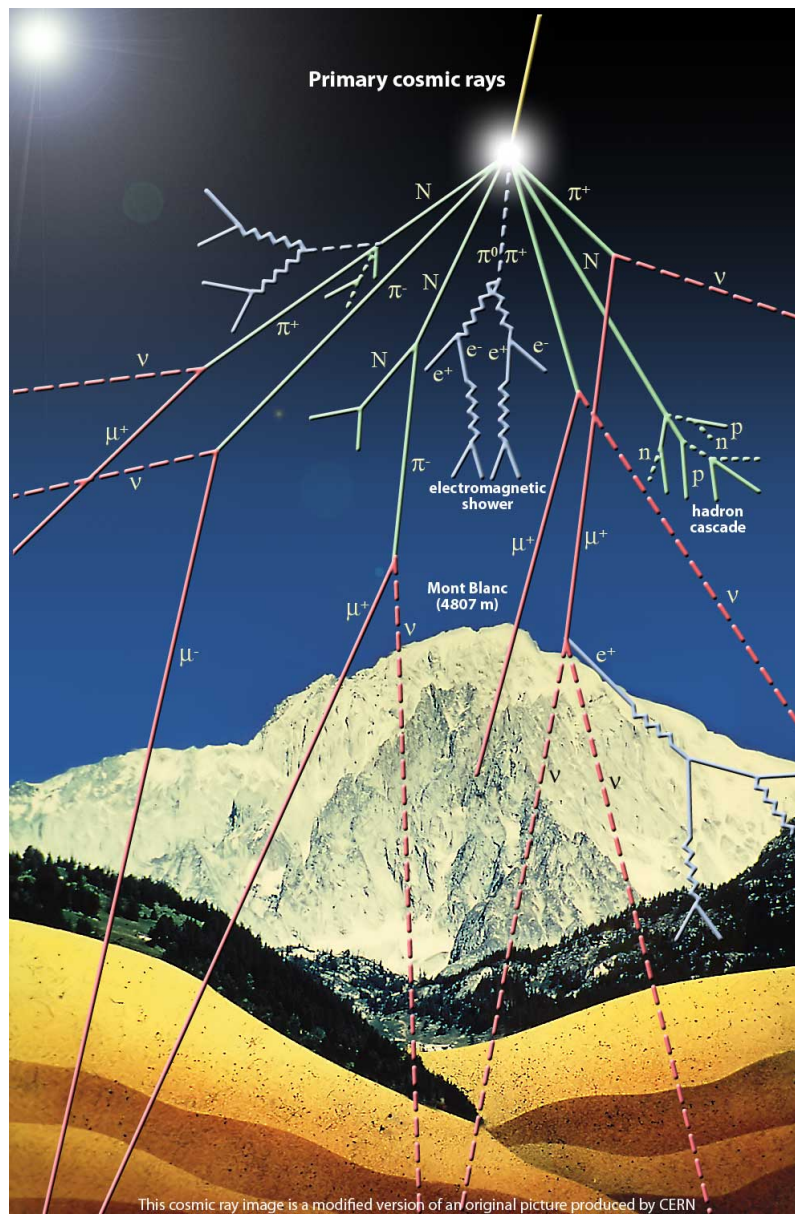
Figure 7: Air shower. In this sketch, only some secondary particles are shown, depending on the energy of the primary particle, several millions or billions of secondary particles can be produced. Fig. from [Cos].
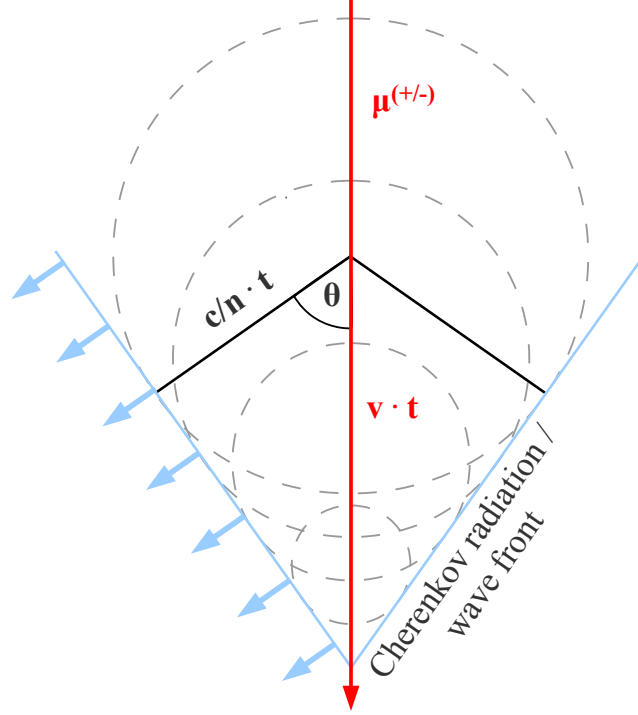
Figure 8: Schematic drawing of the Cherenkov effect.

To get a number of optical photons, N, which are produced by a muon in a water tank, one can take equation 2.5 [Gru05]:

$$\frac{dN}{dx} = 2\pi\alpha z^2 \ \frac{\lambda_2 - \lambda_1}{\lambda_1\lambda_2} \ sin^2\theta_c \tag{2.5}$$

here, α is the fine-structure constant ($\approx 1/137$), z is the charge of the incident particle (for muons ±1), λ_1 (λ_2) is the minimal (maximal) wavelength (as the PMT used have their highest quantum efficiency between 300 and $500\,nm$, these values are used), and θ_c is the Cherenkov angle. This leads to ≈ 270 photons/cm for a relativistic particle with a charge of one, such as a muon.

For an electron emitted for example by the photoeffect due to an ambient γ, i.e. with a maximal energy of $2.6\,MeV$, the velocity is $0.9805\,c_0$. For this electron, the Cherenkov angle is $\theta_c = 40.1°$, and the corresponding amount of light is 260 photons per cm. This number is quite similar to the number derived for muons, but as the energy of the electron is only $2.6\,MeV$ (compared to $270\,GeV$ for the muon), one has to take energy loss by ionization into account. The **Bethe-Bloch formula** (Equation 2.6) describes the energy loss [Nak10]:

$$- \frac{dE}{dx} = Kz^2 \frac{Z}{A} \frac{1}{\beta^2} \{\frac{1}{2}ln\frac{2m_ec^2\beta^2\gamma^2 T_{max}}{I^2} - \beta^2 - \frac{\delta}{2}\} \tag{2.6}$$

where

K	–	$4\pi N_A r_e^2 m_e c^2 \approx 0.307 MeV/(g/cm^2)$,
N_A	–	Avogadro's number $= 6.02214179 \times 10^{23} mol^{-1}$,

r_e –   classical electron radius ($\approx 2.82\,\mathrm{fm}$),

$m_e c^2$ –   electron rest energy ($511\,\mathrm{keV}$),

z   –   charge of the incident particle,

Z,A   –   target charge number and target mass number,

β –   velocity of the incident particle ($= \mathrm{v}/c$),

γ – $\frac{1}{\sqrt{1-\beta^2}}$,

T_{max} – $\frac{2 m_e p^2}{m_0^2 + m_e^2 + 2 m_e E/c^2}$,

                       maximum energy transfer to an electron,

                       m_0 mass of the incident particle,

                       p, E - momentum and total energy of the projectile

I   –   average ionization energy of the target,

δ –   density correction.

In fig. 9, the energy loss of muons is illustrated for different materials. For low energies, there is a $1/\beta^2$ increase. At $\beta\gamma \approx 3.5$, minimum ionization occurs. Particles with such $\beta\gamma$ values are called "minimal ionizing". For high energies, the energy loss increases logarithmically. The energy loss of a singly charged minimal-ionizing particle in water is $\sim 2\,\mathrm{MeV}/(\mathrm{g/cm}^2)$. Consequently, an electron with an energy of $2.6\,\mathrm{MeV}$ does not travel more than $1.5\,\mathrm{cm}$ in water until having lost its kinetic energy. Such a $2.6\,\mathrm{MeV}$ electron would cause around 400 photons to be emitted in the Cherenkov veto. These numbers will be used in Chapter 8.7.2 to estimate if such electrons are an important background source for the GERDA muon veto.
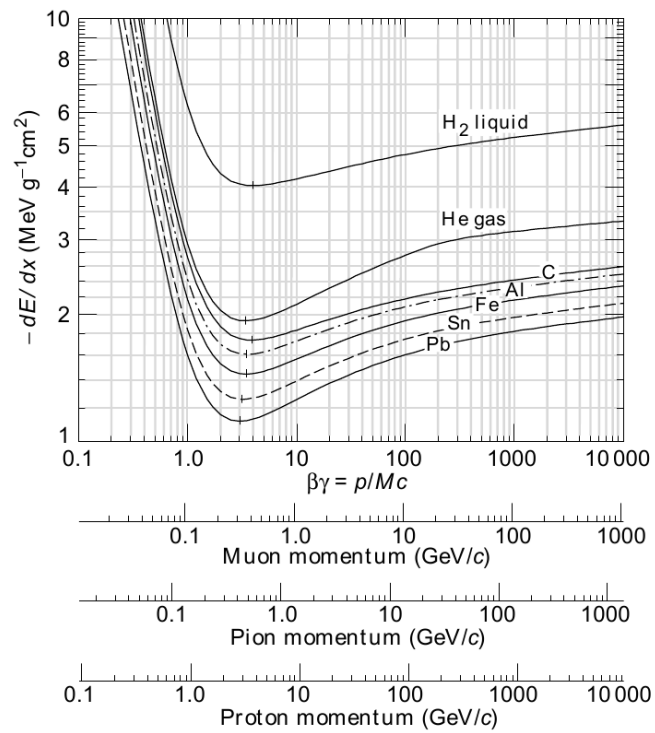
Figure 9: Mean energy loss in liquid (bubble chamber) hydrogen, gaseous helium, carbon, aluminum, iron, tin, and lead. Radiative effects are not included. Fig. from [Nak10].

Chapter 3

GERDA

Before going into detail, this chapter will explain the GERDA experiment. The setup of the muon veto of GERDA will be described in Chapter 4 separately.

3.1 The LNGS

GERDA, the **GER**manium **D**etector **A**rray, is located in the Laboratori Nationali del Gran Sasso (LNGS, fig. 10) in the mountains of Abruzzo in Italy. This laboratory is the world largest underground laboratory, run by the Italian INFN (Istituto Nazionale di Fisica Nucleare - the Italian national institute for nuclear physics). On the highway from the Adria to Rome, a 10 km tunnel is passing through the Gran Sasso mountains (fig. 10), and about in the middle of the tunnel, the entrance to the LNGS is located. The highway access and generously planned tunnel sizes offer the possibility to bring in quite large parts of the experimental setup in one piece, since it is possible to drive in with a standard 40 t-truck. Built up in the early 1980's, the LNGS houses 15 experiments in the fields of particle physics, particle astrophysics and nuclear astrophysics. Due to a coverage of at least 1400 m (around 3100 M.w.e.) of dolomite rock in all directions, the LNGS is well shielded from cosmic rays. The small Uranium and Thorium contamination in the rock reduces the neutron flux in the experimental halls.

3.2 Requirements and benefits for GERDA

GERDA is searching for the neutrinoless double beta decay ($0\nu\beta\beta$) in ^{76}Ge. As it was mentioned in Chapter 2, $0\nu\beta\beta$ is a very rare decay. But the neutrinoless double beta decay in germanium is a good candidate to be discovered, of course, if it exists:

- Germanium detectors are source and detector at the same time. As the β particles released in the $0\nu\beta\beta$ have a short mean free path in germanium, the detection efficiency of such an event is nearly 100 %.

- HPGe detectors can be fabricated very pure. During purification, it is possible to remove most of the intrinsic radioactive impurities such as ^{60}Co.
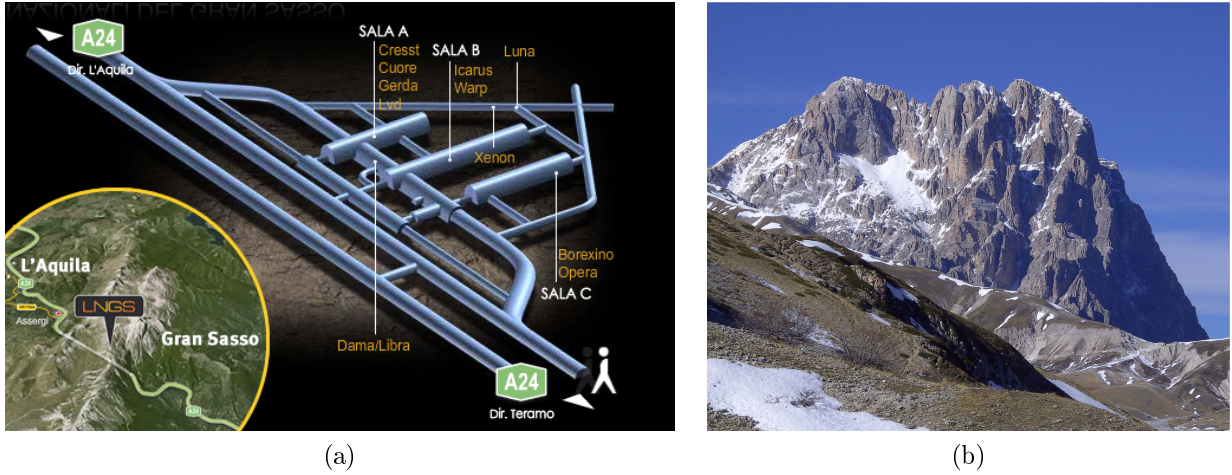
19

Figure 10: (a) Schematic of the LNGS laboratory, from [INF]; (b) the Gran Sasso mountains, the natural part of the shielding.

- The energy resolution of germanium diodes is very good, in fact, an energy resolution of $0.1\,\%$ in the region of $Q_{\beta\beta}$ ($2.039\,\mathrm{MeV}$) is reachable. A better energy resolution leads directly to a higher peak sensitivity.

- Germanium detectors can be made from material highly isotopically enriched in ^{76}Ge. An enrichment from a natural $8\,\%$ to $86\,\%$ is feasible and was already achieved in the past [KK01b].

Pulse shape analysis and anti-coincidence between the detectors give a big opportunity to reduce background contributions, since $0\nu\beta\beta$ is depositing the whole energy within a small volume, while for example a muon passing through a string of detectors will most probably deposit energy in several detectors.
But despite these opportunities, a very good reduction and understanding of the remaining background is necessary. Background contributions are for example environmental radioactive elements such as the decay chains of ^{232}Th, ^{238}U and ^{235}U as well as muons created in the upper atmosphere due to cosmic rays.

3.3   GERDA-setup

To reduce the background, GERDA is located in the LNGS, where it is surrounded by at least $1400\,\mathrm{m}$ of rock in all directions. This first and most massive part of the shielding is reducing the flux of muons dramatically. While on the surface, typically 100-200 $\mathrm{muons}/(\mathrm{m}^2 \cdot \mathrm{s})$ can easily be measured, the dolomite rock of the Gran Sasso mountains reduces this flux to 1.1 $\mathrm{muons}/(\mathrm{m}^2 \cdot \mathrm{h})$, which is a flux reduction of more than five orders of magnitude. Nevertheless, this muon rate is still too high for GERDA, so an active shielding is needed. As the description of the GERDA muon veto is following in Chapter 4, it is just briefly discussed here as a combination of a Cherenkov veto

and a scintillation veto. The innovative design of GERDA is to run the germanium detectors naked in liquid argon. "Standard" setups normally are designed in an onion-like shielding structure. In that case, the detector itself is placed in a vacuum box, connected to a cold finger (normally a copper bar), whose other end is submerged into a cooling liquid like nitrogen. The vacuum box is surrounded by ultra pure copper and lead to prevent γ radiation to reach the detector. Sometimes, also a polyethylene shielding is applied to protect the experiment from neutrons. This setup is quite compact, nevertheless, a muon passing through the lead and/or copper could lead to a particle shower in the shielding, which then could reach the detector and produce a background signal. To prevent this, high-Z materials should be avoided close to the detector, as those materials are better targets for showers and activation. This leads to the innovative setup of GERDA. In GERDA, the detectors are operated naked in the cooling liquid, argon. Only the holders for the detectors are made of as little electroformed copper as possible. Only 31 g of copper are needed to hold a 2.1 kg germanium diode in place. Thus, a passing muon should not produce as much secondaries as in the standard setup.

In fig. 11, an artist view of GERDA is shown. The volume of the cryostat (4 m in diameter, 6 m height) is filled with 64 m^3 of 6.0 grade liquid Argon[1]. Submerged into the liquid Argon, the germanium detectors are located in the center of the cryostat. The argon serves both as coolant for the detectors, and as shielding against gamma rays. As an additional shielding against γ's coming from the stainless steel of the cryostat, sheets of ultra pure copper are mounted on the inner wall of the cryostat, since copper can be produced much more clean than stainless steel.
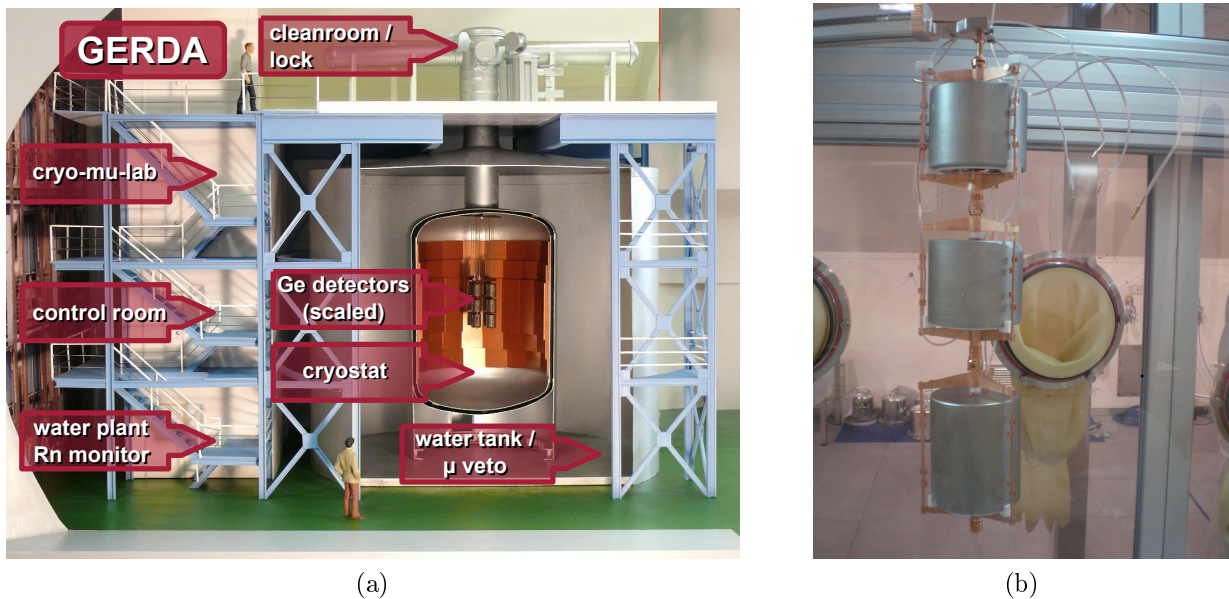

(a)   (b)

Figure 11: (a) Artist view of the GERDA setup (original picture from [GER]); (b) picture of a 3-detector string ready to be submerged into LAr, from [Mac11].

---

[1]The grade gives the purity in terms of other elements of the liquid gas, in this case, the purity is 0.999999

Figure 12: Picture of GERDA, taken in November 2010.

The detector holders are made of electroformed ultra pure copper, silicone and PTFE. A stainless steel chain is fed through the neck of the cryostat and serves as a cable tray and as a mount for the detector holders. This system offers the possibility to lower down the detector string. At the moment the Commissioning Lock is installed. With this, one can handle a three-string arm at the same time as a one-string arm. A final lock is being planned at the moment for the next phase of GERDA. This final lock will be able to hold up to 19 single strings. The lock itself is located in a class 10,000 clean room (i.e. $< 10,000$ particles of a size $< 0.5\,\mu$m in a volume of $1\,\text{ft}^3$, or, 353,147 particles in $1\,\text{m}^3$, this is comparable to the ISO 7-class). Three detectors are mounted on one string and connected to the high voltage and the data cables in the clean room. Afterwards, the string is slowly lowered down through the neck of the cryostat and submerged into the liquid Argon. As the detectors have to be cooled down from room temperature (around $300\,\text{K}$) to $87,3\,\text{K}$, this has to be done slowly, otherwise, the contacts at the diodes or the diodes themselves could be damaged. There are three radioactive sources available in the lock (^{228}Th with an activity of $\approx 20\,\text{kBq}$ each) used for calibration of the detectors. Once a week, a calibration run is performed. For this, the source is lowered down from its parking position at the top of the cryostat's neck towards the detectors. At different heights, it is stopped to "bombard" the detectors with γ rays. The ^{228}Th source offers several γ lines, so with the data taken, one can calibrate the data taking run. Typically, such a calibration run takes around one hour. Afterwards the source is moved back to its parking position. To prevent radon emanation from the steel tank to reach the detectors, a $80\,\text{cm}$ diameter copper shroud was deployed to prevent convection towards the detectors.

A water tank with $10\,\text{m}$ diameter and $9\,\text{m}$ height, filled with $580\,\text{m}^3$ ultrapure water, is surrounding the cryostat. It acts as a neutron moderator, slowing down fast neutrons from the environment. In addition, it also acts as an active muon veto. As described in Chap. 2.4.2, the muons reaching the underground laboratory have an average energy of $270\,\text{GeV}$, so they are highly relativistic. Cherenkov light is produced, when they are passing through the water tank. This light can then be used to identify a throughgoing muon. Without a muon veto, a muon depositing energy in the germanium diodes is contributing to the background. As one can see in figure 11 and as mentioned in the section before, the detectors can be brought into the cryostat through the neck via the lock system. The neck is a blind spot for the Cherenkov muon veto, since it is a volume without water. Muons passing through the neck come close to the detectors, so it is quite easy to deposit energy in the detectors without triggering the Cherenkov veto. To detect these muons, a second part of the muon veto is installed right on top of the clean room (just at the top outside the artist view). 36 plastic scintillator panels are mounted in three layers to get not only the information, if there was a muon, but in addition, due to a rough pixilation, one also gets the information, where the muon went through.

3.4 Physics of GERDA

The physics goal of GERDA is shortly described with: "find an evidence for $0\nu\beta\beta$ or at least push the limits".

In the following, the physics goal of GERDA and some results from former experiments are described. Next, the detectors are described and how they are used. Also a brief comparison between the standard germanium detectors and the newly developed BEGe detectors is given. Finally the background issues are listed GERDA has to cope with.

3.4.1   Physics goal

The current lower limit for the halflife of $0\nu\beta\beta$ for ^{76}Ge is given by the Heidelberg-Moscow (HdM) experiment. This experiment was also built up at LNGS and ran from 1990 to 2003. The halflife time $T_{1/2}^{0\nu} > 1.9 \cdot 10^{25}$ y (90 % C.L.) is derived from data of an exposure of $35.5\,(\text{kg} \cdot \text{y})$. Depending on the matrix elements, an upper limit for the effective Majorana neutrino mass is given at $0.35\,\text{eV}$ [KK01b]. Using the data of HdM, a part of the collaboration published a claim of a detection of the $0\nu\beta\beta$ in ^{76}Ge with a halflife of $T_{1/2}^{0\nu} = 2.23_{-0.31}^{+0.44} \cdot 10^{25}$ y [KKK06]. As this is up to now the first (and only) claim of the detection of $0\nu\beta\beta$ it is controversially discussed. One of the aims of GERDA is either to verify or to reject this claim. To achieve this, the background has to be identified very well. For Phase I, the background should not exceed $10^{-2}\,\text{cts}/(\text{keV}\cdot\text{kg}\cdot\text{y})$, while for Phase II, the plan is to lower the background contribution to $10^{-3}\,\text{cts}/(\text{keV}\cdot\text{kg}\cdot\text{y})$. In comparison, HdM listed a background index of $1.9 \cdot 10^{-1}\text{cts}/(\text{keV}\cdot\text{kg}\cdot\text{y})$ [KK01b]. Figure 13 shows possible limits on the half life time as a function of the exposure. Different background conditions are plotted. The unit $\text{cts}/(\text{keV}\cdot\text{kg}\cdot\text{y})$ describes the amount of counts per exposure $(\text{kg} \cdot \text{y})$ and energy bin (in keV) in the region of interest. This means, if the detector mass is $100\,\text{kg}$, the experiment run time is one year, and the energy interval is $10\,\text{keV}$, one would expect to have 10 events originating from background in the region of interest (ROI), if one achieves a background limit of $10^{-2}\text{cts}/(\text{keV}\cdot\text{kg}\cdot\text{y})$.
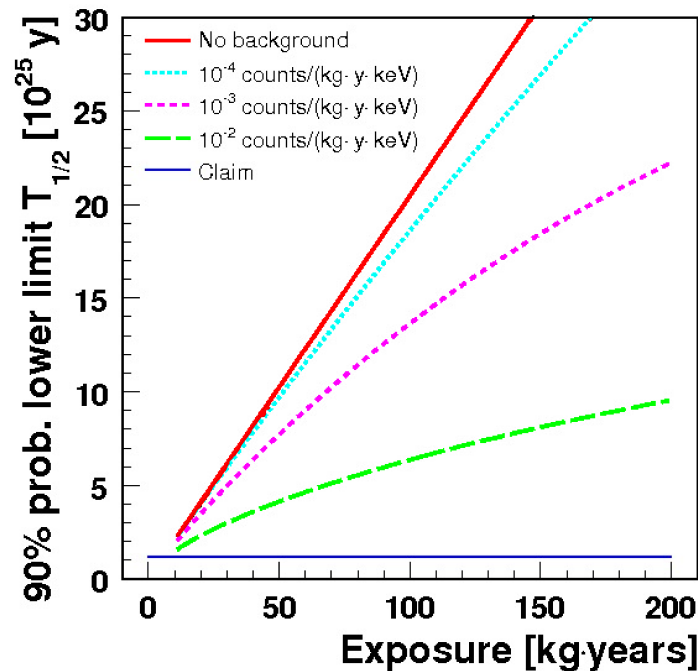

Figure 13: The expected 90 % probability lower limit on the half-life for neutrinoless double beta decay is plotted versus the exposure under different background conditions. The half-life for the claimed observation for neutrinoless double beta decay of ^{76}Ge [KK04] is also shown in blue, from [CK06].

3.4.2 The germanium detectors

3.4.2.1 Phase I detectors

In Phase I, existing germanium detectors enriched in ^{76}Ge will be used. These detectors were used in the former experiments IGEX [Aal02] and HdM [KK01b]. The detectors have been refurbished and also prepared for the usage in liquid Argon. All of these detectors are standard closed end coaxial germanium detectors (fig. 14), with roughly 2 kg detector mass each. The standard coaxial design is a cylindrical single crystal with a borehole in the middle. The borehole is one contact, while the outer surface is the other contact. A high voltage of around 3 kV is applied to totally deplete the inner volume of the diode. An energy deposit in the volume creates electron-hole pairs, proportional to the amount of energy released. The electric field causes the electrons and the holes to travel to the respective electrode. With an external circuit, the resulting pulse can be measured. An appropriate calibration measurement translates the pulse height to the actual deposited energy. Typical resolutions of 1‰ can be reached for energies up to 8 MeV.

3.4.2.2 Phase II detectors

The detectors for Phase II are so called BEGe (**B**road **E**nergy **G**ermanium) detectors. These detectors have a pin contact instead of the borehole of standard germanium detectors (fig. 14). Due to this pin contact, the electric field inside of the detector is more inhomogeneous, therefore one can get a spatial resolution due to different drift times for the different production sites. As the energy of a $0\nu\beta\beta$ event is released within a small volume, it is typically a so-called single-site event (SSE), whereas a γ will most probably deposit its energy through several interactions within the detector, so it is a multi-site event (MSE). Due to the inhomogeneous electric field, the shape of the signals from SSE would differ from MSE signals, thus, the MSE signals are easier to be rejected than in the Phase I detectors. This directly leads to a better background discrimination.
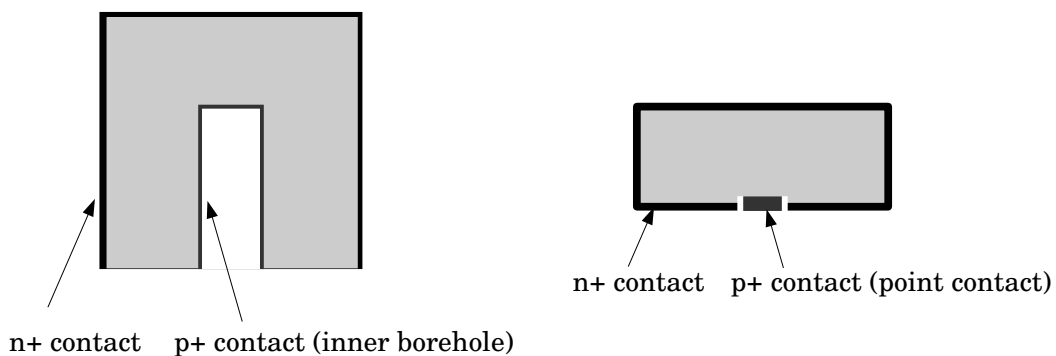

n+ contact   p+ contact (inner borehole)

n+ contact   p+ contact (point contact)

Figure 14: A schematic drawing of an coaxial germanium detector on the left and a BEGe detector on the right.

3.4.3   Background issues

To reach the proposed sensitivity of 10^{-2} cts/(keV·kg·y) in Phase I and the even more ambitious 10^{-3} cts/(keV·kg·y) in Phase II, understanding and rejecting the background play a crucial role for all ultra low statistics experiments. Basically, one has to distinguish between intrinsic and external background.

3.4.3.1   Intrinsic background

The intrinsic background of the germanium detectors are decays of radioactive isotopes of germanium as well as their daughter nuclei. For example, ^{68}Ge is cosmogenically produced. Its γ's are a typical background contribution in germanium detectors. To get rid of it, or better, to prevent cosmic radiation to activate the germanium detector, a huge effort is undertaken keeping the exposure of the material to cosmic rays as short as possible. Already during production of the detectors, especially during enrichment in ^{76}Ge, it was possible to remove most of the ^{68}Ge content. The material is stored underground and only brought to the surface, when there is really a need. For example, the metal for the diodes has to be brought from Europe to the U.S. for crystal pulling. A flight with an airplane is not possible, since in 10 km height, the activation due to cosmic rays is already too high. To bring the germanium metal to the U.S. (and the crystals back to Europe), a container ship will be used. There, the container with the germanium metal surrounded by a massive shielding will be stored below deck, as deep as possible.

3.4.3.2   External background

External background is background which does not originate from the germanium detectors themselves. The material surrounding the detectors for example has to be selected and screened carefully for radioactive containments to reduce the external background. Each single batch of screws, the copper used for the crystal holders, the cables as well as the stainless steel for the cryostat itself was screened. The closer the material is to the detector, the more severe a radioactive contamination would impact the background. Even though the stainless steel for the cryostat is well below the specified limit of 10 mBq/kg [Man08], it was decided to add copper plates (15.8 t) on the inner wall of the cryostat to shield against γ's from the steel. In addition, cosmic rays can contribute to the external background. This can be either directly while passing the detectors, or via secondary particles which are produced close to the detectors. But foremost, the Gran Sasso itself acts as a shield against cosmic rays.

3.4.3.3   Background reduction

Once having an "as clean as possible" setup, the remaining radioactive sources and muons are still producing background events. Thus, active background reduction techniques have to be developed to push down the background limit. As $0\nu\beta\beta$ events are SSE (Single Site Events), a first step is to perform an anti-coincidence cut between the detectors. This eliminates all events with energy deposition in more than one detector. In addition, pulse shape analysis (PSA) can be performed. Events with energy deposition in one detector still can be background. For example, a γ could deposit energy in different spots inside one detector until its total energy is deposited. Thus, if it is possible to discriminate between such so called MSE (Multi Site Events) and SSE, this also

leads to a reduction of the background. Fig. 15 shows the detector charge pulse of a typical SSE in comparison to a typical MSE, further details on PSA are found in [Bud09].
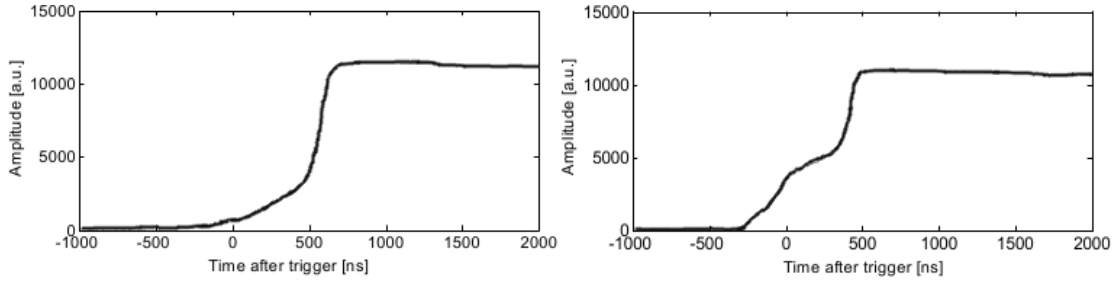

Figure 15: On the left side, a detector charge pulse of a single site event is shown, on the right: detector charge pulse of a multi side event. Fig. from [Bud09].

As muons also contribute to background, it is necessary to suppress their contribution. The muons at LNGS have an average energy of 270 GeV and such a muon can easily deposit 2 MeV in one interaction point at one detector, simulating a $0\nu\beta\beta$ signal. In addition, even without depositing energy directly, a passing muon can produce a secondary particle, for example a fast neutron close to the detector, which then could deposit energy in the detector. Simulations showed, that without a muon veto, the background induced by muons would be $6.4 \cdot 10^{-4}$ cts/(keV·kg·y) [Kna09]. Aiming for an overall background index of 10^{-3} cts/(keV·kg·y), this means, the background induced by muons would contribute already more than half of the tolerable background. Thus, an active muon veto is needed to reach an overall background index of 10^{-3} cts/(keV·kg·y) or even less.

3.5   GERDA-phases

Intentionally, it was planned to run GERDA in several phases:

- **Phase I:** around 18 kg of enriched Ge-detectors (15 kg of ^{76}Ge) will be run for one year data taking (i.e. an exposure of 15 kg · y). With an assumed background of 10^{-2} cts/(keV·kg·y), the limit on the halflife could be pushed to $T_{1/2} > 3.0 \cdot 10^{25}$ y with 90% C.L., if no $0\nu\beta\beta$ exists. The claim of Klapdor-Kleingrothaus $T_{1/2} = 1.19 \cdot 10^{25}$ y [KK04] would be ruled out with 99.6 % C.L.; in the case, that the claim is true, one expects 6.0 ± 1.4 events in the region of interest.

- **Phase II:** new enriched Ge-detectors will be added to the setup, and a background index of 10^{-3} cts/(keV·kg·y) should be reached. 100 kg · y of data will be collected within 2-3 years. If there is still no $0\nu\beta\beta$-event detected, this would lead to an increased lower limit of the halflife time to $T_{1/2} > 2 \cdot 10^{26}$ y [Abt04].

- **Phase III:** the next step would be to add many more Ge-detectors (in the range of 1 t) to gain more exposure, and also the background reduction becomes more and more important. As this is also increasingly expensive, an experiment in such scale would need a world wide collaboration. There are plans to combine GERDA and Majorana (a similar experiment in the U.S.) to such a large scale $0\nu\beta\beta$-experiment.

Meanwhile, the development of the BEGe detectors made such progress, that it was decided to deploy the newly fabricated enriched detectors as soon as they are available. Thus, phase I and phase II are no more strictly separated phases.

3.6 Commissioning

The inauguration of GERDA took place in Nov. 2010. The first 3-detector string was submerged into the argon. All three detectors were standard, natural germanium detectors from GTF. These detectors were used for a full chain test of the whole GERDA setup, and to get a first look at the background level. In addition, since June 2011, the first enriched germanium detectors are submerged. For using them in the GERDA experiment, these detectors had to be refurbished.

During the commissioning runs, an unexpected background arose. A line at 1525 keV became visible. Most probably, it belongs to the decay of ^{42}K to ^{42}Ca in the liquid Argon. ^{42}K is a daughter nucleus of ^{42}Ar, whose contamination was expected to be less than $4.3 \cdot 10^{-21}$ g/g at 90 % C.L. [Ash03]. However the measured contamination is somewhere between $1.6...2.6 \cdot 10^{-20}$ g/g [Sch11] (if the ^{42}K is distributed homogeneously), which is in fact four to eight times higher than assumed in the proposal. Nevertheless, there might be the possibility, that ^{42}K-ions are attracted by the electrical field around the detectors. Thus, a smaller contamination could lead to a higher observed count rate.

$$^{42}Ar \xrightarrow{\beta,\ 600\,keV,\ 33\,y}\ ^{42}K \xrightarrow{\gamma},\ 1525\,keV][\beta,\ 3.5\,MeV,\ 12\,h\ ^{42}Ca \tag{3.1}$$
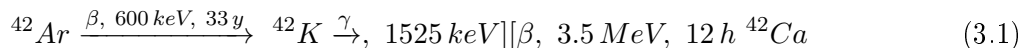
The γ-line of the ^{42}K decay is at 1525 keV, so well below the Q$_{\beta\beta}$, but it is accompanied by a β^- decay with an endpoint energy of 3.5 MeV (Eqn. 3.1 shows the β decay scheme). Thus, it is a crucial task to get rid of the ^{42}K. As the design of GERDA does not foresee to exchange and purify the Argon, it is still under investigation how to decrease the amount of ^{42}K at least close to the detector. Several possible solutions were proposed. For example the idea was tested to read out the detector at the outer surface instead of reading out at the borehole (i.e. the polarity of the HV was switched), to push away ^{42}K ions. But this leads to more noise, so the energy resolution was worse. Another idea was to put a "minishroud" around the string of detectors. This ultra thin tube of copper foil could then be set on a chosen voltage to drift the K-ions away from the detectors.

3.7 Physics run

Since 23rd of June 2011, the first three enriched detectors are submerged in the cryostat and the first data aiming for $0\nu\beta\beta$ is being taken. In addition, three natural germanium detectors are deployed to monitor the background. Soon, a technical report will be published in NIM A, and the first experimental data are expected to be published in 2012.

3.8 The GERDA Collaboration

The GERDA collaboration consists of 19 institutes in seven countries. At the moment, 111 people (physicists, engineers) are working for GERDA in these institutes:

- INFN Laboratori Nazionali del Gran Sasso, LNGS, Assergi, Italy

- Institute of Physics, Jagellonian University, Cracow, Poland

- Institut für Kern- und Teilchenphysik, Technische Universität Dresden, Dresden, Germany

- Joint Institute for Nuclear Research, Dubna, Russia

- Institute for Reference Materials and Measurements, Geel, Belgium

- Max Planck Institut für Kernphysik, Heidelberg, Germany

- Dipartimento di Fisica, Università Milano Bicocca, Milano, Italy

- INFN Milano Bicocca, Milano, Italy

- Dipartimento di Fisica, Università degli Studi di Milano e INFN Milano, Milano, Italy

- Institute for Nuclear Research of the Russian Academy of Sciences, Moscow, Russia

- Institute for Theoretical and Experimental Physics, Moscow, Russia

- Russian Research Center Kurchatov Institute, Moscow, Russia

- Max-Planck-Institut für Physik, München, Germany

- Physik Department E15, Technische Universität München, Germany

- Dipartimento di Fisica dell'Università di Padova, Padova, Italy

- INFN Padova, Padova, Italy

- Shanghai Jiaotong University, Shanghai, China

- Physikalisches Institut, Eberhard Karls Universität Tübingen, Tübingen, Germany

- Physik Institut der Universität Zürich, Zürich, Switzerland

To coordinate the work in such a relatively large collaboration, the GERDA group is subdivided in different task groups. Each task group is dealing with a specific task i.e. for R&D, construction, analysis. This is needed to guarantee smooth running conditions during construction and the experimental run. All together, 13 task groups were defined by the collaboration:

- TG01 - Modification and test of existing diodes

- TG02 - Design and production of new Ge diodes

- TG03 - Front end electronics

- TG04 - Cryostat and cryogenic infrastructure

- TG05 - Clean room and lock system

- TG06 - Water tank and water plants

- TG07 - Muon veto

- TG08 - Infrastructure and logistics

- TG09 - DAQ electronics and online software

- TG10 - Simulation and background studies

- TG11 - Material screening

- TG12 - Calibration

- TG13 - Data management and quality

Within this thesis, there were contributions to the following three task groups:

- **TG07 - Muon veto**
  As the name of this task group (TG) is already suggesting, this TG has to deal with everything, what is of concern to the muon veto. Namely, the design, construction and data acquisition of the Cherenkov veto (not the water tank itself, but the internals) and of the scintillation veto were the main tasks. The TG07 is a joint venture of the Eberhard Karls Universität Tübingen and the Joint Institute for Nuclear Research in Dubna.

- **TG09 - DAQ Electronics and online software**
  Of course, the DAQ of the muon veto is not only part of TG07, but also part of TG09. This task group considered the setup of the electronics part of GERDA. Here, it was decided, which FADCs have to be taken, where the data will be stored, what kind of database for the slow control (the control of basically every parameter for the running experiment) should be used. The main contribution to this group came from the Max Planck Institut für Kernphysik in Heidelberg for the DAQ electronics and the INFN in Padova for the slow control.

- **TG13 - Data management and quality**
  This task group was added, when the first measurements were performed in the GERDA setup. As of now, all groups wanted to get insight into the data, a clear data structure had to be defined, as well as the question about blinding of the data arose. This TG is strongly influenced by simulation studies of the experiment, since for comparison reasons, the GERDA data should be treated in the same way as the simulated data.

Chapter 4

The GERDA muon veto

To get rid of background caused by muons, one has to identify the muons. This can be achieved in different ways. In GERDA, the main part of the muon detector is a huge stainless steel tank, filled with ultra pure water and equipped with light detectors, sensitive for Cherenkov radiation. The Cherenkov detector has a "blind spot", namely the cryostat's neck. To cover this blind spot, so-called plastic scintillator panels, equipped with light detectors are mounted above the clean room. This is called the scintillation detector. In this chapter, the basic principles of muon detection will be described, and the muon veto of GERDA will be explained.

4.1 Detection principles

4.1.1 Scintillation

As muons are charged particles and as they have high energies, one can exploit the scintillation effect to detect them. If energy is deposited in the scintillation medium, a part of this energy is emitted as light. The amount of the light emitted is linear dependent on the deposited energy. This light can be used to determine the overall energy of the incident particle. There are several kinds of scintillators, for example scintillator crystals such as NaI or $CaWO_4$. Some liquids and also some plastic materials are good scintillators. In all scintillation materials, there are several energy transitions between atomic, molecular and/or crystal energy levels. If energy is deposited, several electrons are excited to higher energy levels. By de-excitation, light is emitted. Typically, the energy resolution is at a $>5\%$ level, as it is shown in [Mos05] and [Bar11c].

4.1.2 Cherenkov effect

As explained in Chapter 2.4.2, the medium energy of muons reaching the experimental halls of LNGS is in the range of 270 GeV. Thus, muons traversing the water tank of GERDA are highly relativistic. Their velocity is well above the phase velocity of light in water. Through Cherenkov effect, around 270 photons are produced for a 1 cm track of a muon.

4.2   The GERDA scintillation detector

In GERDA, plastic scintillators located on the roof of GERDA are covering the neck of the cryostat, since this is a possible "blind spot" of the water Cherenkov detector. The volume of the scintillation detector consists of 36 modules, each with a $3 \times 50 \times 200 \, \text{cm}^3$ plastic plate and an electronics board (additional $20 \, \text{cm}$ of space) at one of the short ends (see fig. 16). The electronics board houses a 1" PMT, electronics to transform from $12 \, \text{V}$ supply voltage to the needed high voltage in the range of $800 \, \text{V}$ and the electronics for a first data processing such as a leading edge discriminator and an amplifier and shaper to fit the pulse shape to the FADC sampling rate. The light from the scintillator plate is fed to the PMT through optical fibers attached to the long sides of the plate. These 36 modules are stacked in 3 layers with 12 panels each, while the inner part of the uppermost layer is rotated by 90° to obtain a pixilation (fig. 17). In total, the horizontal cross section is $4 \times 3 \, \text{m}^2$. These scintillator modules were built at JINR in Dubna, Russia.
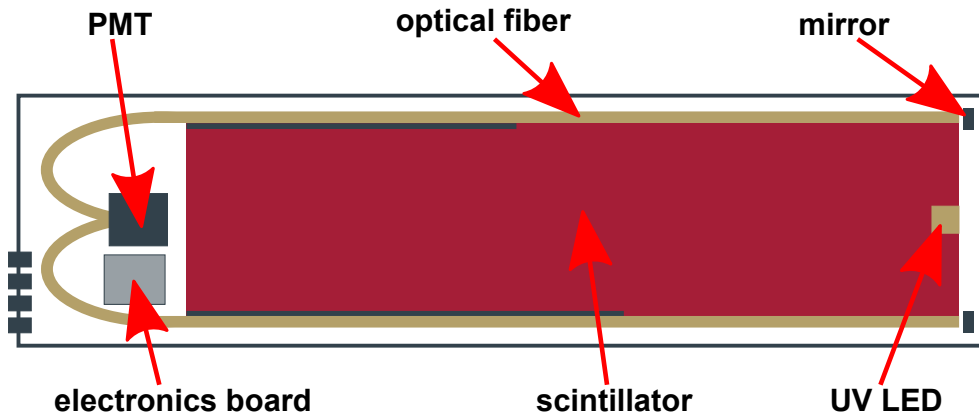
Figure 16: schematic drawing of one plastic panel. The electronics board houses electronics to shape and amplify the signal to fit the sampling frequency of the FADC as well as electronics to transform the $12 \, \text{V}$ input voltage to $800 \, \text{V}$ high voltage for the PMT. At the far end of the panel, a UV LED is built in to calibrate the light output. A throughgoing muon causes light in the plastic panel, which is then lead via optical fibers to the PMT. Fig. from [SZ08].

From November 2010 to July 2011, a preliminary setup was used. Only 7 panels were placed on the roof of the GERDA clean room, three stacks of two panels and one single panel. The analysis shown in Chapter 8 relies on this setup. Test measurements with this setup revealed that two layers are not enough to discriminate γ radiation and muons. So it was decided to use a three-layer setup which is seen in fig. 17. This was accomplished in July 2011, since August 2011, the full plastic veto setup is operational.

4.3   The GERDA water Cherenkov detector

The big water tank, which is surrounding the cryostat is filled with ultra pure water ($580 \, \text{m}^3$). The inner wall of the water tank, the bottom plate as well as the outer wall of the cryostat are covered
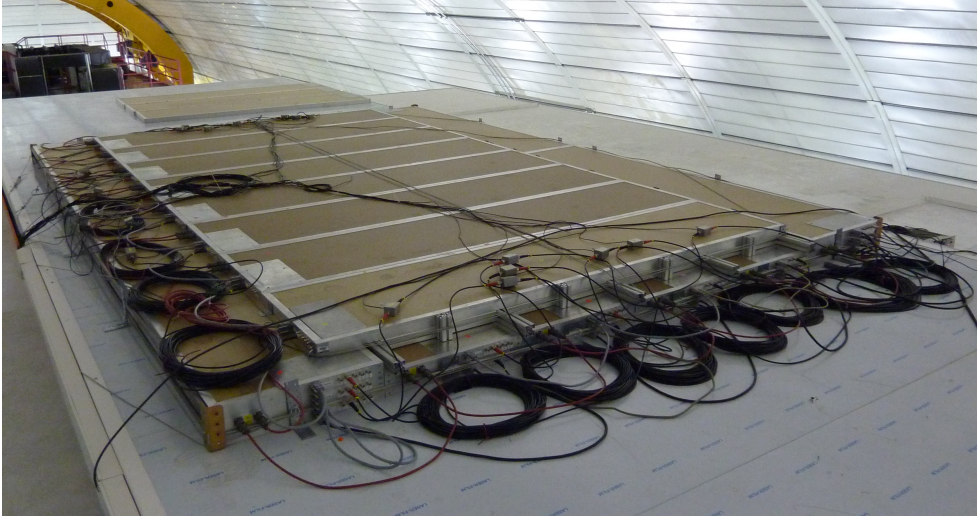
Figure 17: picture of the 36 mounted plastic scintillators. Picture from [Fre11].

with a highly reflective foil VM2000[1], which in addition acts as wavelength shifter (relevant details are given in Tab. 3).

As the reflectivity is $> 90\%$ in the bandwidth from 400 to 775 nm, an optical photon has a high chance to be reflected, and in addition, a UV photon has a good probability to be absorbed and re-emitted as an optical photon. With that, one increases the possibility to detect photons, but one also loses directional information due to the reflections. Nevertheless, the increased number of optical photons (either due to reflection or wavelength shifting) pays for the loss of angular resolution.

4.3.1   PMTs

To detect photons, the water tank is equipped with 66 8" photomultiplier tubes (PMTs) from ETL (9350KB and 9354KB [ET a, ET b]). Those PMTs consist of an evacuated glass bulb, which holds the photocathode. Inside the glass bulb, several electrodes ("dynodes") are located, as well as some focusing electrodes. All these electrodes are connected to an electronics base, where the voltage divider is located. A photon hitting the cathode can free an electron via the photoeffect. Due to the voltage divider, the following dynode is on a positive potential, accelerating the electron towards the dynode. Arriving at the dynode, the electron gained enough energy to release several electrons (in the order of two to five). Subsequently, from dynode to dynode, an avalanche is started, which results in a current pulse on the anode in a range of some tens of milliampere, with a duration of typically 10 to 50 ns.

In figure 18 the so-called quantum efficiency as function of the light wavelength is plotted. As one can see, the PMTs are most efficient in the blue region (around 420 nm), leading to a quantum efficiency of maximal 30%.

To submerge the PMTs in water, one has somehow to prevent the water reaching the electronic

---

[1]VM2000 is also known as Daylighting Film DF2000MA from 3M

Table 3: Properties of VM2000 [3Ma].

Characteristics	Value	Test by
Luminous reflectivity	$> 99\%$	ASTM E1164-02/ E308-01
Bandwidth for 90% reflectivity (0 to 80° angle of incidence)	$400 - 775\,\mathrm{nm}$	3M
Wavelengths transmitted (0 to 80° angle of incidence)	$> 775\,\mathrm{nm}$	3M
Wavelengths absorbed	$< 400\,\mathrm{nm}$	3M
Useful angle	$0\ to\ 90°$	3M
Total Thickness (nominal) Film Adhesive Liners (protective and adhesive)	$206\,\mu\mathrm{m}$ $66\,\mu\mathrm{m}$ $38\,\mu\mathrm{m}$ $102\,\mu\mathrm{m}$	3M
Total Density (film, adhesive and liners)	$0.25\,\mathrm{kg/m^2}$	3M
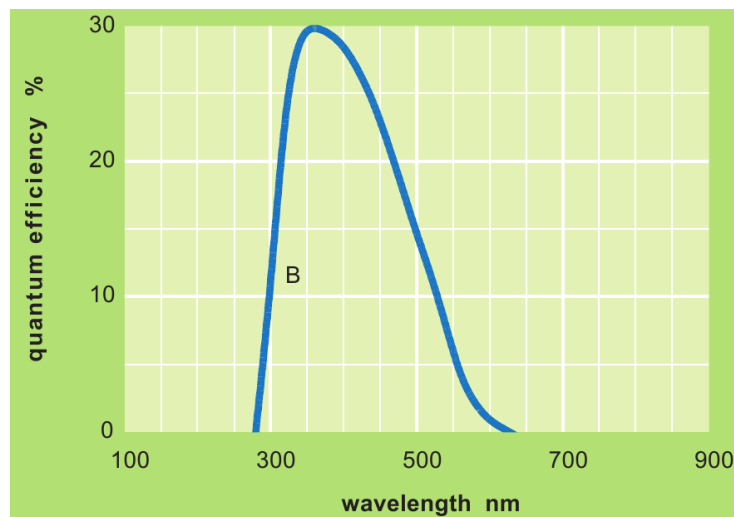
Figure 18: The quantum efficiency of a PMT. Fig. from [ET a].

contacts. The GERDA collaboration could profit from the developments by the Borexino[2] col-laboration. The capsules developed were slightly modified in comparison to the Borexino design (fig. 19, [Kna09]). It consists of a stainless steel housing, a cone attached to a cylindrical part with two fixation holes at the bottom plate. On top, a PET hat locks the volume, offering a window, where the light can be transmitted to the photocathode. A feedthrough for the high-voltage underwater coaxial cable RG 213/U[3] is leading directly into the volume. The electrical base is connected to the high voltage cable. To keep the PMT in position, the base is fixed with polyurethane. As additional water blocking, silicone is filled to a height above the electrical contacts. The remaining volume is filled with mineral oil to get a smooth transition from water through PET, mineral oil and the glass of the PMT to the photocatode.
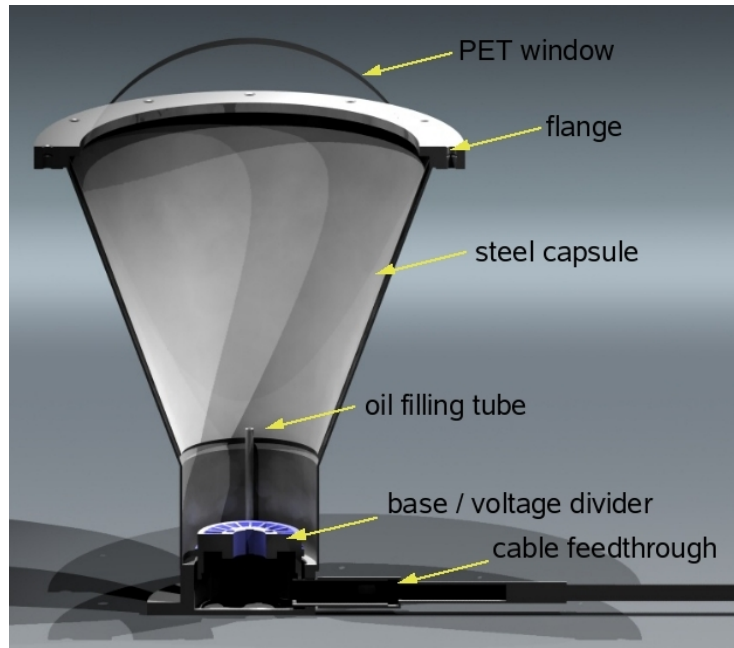
Figure 19: Schematic drawing of the Cherenkov veto PMT. For clarity, the PMT, the oil and the silicone are left out.

The PMTs were encapsulated and tested in Tübingen. Some prototypes were produced to test the under water functionality over several months and years. A detailed description can be found in the corresponding thesis [Kna09].
6 of these PMTs are distributed in the volume below the cryostat, the so-called "pillbox", 20 PMTs are located in two rings on the bottom plate of the water tank. The remaining 40 PMTs are mounted on the wall of the water tank, in four rings with 10 PMTs each.
The only connection to the outside is permitted through a 35 m long underwater high-voltage coaxial cable. In the electronics room of GERDA, a splitter box divides the high voltage and the signal pulses by appropriate band pass filters. As the high voltage is a DC current, and the signal

---

[2]http://borex.lngs.infn.it/
[3]JOWO RG213C/U

pulses is a combination of several AC current with different frequencies, the filter blocks the DC current to the "signal out", while the AC currents are blocked for the "HV" out. For calibration and functional tests, each PMT is connected to one optical fiber. As a second calibration system, and to study temporal behaviour, five diffuser balls are mounted inside the water tank. These "light bulbs" were produced in Tübingen to serve as point-like light sources in the water tank. One of these diffuser balls is mounted in the volume beneath the cryostat, while the other four are in the outer water tank at a height of around 4 m, shifted to each other by 90° (for details see Chapter 7).

4.3.2   Nomenclature

For numbering the positions, a nomenclature was defined. The position numbers consist of three digits. The first digit defines the ring, in which the PMT is positioned. "1" is reserved for the pillbox, "2" stands for the inner ring on the bottom and so on, ending with "7" for the uppermost ring on the wall. The next two digits describe the radial position on the ring, starting with "01" for the first position with an angle of more than 0°. 0° is defined by the simulation tool MaGe, pointing from the central point of the GERDA-cryostat perpendicular to the elongation of the Hall A towards the L'Aquila side of the mountain. For the water tank, this means, that 0° is defined by the manhole. Thus, the very first PMT is "101", which is a pillbox PMT. The very last number is "710", the PMT at 650 cm height and an angle of 360. Figure 20 shows the position of each single PMT. In Appendix II, all data for the PMTs installed at LNGS are listed.

Wall

PMTs inside Watertank

Bottom
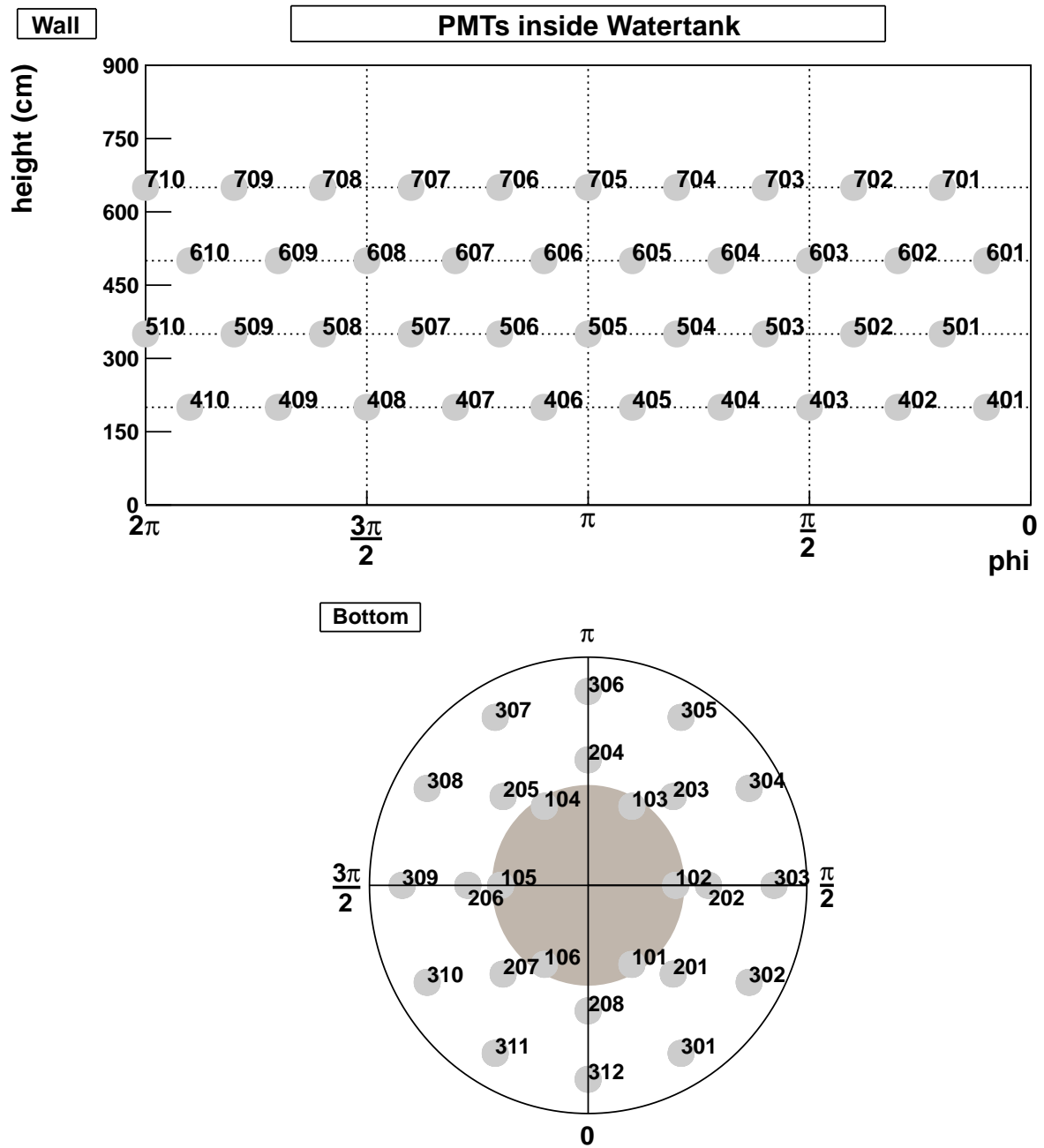
Figure 20: Schematic for the nomenclature of the PMTs position.

Chapter 5

The muon veto DAQ

The main part of the data acquisition system (DAQ) of the GERDA muon veto consists of 14 Flash-ADCs (FADC) SIS3301. Each FADC houses eight channels with a sampling rate of 100 MHz. These fast analog to digital converters digitize the analog pulse to a column of digital data. The choice for these FADCs was due to the fact, that the same FADCs are already used for the Germanium DAQ in Phases I and II. The 66 PMTs of the water tank are distributed on the FADCs in such way, that next neighbors are on different FADCs. This grouping helps in identifying a muon event, since a muon should then lead to a light flash in different FADCs, leading to a relative easy way to trigger on a muon.

For the scintillation veto, a slightly different approach was chosen. Since the four remaining FADCs only can house 32 individual channels, the best solution was to combine two of the 36 single panel signals from one layer to one signal, delaying one of the signals by 150 ns. Now, only 18 channels are left, six channels per layer. These six channels were plugged into one FADC each, so, in total, the scintillation veto needs three FADCs. This chapter starts with the hardware setup of the DAQ, then describes the DAQ program developed in Tübingen. Finally, the DAQ software used at LNGS will be explained in detail, and some first events will be shown.

5.1 Hardware setup

For developing the DAQ system, several constraints were given:

- Each PMT should be read out separately to have the possibility to get individual information such as for example trigger rate and gain.

- The same FADCs as for the Phase II Germanium system should be used to have a kind of "standard" electronics.

- As a common electronic interface, VME was decided.

- A trigger system should be developed by using as few additional modules as possible.

- If possible, the plastic scintillators should be read out with the same setup.

5.1.1   NIM and VME

There are several different standards of electronic modules used in particle physics. Such a standard defines both mechanical and electrical specifications for electronic modules. For example, in nuclear and particle physics the NIM-Standard (Nuclear Instrumentation Module) is widely used. This was the first such standard, defined at the end of the 1960's. The backplane of a NIM crate supplies $\pm 24\,\mathrm{V}$ and $\pm 12\,\mathrm{V}$ (in some case also $\pm 6\,\mathrm{V}$), but the modules cannot communicate with each other through the backplane. In the NIM standard, also cable specifications and levels for logic signals are defined. For fast logic signals, the **NIM logic** is a current based logic, with negative true (-14 to -18 mA at $50\,\Omega \,\hat{=}$-0.7 - (-0.9) V) [ORT]. Although the standard is rather old (developed in the 1960's, defined in 1968, revised in 1990), it is still widely used due to the robust design. Standard modules are for example amplifiers, discriminators and pulse generators.
But with the development of micro-controllers, new systems with interacting modules became possible.
In the year 1979, Motorola developed the VERSAbus, a standardized bus system for their new 68000 CPU. Later, they added mechanical specification based on the eurocard standard. This joint venture then was called VMEbus (**V**ERSA**m**odule **E**urocard bus), defined in ANSI/IEEE 1014-1987. This original standard was a 32 bit-bus, using the Eurocard DIN connectors. In the meanwhile, several additions to this standard have been made, for example to allow wider bus widths and faster data transfer rates. At the moment, VME2eSST is the current standard. It allows 64bit-data access with a bandwidth of up to $320\,\mathrm{MB/sec}$.
The modules communicate with each other through the VME backplane, where one module is the master module. This master is either a module housing a CPU onboard, or it is connected via cable or optical fiber to a PC. A VME crate can house up to 21 modules, daisy-chaining of these crates offers a much more complex setup.
Of course, there are VME modules, which are offering the same functionality as NIM modules, such as amplifiers, discriminators. With the possibility of communication between different modules via the backplane, new connections were made possible. By using micro-controllers and FPGAs, a variety of operations on single boards is possible. This opened a new window in data handling such as processing online, storage and so on.
Several other standards are used in particle and nuclear physics such as CAMAC or PXI, but since those were not used in this work, they are not further described here.

5.1.2   The FADCs

The type of FADCs used are SIS 3301 from Struck [Str04]. Each of these VME modules houses 8 analog input channels and 8 digital input/output channels. The sampling rate is $100\,\mathrm{MHz}$, which means, the input signal is digitized every $10\,\mathrm{ns}$. In the following, a "clock tick" means one of these time steps. The analog value is digitized in 14 bits, so, the voltage range (here $\pm 1\,\mathrm{V}$) is converted in values between 0 and 16.383. For triggering, the FADC offers a FIR (**F**inite **I**mpulse **R**esponse) trigger on each channel, but only an OR-ed logical signal of all eight trigger signals is given to one output channel. The FADC delivers online the information, that **at least** one channel has fired, but neither which one nor how many. To get the information, which PMT has fired, this can only be retrieved offline by having a look at the data.

5.1.2.1 FIR filter

A trapezoidal FIR filter is implemented on the module for trigger generation. The user chooses a trigger window (w), a trigger gap (g), both in units of clock ticks. In addition, the user sets a trigger value (v, in ADC channels). There are two running time windows generated. Both have the width w, and the distance between both starting points is g (fig. 21). The module sums the digitized signal values within the windows separately and the difference of the sum gives the actual filter value. As this is done for each sampling step, the resulting curve of the filter values has a trapezoidal shape.

Does the filter value exceed the trigger value v, a rectangular trigger signal is created, fig. 21 shows a visualization of the two moving windows.
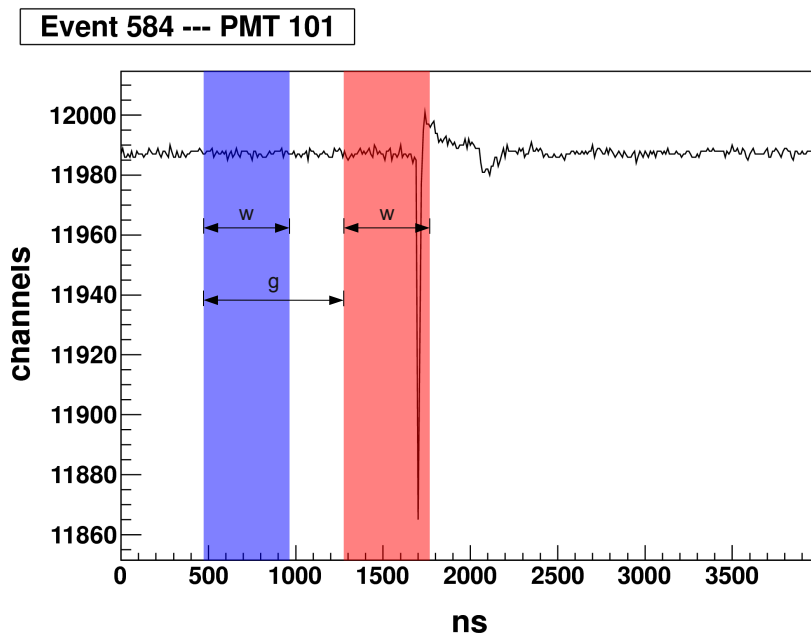
Figure 21: Example for FIR trigger. The red and the blue shaded area are the two windows of w clock ticks width, also the gap g is shown.

5.1.2.2 Memory banks

The FADCs have two memory banks with 2 MB each (8 channels · 128k samples · 16bit = 2 MB). With these modules, it is possible to read out the first memory bank while the second bank is ready to record data, leading to an almost dead time free readout. With one bank, one can record 128k clock ticks. At a sampling rate of 100 Mhz, a maximum record length of 128 · 1024 · 10 ns = 1310720 ns or around 1.3 ms is possible for one event. In addition, one memory bank can be divided in several "subbanks", each "subbank" is then used for one event. With this possibility, one can save several events, before going to the second bank, which leads to an increase of the possible event rate, since the system still is armed and ready for data taking while the full bank

is read out. In Tab. 4, all possible setups are given.

The final setup for the GERDA muon veto is able to handle 32 events at once, which means, the memory bank was divided in 32 parts, and for each event, 40.960 μs are recorded.

Table 4: Possibilities to split the memory of the FADC in different events. In the first column, the number of sub-events are given, the second column is the number of clock ticks per event, while the right column is the calculated record length per event.

Events/Bank (Number of divisions)	Page Size	record length @100MHz (in ns)
1	128k	1310270
8	16k	163840
32	4k	40960
64	2k	20480
128	1k	10240
256	512	5120
512	256	2560
1024	128	1280

5.1.3   Trigger module

If the whole muon veto system would be read out every time when a single PMT had fired, there would be a tremendous amount of garbage recorded. But since muons produce signals in more than one PMT, a dedicated trigger logic had to be implemented. Of course, the easiest way would be to trigger on each single PMT. A minimum number of PMTs firing in a specified time range, or some PMTs firing with their next neighbors, is an acceptable trigger condition to identify a muon. However, with the FADCs, one gets a trigger information of the whole FADC ("one or more of the channels of FADC xy has fired"). But even the digital trigger signal of the entire FADC can be used to make a good triggering system.

If a muon passes the water tank, emitting Cherenkov light, one assumes to get signals in several PMTs spatially close to each other. By distributing the neighboring PMTs on different FADCs, one should find a muon, if several different FADCs are firing within a short time. To achieve this, and to distribute the PMTs in the best way, it was decided to use 10 FADCs. In that case, each FADC houses one PMT from each ring on the wall, two PMTs form the two bottom rings, and a part of the FADCs house one pillbox-PMT. The "Tübingen DAQ" used a discriminator module, which also creates a "majority" signal, if more than X FADCs fired at one time. In the final LNGS solution ("Heidelberg DAQ"), this is done by a custom made MPIC-module. This module, designed and built in Heidelberg, houses a FPGA[1], which is used for the trigger generation. The "trigger out" of the FADCs are fed into the module and the FPGA compares, if the amount of fired FADCs exceeds the chosen majority. This module is also used as external clock for all FADCs of the muon veto, so, each clock tick is present on each FADC at the same time, which means, that

---

[1]**F**ield **P**rogrammable **G**ate **A**rray - an integrated circuit, which is programmable

all internal FADC clocks are synchronized. And it also serves as GPS interface for the absolute time and runtime/lifetime registers [Kih11].

In the following two sections, both DAQ programs are explained more detailed.

5.2 The Tübingen DAQ program

During this thesis, a data acquisition program (DAQ) was developed in Tübingen. Intentionally, it was planned to be used only in GERDA Phase I to read out the Cherenkov muon veto, but it also was used in several setups in Tübingen, for example test facilities of PMTs, studies of decay chains of different Germanium isotopes and the behavior of scintillating crystals at different temperatures. The Tübingen DAQ consists of a VME crate housing 21 slots for a variety of modules and a controller card (CAEN V2718 [CAE09]). This card is practically an extension of the PC PCI-Bus, as it has to be connected with a PCI card (CAEN A2818 [CAE08]) via a duplex optical fiber pair. CAEN, the producer of the controller system offers all C/C++ and LabVIEW functions needed to interact with the VME-Bus. To identify the different modules plugged in, each module has to get its own base address. The C/C++ functions from CAEN then offer different options to access the modules, always depending on the base address and a specified subaddress. For the first tests, a small setup was installed with only one PMT channel to be read out. Several versions were developed. A very first version wrote a simple ASCII file for each event. This file is human readable, has 9 columns (one column with a running value, and one column per FADC channel). A "Zulassungsarbeit" [Oßw07] measuring scintillation properties at low temperatures with an optical cryostat was obtaining results with this program. A big step forward was the implementation of a binary storage on hard disc, since this lead to less storage space and in addition also to a higher readout speed (since the program is not delayed by disc access). This version of the program was also used and developed further in a diploma thesis at the optical cryostat [Str10] and is now used for experiments of another PhD thesis [Sai]. The objective of these theses was to investigate the scintillation properties of different crystals at temperatures from room temperature to 1.2 K for the CRESST experiment [Ang08].

But not only for studies for the CRESST experiment, but also for background studies for GERDA this program was or will be used. Neutrons originating from interactions of muons with material close to the GERDA setup could be captured by atoms in the germanium crystal, leading to an intrinsic background for the GERDA experiment. This issue was investigated by neutron activation of ^{74}Ge and ^{76}Ge. Also the data for this PhD thesis were obtained with this program [Mei10].

These experiments all were satisfied with reading out one single FADC. But for GERDA one needs to read out several FADCs simultaneously and therefore this possibility was implemented. In addition, the data can be written in ROOT format directly to the hard disk. The "trigger out" of the FADCs are fed into a Leading Edge Discriminator (described in chapter 6.1.1 [CAEa]), which offers a multiplicity trigger signal. This trigger signal (called "majority" in the manual) gets active, if an user defined number of channels are triggering within the chosen time window. A signal occurring in different FADCs will then lead to a rectangular output pulse of the Leading Edge Discriminator, which then is fed via a FIFO [2] into the stop-channel of the FADCs. This stops the digitization of this event. The next part of the memory bank is armed, waiting for the next trigger.

---

[2] **F**an **I**n, **F**an **O**ut; a multiplexing unit which copies the input signal on up to 16 output signals [CAEc]

While the Tübingen DAQ was used for tests in Tübingen, the setup at LNGS was equipped with the Heidelberg DAQ for compatibility reasons between the muon veto DAQ and the Germanium DAQ.

5.3 The Heidelberg DAQ program

The Heidelberg system uses a different VME system than the Tübingen system. It houses a built-in CPU in the VME system, i.e. the VME system is a PC on its own. The VME backplane is in principle used in the same way, as a PC uses the PCI chain. This offers a fast connection from the FADC to the storage unit. The output of the system is a tagfile. This file is so to say a "structured binary file". The informations about the setup like number of PMT channels, setup of the FIR trigger, clock source, starting time are stored in the very first part of the tag file, the header part. The number of stored events and the end time are stored within the footer part. In between, the data for each event are stored in the event part. Each event is structured in the same way, starting with the event number, the time, when the event triggered, and then, for each channel, the recorded data. Each kind of information is connected with a "tag", which is unique for the whole measurement. One of these packages of informations consists of three parts:

- tag: unique identification number (a 32 bit number)

- size: the size of data in bytes (a 32 bit number)

- data: the data itself (size $\times$ 32 bit)

To illustrate the principle, figure 22 shows a small sketch of the data structure. In this example, two tags are shown. Tag "101" defines the number of the event, the whole data belonging to this tag are 96bit: The first 32 bit contain the tag "101", the next 32 bit contain the amount of data to be stored, which is "one integer", and then, the data itself is again 32 bit wide. The second example shows the data for a hypothetical PMT channel, recording five clock ticks. Thus, the tag "31001", which defines the channel number is followed by a "20", giving the amount of data to be read in Bytes. Both these values are integers, thus 64 bit have to be read for this information. Then, the five values corresponding to one clock tick each, have to be read. In this example, 7×32 bit $= 224$ bit have to be read in total to get the trace of one channel.

5.3.1 The conversion tool

To get access to the data stored in the tagfile, a small program ("Tag2ROOT") was written to "translate" the tag-data into ROOT format. Basically, this tool converts the tagfile into two ROOT-trees:

tag	size in byte	value
101	4	123456
32bit	32bit	32bit

tag	size in byte	value				
31001	20	123456	123456	123456	123456	123456
32bit	32bit	5 x 32bit				

Figure 22: Example of the data structure. Here, two different types of data are shown. The first one is the typical structure for the event number, the Tag "101" is followed by a "4" indicating 4 Bytes to be read, followed by an integer number "123456". The other tag "31001" is the tag for the data from one channel. Here, the tag is followed by a "20", as the data consists of 5 x 4 Bytes = 20 Bytes, then the 20 x 32 bit follow.

the "headerTree" contains information about the run such as:

- start time, end time and the calculated recording time

- number of recorded events

- the event rate

- type of data (Cherenkov triggered, plastic veto triggered, gain measurement)

- number of PMT channels

- number of germanium channels

- number of plastic veto channels

- information about the trigger threshold setup for each type of channel

- setup of the trigger criteria (multiplicity)

- informations about the trace length

the "eventTree" contains information about each single event:

- number of event

- event time

- traces of all 66 Cherenkov PMTs

- pulse height, integral and hit time of each PMT

- was the individual PMT hit?

- how many PMTs fired?

- how many Pillbox PMTs fired?

- traces of all 36 plastic veto channels

- pulse height, integral and hit time of each plastic scintillator

- was the plastic scintillator hit?

- how many scintillator plates fired?

- integral signal in the water tank

- seconds since the last event

As at the end of July 2011, when the full setup of the plastic scintillator veto was completed, the DAQ at the LNGS was changed. Until then, seven plastic scintillators were read out, but since

August 2011, the full setup (36 plastic scintillators) is read out, the conversion tool was changed to handle the larger amount of scintillator data.

At the moment, the present tool allows a quick look on the muon data alone. A separate thesis is working on the implementation of the muon data into the overall GERDA data stream [Fre].

5.3.2   The display tools

A collection of several ROOT based programs and functions were developed to display single events, based on the data structure provided by the conversion tool. At the moment, these programs only can handle one data file. For the very first data, the start and stop of such a data run was done by hand. In the meanwhile, once a day, a new data file is started. Most of the programs are designed to plot single signal traces, or the behaviour of the water tank. A detailed description of the functions can be found in Appendix I, nevertheless, here just a very brief list will be given:

- PlotEvent:
  To plot a view on the water tank (muon map), giving a color- and size coded information about the light seen by each PMT.

- PlotTrace:
  To plot the trace of one PMT for one event.

- Traces:
  Basically the same as "PlotTrace", one can click through all traces of the PMTs.

- PlotRing:
  The traces of all PMTs belonging to one ring are plotted.

- PlotTracePanel:
  Traces of the panels of one pixel are plotted.

- PlotHisto:
  A histogram or the pulse integral of a user specified PMT is created.

- HistogramVariable:
  To plot histograms of different variables for one PMT.

- PlotHitTimeMultiplicity:
  A 2D-Plot, on x-axis is the number of fired PMTs (multiplicity), on y-axis the time, when the PMTs have fired.

- PlotIntegralMaximum:
  A 2D-Plot integral vs. maximum is plotted.

- CreateMovie:
  A .gif-movie is created, the event in a time sequence.

- CreateMovieEvents:
  A .gif-movie of several events is created.

Chapter 6

Calibration of the PMTs

One subject of this thesis was to define the individual voltages of each PMT to reach a gain factor of $2 \cdot 10^7$. Also, the dark rate of each single capsule was determined. In the following, the experimental setups and the results for both measurements are presented.

6.1 Gain measurement

The photomultiplier used in GERDA are of the ETL types 9350KB and 9354KB with a diameter of 8". These PMTs are capable of detecting single photons. As described in chapter 4.3.1, an incident photon may release an electron out of the photocathode due to the photoeffect. This electron is then accelerated to the first dynode due to a potential difference between the cathode and the dynode of typical 200 V. Having a higher momentum, the impact of this accelerated electron on the dynode releases typically two to five electrons which are again accelerated to the second dynode and so on. Thus, an avalanche is started. Assuming $N_e = 4$ electrons are released due to one impact electron, and assuming, the PMT has $n_{stages} = 12$ dynodes, one can estimate the typical gain factor of the PMT in:

$$G_{\text{theor}} = N_e^{n_{\text{stages}}} = 4^{12} = 1.7 \cdot 10^7 \tag{6.1}$$

Several millions of electrons are arriving at the very last electrode, the anode, causing a measurable current pulse. This current can be measured either directly or through the corresponding voltage pulse across a resistor of $50\,\Omega$. To determine the gain, one needs either a light source with known intensity, i.e. known amount of photons, or one can use the so-called dark pulses.

6.1.1 Dark pulses

The dark pulses are mimicking a single photoelectron. Dark pulses occur, if a thermal electron of the cathode has an energy higher than the work function in the bialkali cathode, so it can emerge, or an electron is emitted due to field emission effect. Such an electron will produce the same signal as a "real" photoelectron (p.e.). At ambient temperature, the rate of dark pulses is typically around some kHz for a PMT with 8" diameter.

To use these pulses for gain measurements, one has to split the signal of the PMT to obtain one signal for trigger generation and one signal to analyze. This is achieved with a FanIn-FanOut

(FIFO, CAEN V925 [CAEb]), which multiplexes 4 input channels on 4 output channels. In this case, only one input channel is present. One output is fed into a leading edge discriminator (as LED is very confusing with light emitting diode, in the following, always "LeadingEdge" is written for this device [CAEa]). This device delivers a rectangular signal, if an analog signal exceeds a given trigger threshold. A good value for the trigger threshold is a value around 1/4 single p.e., since with this threshold, one triggers on most of the dark pulses while suppressing signals due to noise coming from the electronics.

The second output signal is then fed into a charge integrating ADC[1], here a CAEN V265 [CAE03] was used. While a rectangular gate signal (from the LeadingEdge) is present, the ADC is collecting the charge of the signal, and at the end converts it into a 12bit value. For the V265, the gate signal has to precede the analog signal by at least 65 ns. A schematic drawing of the setup is shown in fig. 23a.

This measurement only works with a dark pulse present. To derive the gain, one also needs a "null signal", i.e. an ADC value for "no signal present". To get this, one can simply take a pulse generator to trigger the ADC at random times, with the same signal length as the rectangular signal used before.

6.1.2 LED measurement

In principle, the PMTs are capable to measure the gain with these dark pulses, but it turned out, that due to a relatively high noise on the signal, some PMTs were not able to detect single p.e. through the dark pulse measurement as their signals were too small in comparison to the noise. Thus they had to be measured by another technique. Therefore, a light source which emits a specific amount of light in a specific time window was used. In the best case, one should dim the light source to a single photoelectron level. A reasonable setup would be, to have around 90 % of the trigger times with no signal, and only 10 % with signal. If the light source is too bright, i.e. it delivers more than one photon per pulse, this would lead to a higher probability that also more than one photon reach the cathode, releasing photoelectrons and therefore, producing a higher signal.

The light source used is a bright blue LED, driven by an electronic driver. Almost the same LED driver is later used as driver for the calibration system onsite (see Chapter 7). The light of this LED is fed through an optical fiber, and the opposite end of the fiber is directed towards the photocathode. The light intensity of the LED is controlled by changing the supplied voltage.

Also in the LED driven measurements, the PMT signal is fed through the FIFO. But as the LED is already triggered by a rectangular pulse, this rectangular pulse is used as a gate signal for the ADC (fig. 23b).

If the LED is dim enough, it is obvious, that one gets both the single p.e. signal and the pedestal (no event) signal during one measurement.

6.1.3 Result

In fig. 24, some measurements of both setups are shown. On the left side, one sees measurements at different voltages for one PMT with the dark pulse setup. On the right side, another PMT was measured with the LED setup. For the dark pulse setup, one needs to measure the pedestal
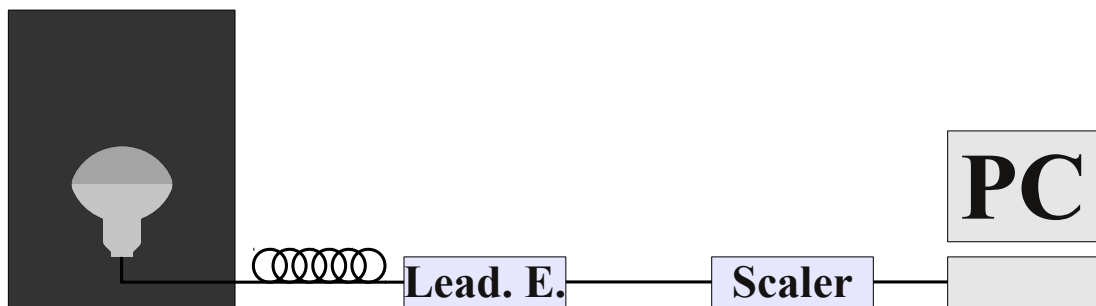
---

[1]Analog to Digital Converter
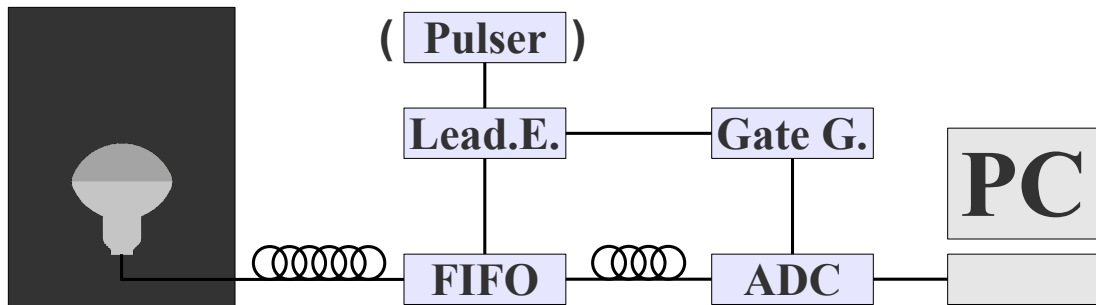
(a) Gain measurement with dark rate pulses
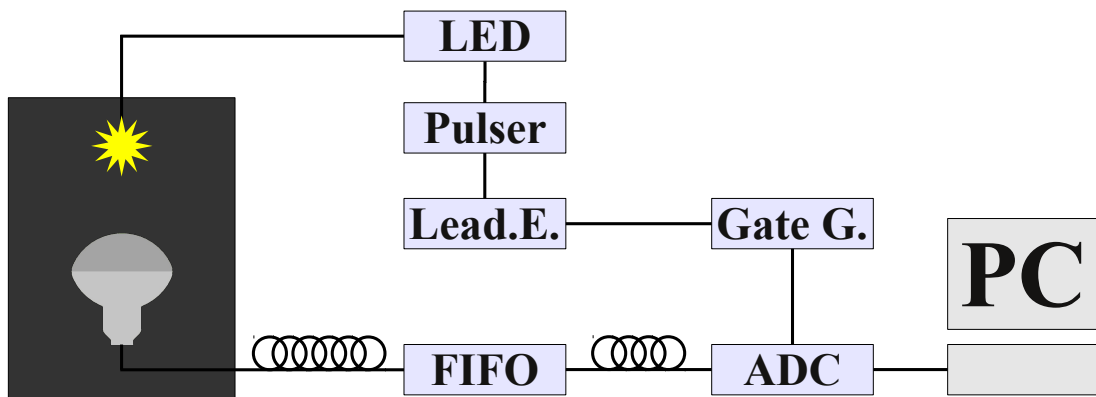
(b) Gain measurement with LED triggered pulses

(c) Dark rate measurement

Figure 23: All three setups for the different characterization measurements are shown. "Lead. E." is the trigger generator, a Leading Edge Discriminator; The "Gate G." is a gate generator to stretch the logic signal of the LeadingEdge, so that the full signal of the PMT fits in the gate needed by the ADC. For the right timing, a delay line is used from the FIFO to the ADC. In (a), the pulser is needed for the measurement of the pedestal.

with an external trigger (shown in red), as the signals always start at a given threshold, while the LED setup delivers the pedestal peak in addition. The pedestal signal stays at the same position for all different applied voltages, while the single p.e. peak shifts to higher ADC values for higher voltages.

(a) Dark pulse histogram   (b) LED pulse histogram
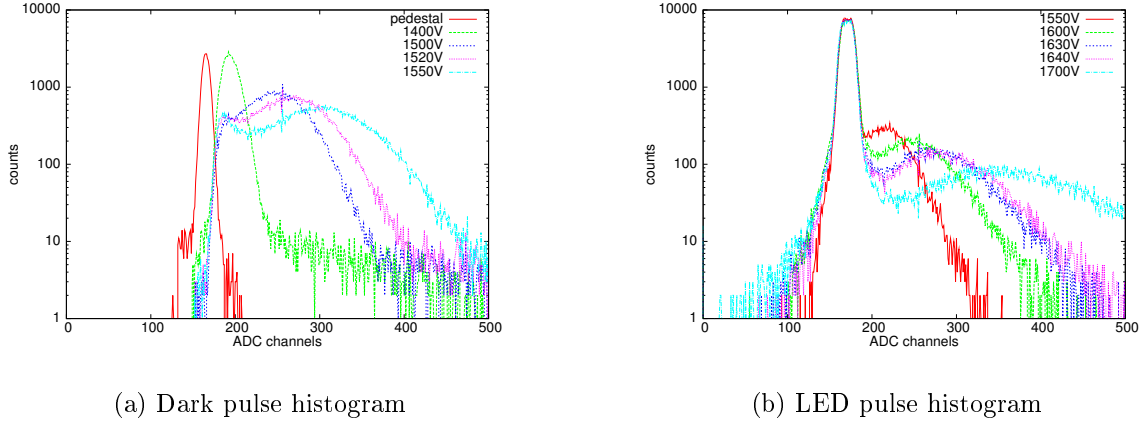
Figure 24: Two histogram plots for different PMTs. Left: dark pulse histogram, as the trigger is on the signal of the PMT, all histograms start at a fixed position right from the pedestal. Right: LED setup histogram, here, the pedestal is clearly visible in all measurements. On both plots, one sees that the single p.e. pulse is moving to higher values for a higher voltage supplied on the PMT.

As one can see in figure 25, the voltage supplied to the LED driver has to be chosen thoroughly, otherwise, one can get a non-negligible contribution due to double or multiple photoelectrons.
The gain of the PMT is calculated using equation 6.2, where Q_{meas} is the measured charge, N_e is the number of incident electrons and e is the charge of one electron. To get Q_{meas}, one has to calculate the position of the single p.e. peak with respect to the pedestal. This value (N_{ch}) is given in ADC channels, corresponding to the manual of the ADC used, a value of 120 pC is given for the whole range of 4096 ADC channels, so one ADC channel corresponds to 29.3 fC/ch. As single p.e. events were used for the measurement, N_e is equal to 1.

$$G = \frac{Q_{meas}}{N_e \cdot e} = \frac{N_{ch} \cdot 2.93 \ \cdot 10^{-14} C/ch}{e} = \frac{N_{ch} \cdot 29.3 \text{ fC/ch}}{1.6 \cdot 10^{-19} \text{C}} \tag{6.2}$$

In Tab. 5 on page 54, all PMTs are listed with their individual high voltage for a gain of $2 \cdot 10^7$, the histogram of the defined high voltages can be found in fig. 26.

6.2 Dark rate

The dark rate is the rate of pulses, which occur even if the PMT is in complete darkness. In the previous section, these pulses were called dark pulses. These pulses are always present, nevertheless, one can decrease the dark rate by lowering the ambient temperature. To measure the
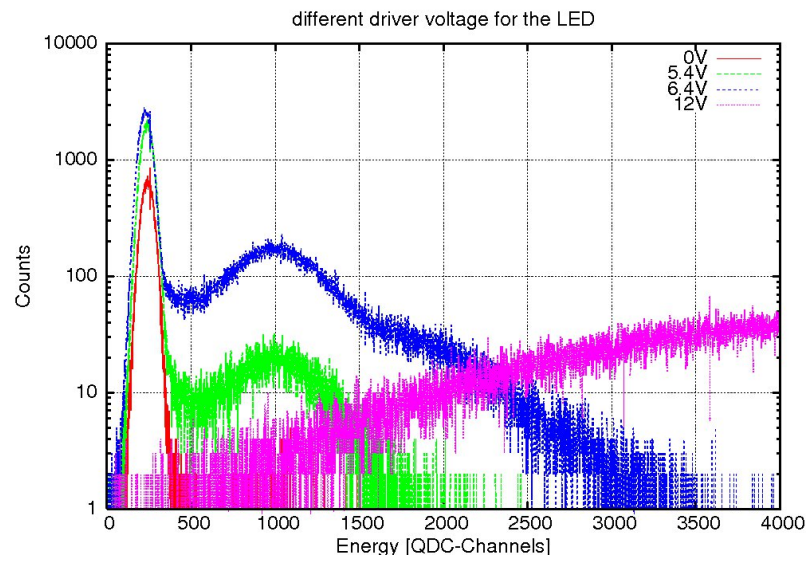
Figure 25: Response of one PMT for different supply voltages of the LED.
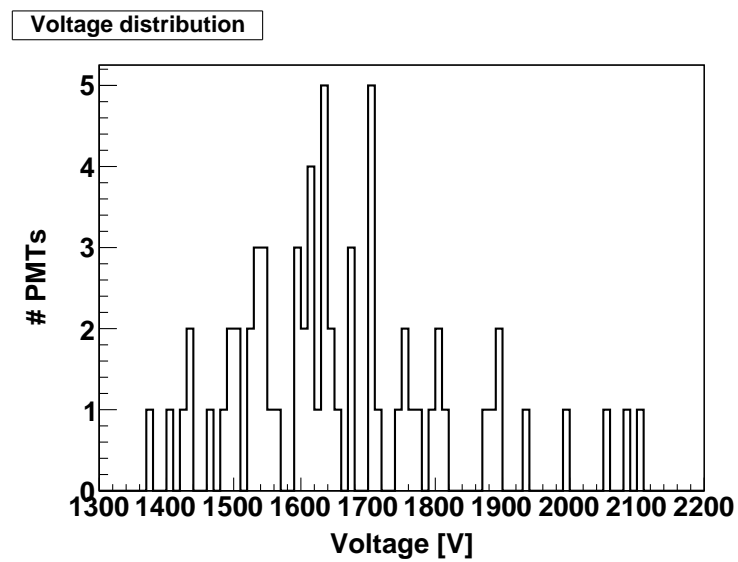
Figure 26: Histogram of the voltage supplied to reach a gain of $2 \cdot 10^7$.

dark rate, one has to ensure, that no ambient light reaches the PMT. In Tübingen, a darkroom was installed, the walls, floor and ceiling covered with black felt. This gives the opportunity to install the PMT in the room, close the door and start measurements without covering the PMT. To ensure the light tightness, the capsules were covered with 4 layers of thick black cloth.

The PMTs were supplied with high voltage (the voltage derived by the calibration measurement), and then the dark rate was measured for two minutes. The signal was fed into a LeadingEdge, and the threshold of the LeadingEdge was set to 1/4 single p.e. pulse height. With that value, one makes sure to trigger on most single p.e. signals while not triggering on noise. As the single p.e. peak was at around 30 mV, a trigger value of 8 mV was chosen. The rectangular trigger signal was then fed into a scaler (CAEN V560 [CAE02]), which counts the number of pulses, a sketch of the setup is shown in fig. 23c. The two minutes measuring time was divided in 5-seconds bins to see, if the rate is stable, or if there is an additional structure visible (fig. 27).
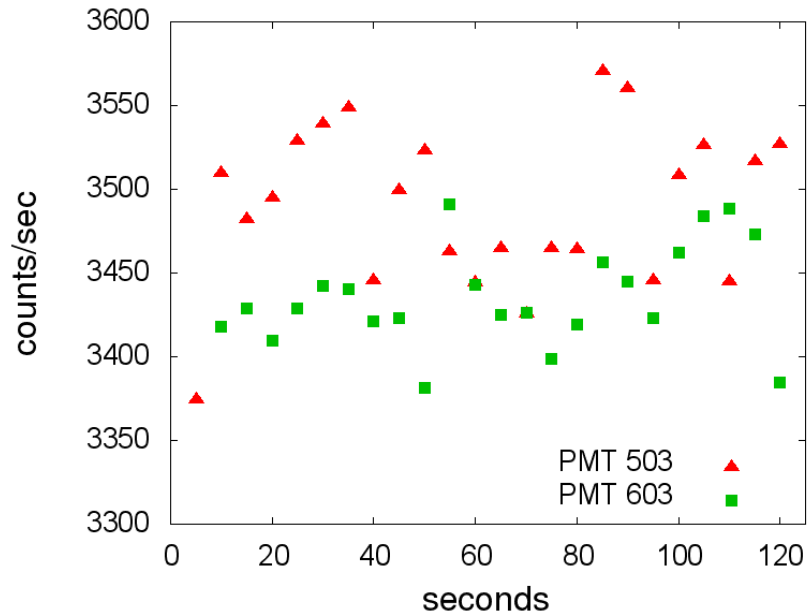
Figure 27: Two measurements of the dark rate behaviour. Both PMT have about the same medium dark rate.

Right after installing the capsules in the darkroom, the PMT needed to "settle down", as they were stored in standard storage racks and ambient light. Typically, the dark rate settles after some minutes, but one PMT showed a very slow decrease of the dark rate and a very high starting rate in the range of MHz. For this PMT, a special measurement was performed, the dark rate was recorded over several hours (fig. 28), again in bins of five seconds. As one can nicely see, the dark rate drops to a reasonable value of $5200 \, \text{cts/s}$ within one day. And even after several days, this rate further decreased to around $3400 \, \text{cts/s}$, which is fully acceptable, so even this "noisy" PMT could be installed into the Cherenkov detector.

Tab. 5 contains the dark rate at a gain of $2 \cdot 10^7$ for each capsule, which was used for the Cherenkov detector, and fig. 29 displays the data as a histogram.
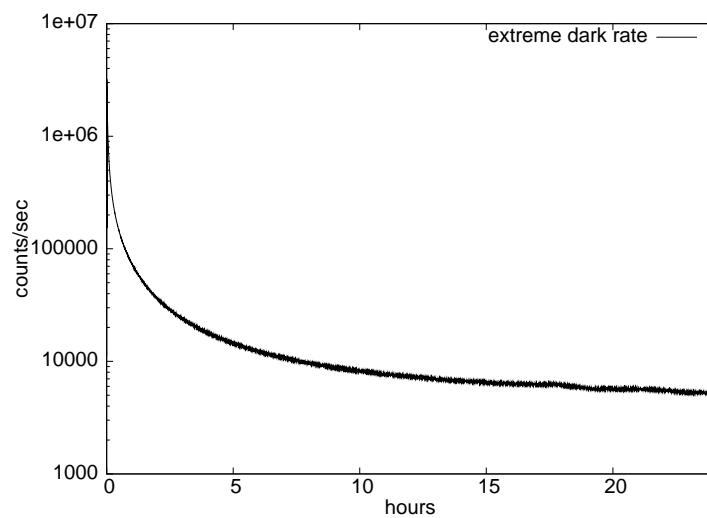
Figure 28: Temporal development of a capsule with a very high dark rate at the beginning of the measurement. After around one day, the capsule shows a dark rate of 5200 cts/s, after several days of lifetime, this value stabilized at around 3400 cts/s.
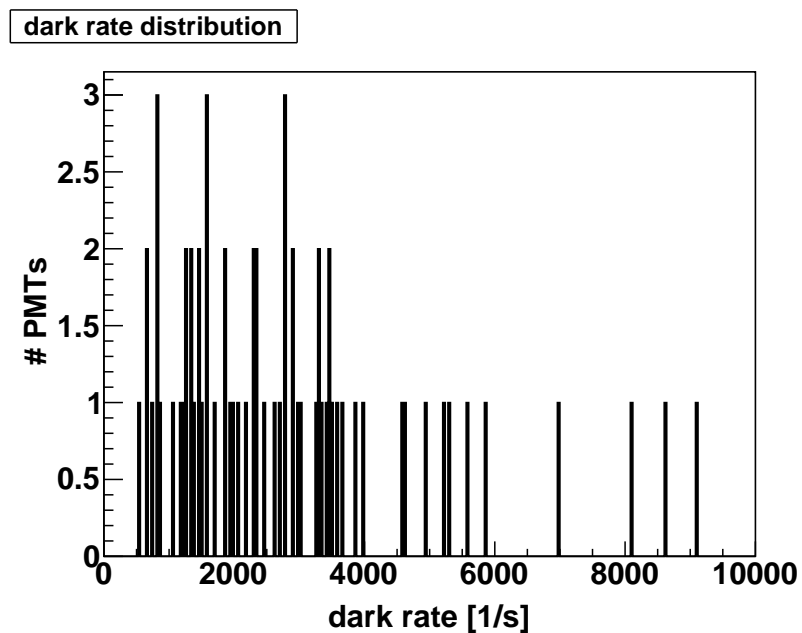
Figure 29: Dark rates of the installed PMTs at a gain of $2 \cdot 10^7$.

Table 5: List of PMTs, voltage@$2 \cdot 10^7$.
[a]: measured with LED;
[b]: measurement was only possible for a gain of $1 \cdot 10^7$

PMT number	Capsule serial	Volts @ $2 \cdot 10^7$	Dark rate	PMT number	Capsule serial	Volts @ $2 \cdot 10^7$	Dark rate
101	30	1435	663.92	501	56	1670	2995.32
102	28	1480	4621.62	502	4	1530	1866.13
103	14	1635	3662.93	503	31	1650	3490.44
104[a]	24	1430	3313.07	504	20	1635	521.983
105[a]	69	1370	2919.88	505	49	1500	1712.59
106	44	1400	1268.9	506	73	1615	831.93
201	27	1740	1053.19	507	23	1750	1378.7
202	51	1425	1204.8	508	68	1625	1572.43
203	48	1670	9084.56	509	12	1700	1568.36
204	17	1560	2067.17	510[a]	8	1640	2297.39
205	76	1500	2718.14	601	61	1520	2790.23
206[a]	45	1700	2455.07	602	77	2080	2792.53
207	52	1540	1322.22	603[a]	34	1630	3415.07
208	22	1610	2352.66	604[a]	29	1630	3459
301	81	1630	2910.81	605	38	2050	3581.9
302	66	1930	3032.85	606	6	1610	2358.4
303	55	1750	3257.52	607	58	1590	4951.06
304[a]	33	1760	2794.46	608[a]	67	1800	1346.24
305[b]	25	1590	2307.37	609[a]	37	1550	3359.7
306	64	1880	1250.04	610	36	1715	3478.8
307	40	1810	1514.74	701[a]	41	1870	3965.62
308	70	1790	1172.12	702	50	1770	1471.97
309	82	1800	8602.6	703	10	1600	3281.16
310	63	1460	1981.83	704	11	1700	5225.48
311	60	1700	2167	705	26	1540	5285.61
312	13	1615	4597.52	706[a]	71	1540	5568.07
401	43	1495	6991.62	707	15	1995	5865.88
402	3	1530	1931.67	708	46	1490	2636.8
403	57	1590	1584.79	709	35	1535	8085.81
404	47	1640	853.4	710	42	1520	3879.97
405	75	2100	652.775				
406	9	1670	1451.14				
407	78	1705	748.542				
408	32	1890	812.975				
409	72	1890	806.933				
410[a]	54	1600	1879.72				

medium dark rate: 2834 cts/s

Chapter 7

Calibration system

To calibrate the PMTs, two complementary calibration systems were developed during this thesis. First, five so called diffuser balls are distributed inside the water tank. These diffuser balls are able to illuminate the water tank with light from a LED outside the tank. Second, each PMT is provided with an optical fiber. Here one LED illuminates all fibers, and, by changing the voltage firing the LED, the PMT can be illuminated with different brightness.
In the following chapter, both systems are described.

7.1 The diffuser balls

The first system uses diffuser balls in the tank to illuminate the PMTs for geometry dependent calibration. The light source itself consists of a high power blue LED for each diffuser ball. The electronic driver for the source is a modified version of a driver first proposed in [Kap85] (fig. 30). The light output of this source is adjustable in the range of $0 - 10^9$ photons per pulse in the range of $3 - 10$ ns. Thus, the response of the PMTs is easily monitored. The light is fed to each diffuser ball with optical fibers. The end of the fiber is fed into the "pre diffuser". This small glass bulb (around 5 to 10 mm in diameter) is filled with a mixture of Lensbond [Sum] and a high concentration of "S32 5 micron glass bubbles" [3Mb]. Due to the high concentration of the S32 glass bubbles, the light emitted at the end of the optical fiber is easily reflected in different directions, leading to a pre-diffusing of the light. The "pre diffuser" is put into the diffuser ball, a glass bulb with a diameter of around 50 mm (fig. 31). The bulb is filled with silicone SilGel 612 A&B [Wac] mixed with S32 glass bubbles. Here, the light is even more distributed, thus, the diffuser ball is illuminating the water tank isotropically. Each diffuser ball is a point like light source.

Four of these diffuser balls are located in the water tank, while one ball is in the volume below the cryostat, the "pillbox". The use of different diffuser balls provides not only geometric dependent responses of the PMTs to recognize shadows, but also a timing information due to the different distance of the PMTs to the diffuser balls.
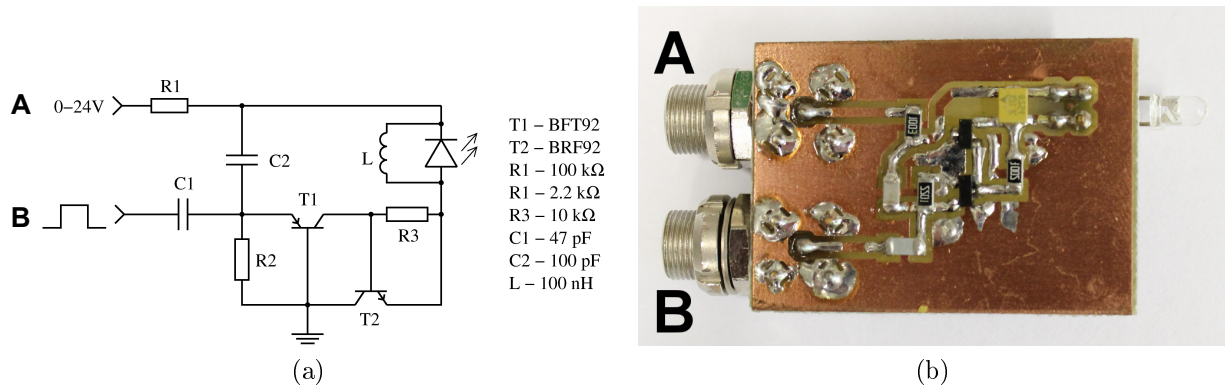
Figure 30: (a) Schematic and (b) picture of the electronics for the LED. On input "A", the voltage is adjusted via a VME DAC module PAS 9817/AO, this defines the brightness of the LED pulse, input "B" is the trigger input which causes a signal.
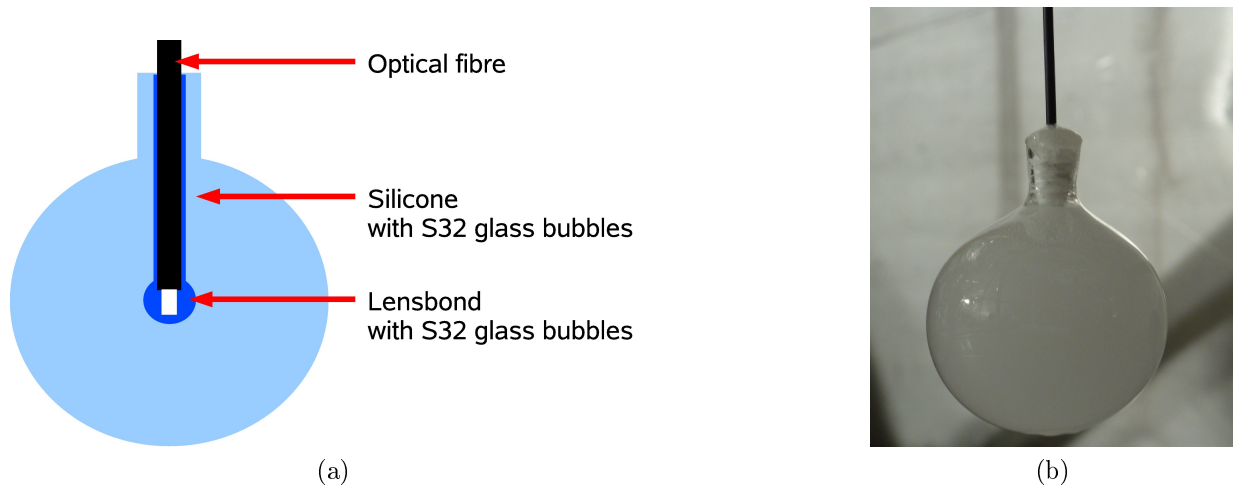
Figure 31: (a) Sketch and (b) picture of a diffuser ball.
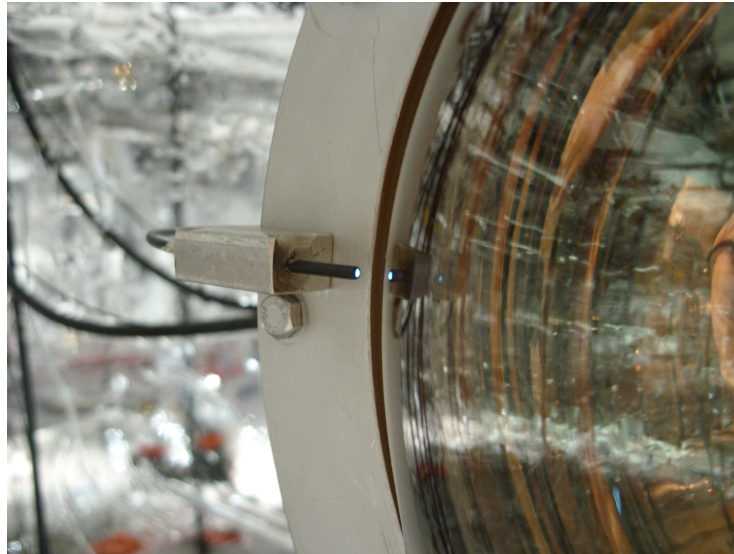
Figure 32: A photomultiplier inside the water tank. One recognizes the photo cathode on the right (golden), the mounted optical fiber, and in the back, the high reflective wavelength shifting foil VM2000.

7.2 Single fibers

The second system uses the same type of light source as the first one. The LED illuminates 80 optical fibers (the "brush"; length: 20 cm, PMMA, core diameter: 1 mm) through a diffusing lens. Each single fiber is connected with a coupling to another, 35 m long fiber, which is fed to one of the PMTs, in fig. 32 one can see the enlightened end of the fiber.

Controlling the LED voltage, one can ensure to illuminate the brush with only some photons, leading to single photon response of the PMTs. Figure 33 shows the different response of one PMT to different supply voltages of the LED. The red curve shows the response of the PMT when the LED is switched off. Driving the LED with a low voltage (here 5.4 V), the single photoelectron peak emerges. With a medium voltage (6.4 V), the double photoelectron peak becomes visible, while with a high voltage (12 V), only one broad peak is visible, as several photoelectrons are emitted. Up to now, this system is not fully installed at LNGS.

7.3 Measurements

First test measurements with the diffuser balls were very promising. It was possible to perform a gain measurement by using all five diffuser balls at once. In fig. 34 the response of the single PMTs is histogrammed. One sees the single p.e. peak. In figure 35, the light in the water tank is shown, together with the trigger multiplicity of the PMTs. Here, one sees, that in each event, around a fourth of all PMTs saw light. As described in Chapter 6, a light source is set right for single p.e. signals, if the detector "sees" light in around 1/10 of the events. In other words, one would expect that the diffuser balls are dim enough, if on average, at each event six to seven
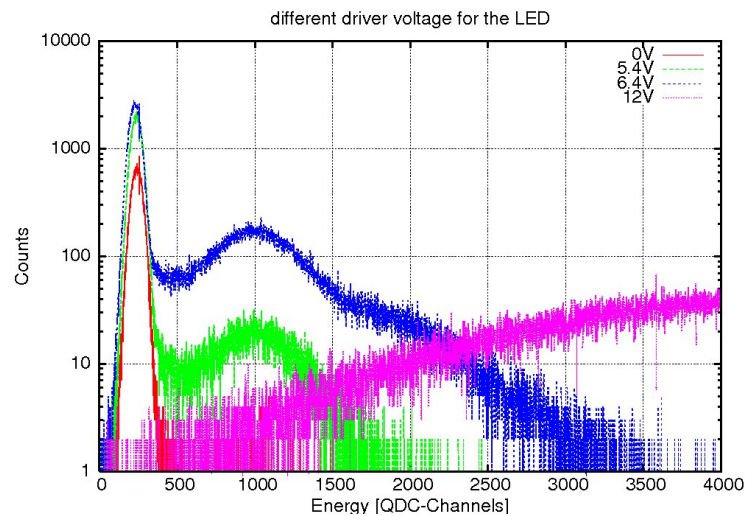
Figure 33: Response of one PMT for different supply voltages of the LED.

PMTs triggered. As shown in fig. 35, around 15 PMTs fired on average, meaning that the diffuser balls were slightly too bright for this measurement, but nevertheless, a gain measurement with the diffuser balls is no problem. One also sees in fig. 36 a nice 1:1 correlation between amount of recorded light and fired PMTs.

Measurements with the single fibers are not performed yet, since the "brush" is not yet installed at LNGS. At the moment, the one end of the fibers are already connected to the PMTs. The fibers are fed through the water tank to the electronics room (the "Cryo-Mu lab") in the second story of the GERDA-building. Here, the other ends of the fibers are packed light tight.
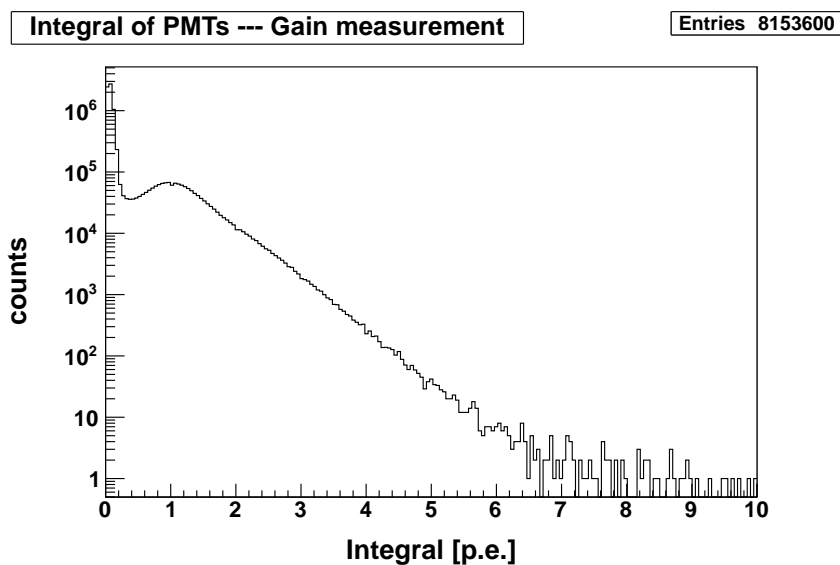
Figure 34: Average response of the single PMTs. One recognizes a peak at 0 p.e.s (the pedestal) and the next peak at 1 p.e.. In addition, as there are still contributions to more than 1 p.e., one sees, that the contribution of multiple-p.e. events is still too high.
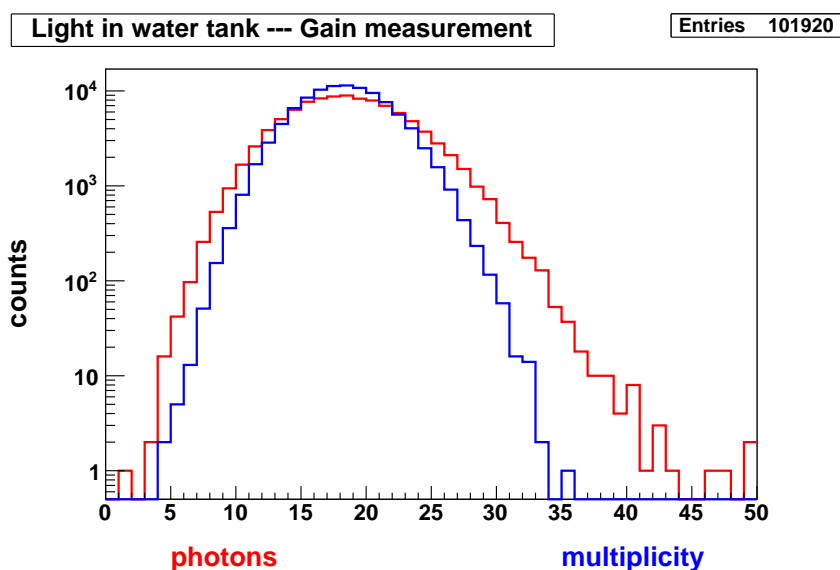
Figure 35: Summed integral response per event. In red, the number of photons detected in the water tank are plotted. Blue is the corresponding histogram for the number of fired PMTs. One sees a coincidence of these two plots, indicating, that each fired PMT detected a single p.e..
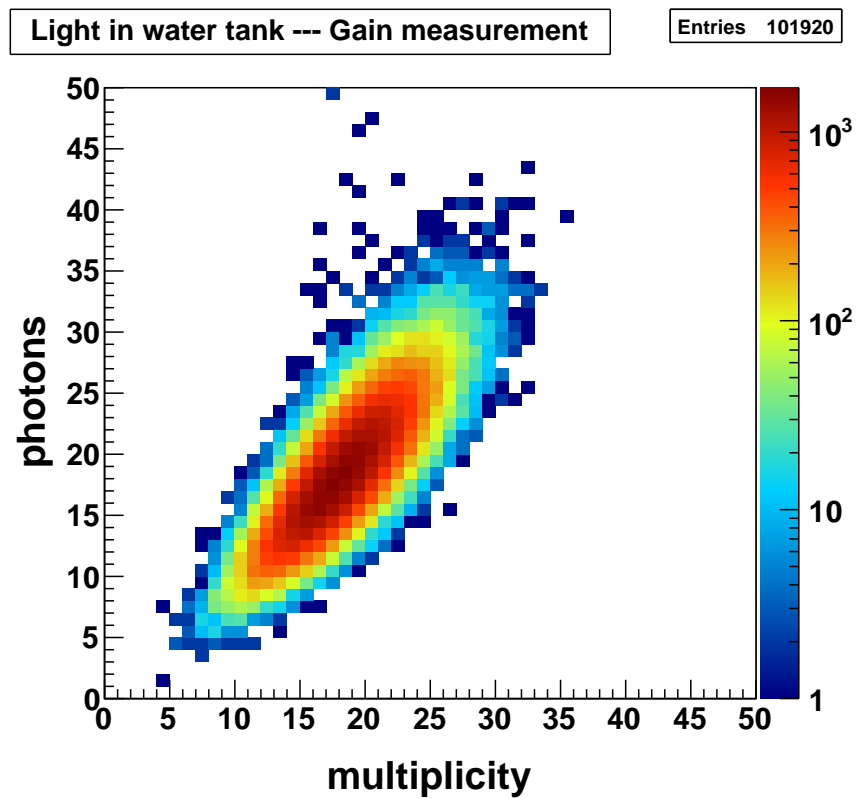
Figure 36: The light in the water tank is plotted against the number of fired PMTs. One sees a huge area around a 1:1 correlation

Chapter 8

Analysis

In this chapter, the very first analysis of data taken with the GERDA muon veto will be presented. A first look on the data and a comparison to expectations from Monte Carlo simulations revealed an enhancement in the low light region. Several coincident events between the muon veto and germanium signals were found. These events, which are certainly muons, are used to analyze the response to muons of the Cherenkov veto. A first analysis of the data from the Cherenkov veto and the preliminary plastic veto is shown as well. To investigate the "low-light-enhancement", several ideas are considered. The data, which are analyzed here, were taken during the period from 1st of December 2010 to 15th of March 2011, in total 83.52 days of experimental lifetime were collected. To trigger, at least 5 FADCs had to produce a trigger signal within 60 ns.

8.1 First light

In a previous thesis, simulations were run to determine the best distribution for the photomultiplier within the water tank [Kna09]. These simulations showed that even without the highly reflecting foil on the walls, most of the muons traversing the water tank produce enough light to be detected. As the highly reflecting foil is covering all steel-surfaces, and as it is also shifting UV light into visible range, the chance of an optical photon to reach a PMT is increased. Thus, a typical muon should be revealed by a high multiplicity of fired PMTs. Fig. 37 shows the simulated PMT multiplicity spectrum in the water tank due to traversing muons. In the simulations, the "pillbox" was assumed to be a totally enclosed volume, thus, a spike is seen at 6 PMTs (only the pillbox fired), and another peak at 60 PMTs (only the entire outer part of the water tank fired). As the pillbox has two windows to the main tank, the two peaks are not seen in the first data (fig. 38). But there is also a steep rise to high multiplicity like in the simulations. In addition, a "bump" at low multiplicities up to 20 photomultiplier arises which is too large to be explained by the pillbox spike in the simulation. Possible reasons of this bump will be discussed in section 8.7. These could be fast electrons causing Cherenkov effect or ambient neutrons or gamma rays (for example from the stainless steel wall of the water tank) causing scintillation in the reflecting foil.

The overall trigger rate is around $4 \cdot 10^{-2}$ cts/s which is slightly larger than the expected muon rate of $3 \cdot 10^{-2}$ cts/s given by the simulations [Kna09]. All together, the "first light" shows, that the Cherenkov veto is working quite well, but to fully understand the data, further investigation is needed.
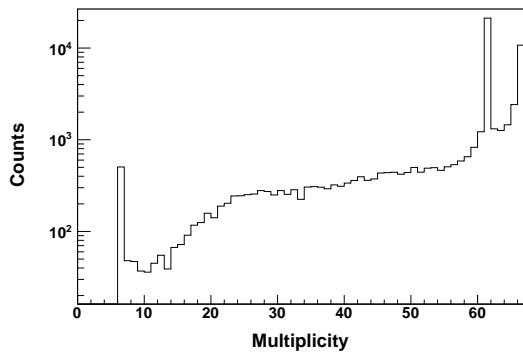
Figure 37: Simulated multiplicity of the Cherenkov PMTs. Only "dangerous muons", i.e. muons with energy deposition in the germanium array are recorded. The simulated run time was 14 years [Fre11].
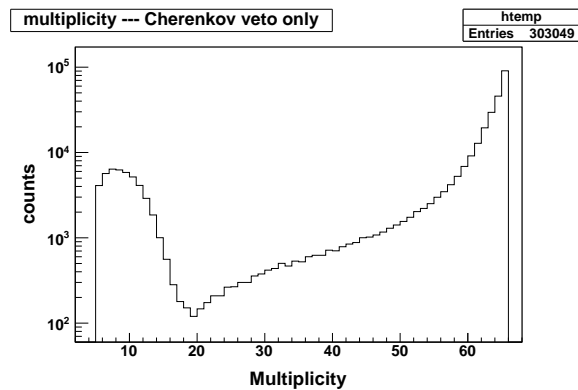
Figure 38: Measured multiplicity of the Cherenkov PMTs. The data were taken for 83.52 days. These are all events registered in the water tank, no cut on energy deposition in the germanium detectors was performed.

The following section describes the signals of the PMT as they are recorded. It is followed by a look on the integral light measured in the whole water tank and in the pillbox. The analysis of the integral light is then used to group the events in four classes. Then, different coincidence tests together with calculations are presented, which try to explain the origin of the "low multiplicity bump".

8.2 Pulses

In fig. 39, a variety of pulses (= PMT signals as function of time) recorded during one event are plotted. The upper left plot shows for example a typical single photoelectron signal. One can see the sharp signal with a rise time of 20 ns. Measurements taken with an oscilloscope revealed an intrinsic rise time of 4 to 5 ns for single photons. The difference is a tribute to the sampling rate of the FADC (100 MHz), as an anti-aliasing filter is implemented. Around 350 ns after the main pulse, a relatively prominent electronic reflection is visible, which is caused by the reflections between splitter box and PMT. Since the height of this electronic reflection is only 1/10 of the single p.e. pulse, it is no problem for the trigger system.

The upper right picture on fig. 39 shows a pulse, which reached the maximal pulse height. The overall pulse shape is comparable to the single photon pulse on the left side. Due to the different scale, the baseline seems much less noisy in this case. One clearly sees the electronic reflections 350 ns, 700 ns and 1050 ns after the main pulse. In addition, several small spikes are visible after the main pulse, which are most likely due to optical reflections on the water tank walls. In the following sections, the integral of the pulse was taken as a measure of the light in the tank.

The effect of optical reflections is nicely seen in the two lower plots of fig. 39. For example, on the lower right, one can recognize several spikes, each of them some tens of nanoseconds after the preceding spike, which means, that the PMT under investigation "saw" light reaching it at
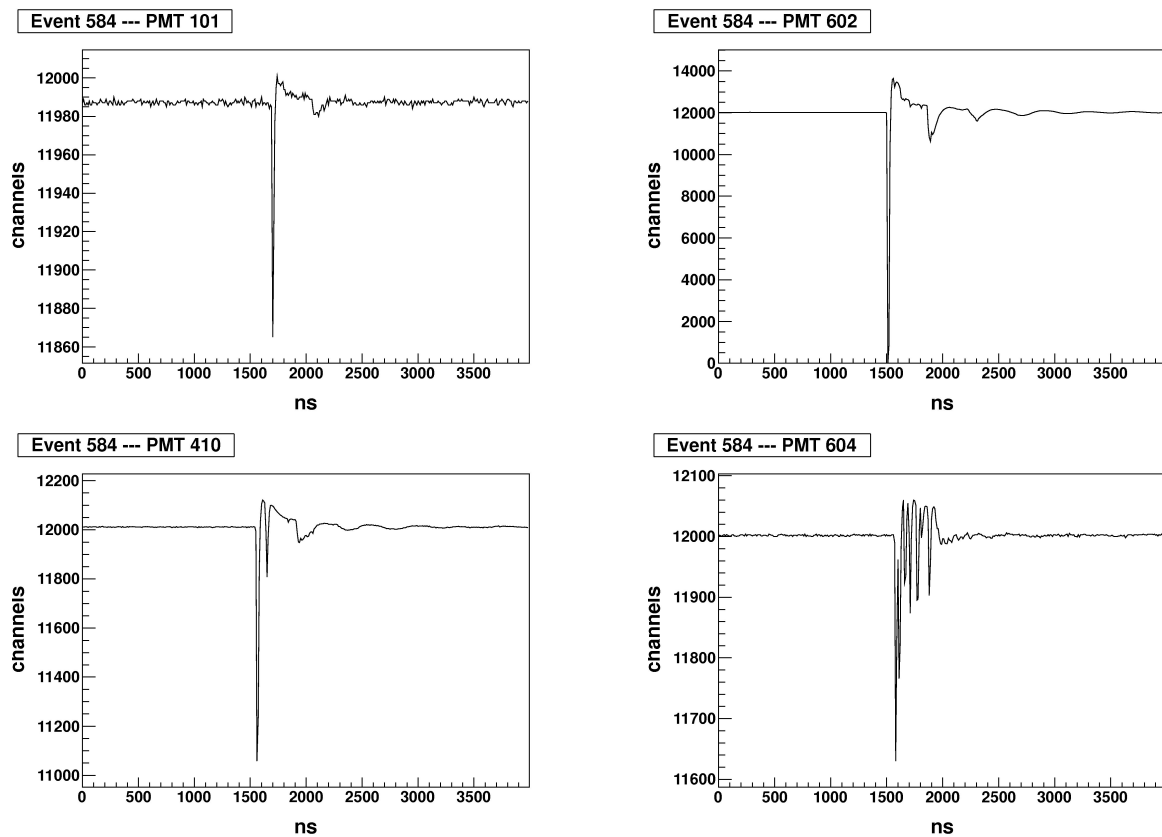
Figure 39: Different pulses: upper left: a single photon event is shown; upper right: all photons were registered within one sampling step of the FADC (10 ns); lower left: one high event (i.e. ≈ 10 photons) with a second hit of ≈ 3 photons around 90 ns later; lower right: several photons hitting the PMT at different times, i.e. multiple optical reflections. All traces were recorded during one event, which is shown in figure 63.

different times. A time difference of 30 ns (3 clock ticks) for example corresponds to a traveling distance of light in water of around 6.7 m. As the radii of water tank and cryostat are 5 and 2 m, respectively, the minimum length between the two walls is 3 m. Thus, if there is for example one photon reaching the PMT directly, while another photon, emitted at the same time and position reaches the PMT via a reflection on the cryostat wall, this could easily explain a measured travel time difference of around 30 ns. Of course, reflections also occur on the bottom surface, and even multiple reflections can occur.

As it is needed in the further analysis: the "multiplicity" defines the number of fired PMTs. Each PMT, which fired within 600 ns around the trigger signal is marked as "fired". This long time period is needed since due to possible multiple reflections of a photon, it might take some time after the muon passed the water tank, until a PMT is hit.

To analyze the data further, a classification of the events will be presented in the next section, followed by an analysis of coincident events between the Cherenkov veto and either the germanium detectors or the preliminary plastic veto. The time structure of the events is the subject of the third section, afterwards, a calibration from amount of light to track length will be done. Section 8.7 will focus on the "low multiplicity bump" and will try to figure out, what physical reason might cause it. Finally, the final muon cut will be presented, followed by a calculation of the muon detection efficiency.

8.3   Classes of events

Figures 40, 41 and 42 show the light in the whole water tank, the outer part without the pillbox and in the pillbox respectively versus the multiplicity in the whole water tank. The plot of the total light (fig. 40) shows an indication of a band in the region of several hundreds p.e. and a multiplicity of more than 15 PMTs. This band vanishes in the outer part of the water tank (see fig. 41) but is still present in the pillbox as seen in fig. 42, indicated as class 1. As it is a relatively large amount of light, this leads to the conclusion, that these events are most probably caused by muons traversing the pillbox.

As one can see in fig. 42, one can divide the data in four different regions, defining four classes of events:

- **Class 1 (μ in pillbox):** Events, which are producing a lot of light (≥ 80 p.e.) in the pillbox. The multiplicity of PMTs in the whole water tank spans from around 15 PMTs to all 65 PMTs. These events are selected by a cut ≥ 80 p.e in the pillbox. These are certainly muons traversing the pillbox with a relatively long track. The multiplicity then depends on the trajectory of the muon in the rest of the water tank and the light leaking out of the pillbox.

- **Class 2 (μ in water tank):** A moderate number of photoelectrons are produced inside the pillbox, reaching form single p.e. to some tens of p.e.. The total PMT multiplicity of these events span from 20 PMTs to the full 65 PMTs. Here, one has to apply a cut > 20 PMT in the whole water tank AND < 80 p.e. in the pillbox. Most probably, these are muon events (or more precisely events with a lot of light) in the rest of the water tank, where light is shining through the man holes into the pillbox. And/or such events with a short path in the pillbox.
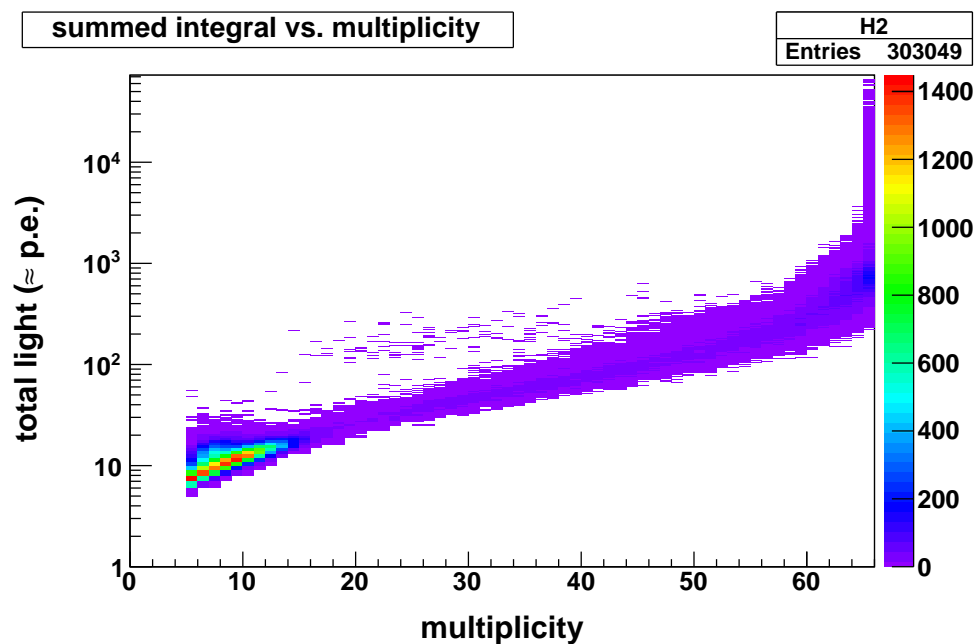
Figure 40: light in the whole water tank versus multiplicity. the total light in the water tank spans from some p.e. up to several ten thousands of p.e., while the "low multiplicity bump" is equivalent to a "low light" bump (i.e. the "hot spot" on the lower left).
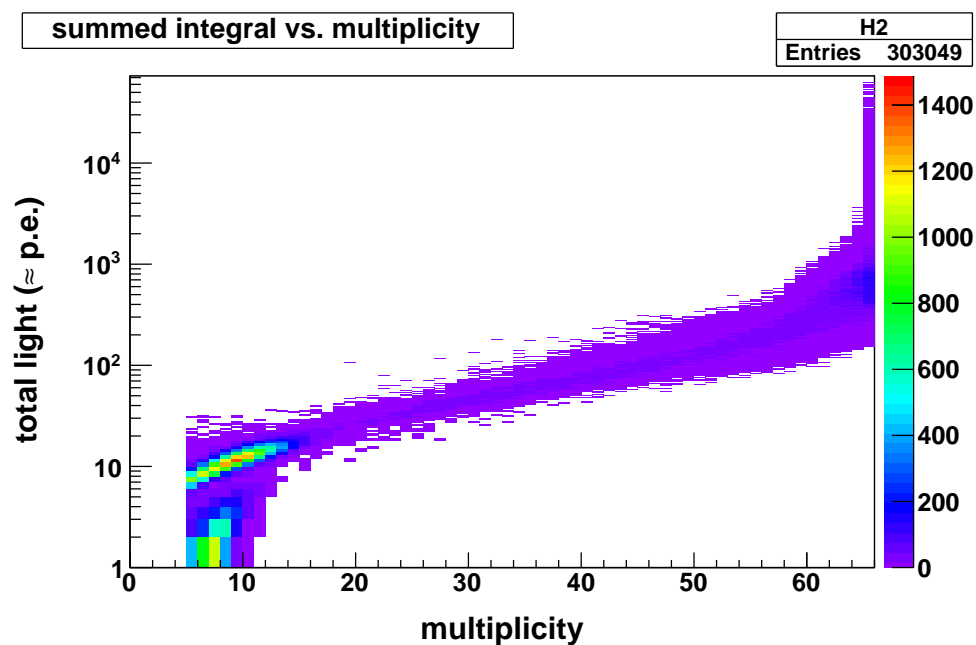

Figure 41: light in the outer water tank versus multiplicity. Here, "outer water tank" means the water tank without the pillbox.
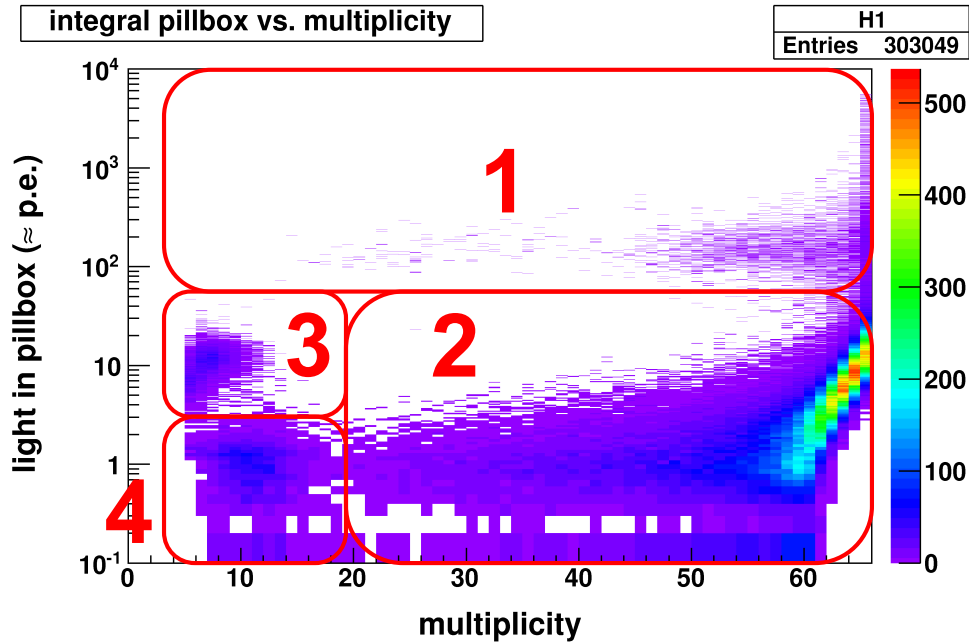
Figure 42: light in the pillbox versus multiplicity. Only events with at least one fired pillbox-PMT are recorded. The four different classes described in the text are shown.

- **Class 3 (light, but no μ in the pillbox):** Those events are producing not as much light as class 1 events, but they are all located in the low-multiplicity region, so there seems to be a relation between low light and low multiplicity. Due to their location on low-multiplicity and low-light, this could be muons, only traveling a short distance in the pillbox AND a short distance in the rest of the water tank, or other physical reactions causes these events. The cut, which has to be applied: ≤ 20 PMT AND > 3 p.e. AND < 80 p.e..

- **Class 4 (light, but no μ in water tank):** Only few (up to three) p.e. are produced in the pillbox, and the total PMT multiplicity spans up to 20 PMTs. Those events might either be accidental noise in one Pillbox-PMT coincident with some low-light event in the rest of the water tank, or just being an addition to class 2, since the gap between these two classes is not so clear, however, there is an increase in rate towards low multiplicity. To cut on these events, this are the cut conditions: ≤ 20 PMT AND ≤ 3 p.e.in the pillbox.

As classes 1 and 2 are both either high multiplicity or a high amount of light in the pillbox, these are expected to be muons. The classes 3 and 4 are both in the multiplicity range of the previously mentioned "bump", where it is not clear, if muons are responsible for the light or if another physics process is the origin of this bump. But nevertheless, there might be as well muons which are responsible for some entries in these classes.

With these four classes, one can plot the same figure as figure 40, but now color coded for the four different classes. Figure 43 is the respective plot. Here, one can see, classes 1 and 2 are populating the same region for high multiplicities, let's say > 40 PMTs. This occurs, when a muon is traversing both pillbox and the outer part of the Cherenkov detector with reasonable

track lengths (in the order of meters). And, in addition, in this plot, classes 3 and 4 are both populating the low multiplicity/low light region. By the light in the whole water tank, classes 3 and 4 cannot be distinguished, thus they differ only by their light in the pillbox.
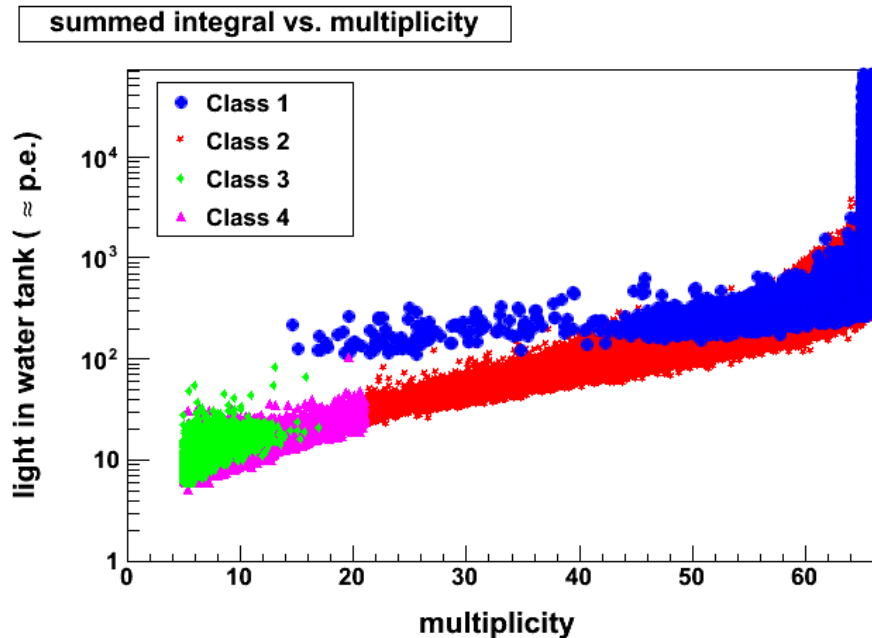

Figure 43: light in the water tank versus multiplicity. Here, the classes taken from fig. 42 are color coded.

Table 6 on page 74 shows the rates for the classes. As one can clearly see, the main contribution comes from events of class 2. To verify the classification of the Cherenkov veto events that muons are identified properly, two coincidence measurements were performed. The first one is looking for coincidence between Cherenkov and plastic veto, the second searches for coincidences between Germanium detectors and Cherenkov veto.

8.4   Coincidences

For the whole data set, the preliminary plastic veto was available, consisting of seven plastic panels, so, the first subsection will analyze the coincident events between the preliminary plastic veto and the Cherenkov veto. In addition, the Germanium data were available from 13th of February to 15th of March 2011, a life time of 30.76 days. The combination of these data gave the possibility to search for coincidences between Cherenkov veto and Germanium detectors, this will be shown in the second subsection. These coincidences can only be caused by muons. Thus, to study which signal structure is caused by muons in the veto, the coincidences are used. In June/July 2011, the full plastic veto (consisting of 36 plastic panels) was installed.

8.4.1   Coincidence between Cherenkov and plastic veto

In November 2010, a preliminary version of the plastic scintillator veto was installed on top of the roof of GERDA. It consisted of seven plastic panels ($2000\,\mathrm{mm}\times500\,\mathrm{mm}\times30\,\mathrm{mm}$), three packs of two and one single panel. Each panel is equipped with a 1" PMT, which detects the light produced in the panel (Section 4.1.1). The electrical signal from these PMTs was fed into the μ-DAQ as a separate set of signals ("pospm"). A muon traveling through the plastic veto and the Cherenkov veto should cause a signal in both parts of the muon veto. Due to a lack of flexibility in the DAQ at this time, it was only possible to trigger either on the plastic veto or on the Cherenkov veto. Several tests were performed with different trigger values and trigger options. As there was a need for an appropriate muon veto signal for the Ge-DAQ, it was decided to do the tests with a trigger on the Cherenkov veto only, the plastic veto was read out passively. Thus, the Cherenkov veto was used as an external trigger for the plastic veto[1]. A muon passing the plastic veto most probably passes through a panel of the top layer and a panel of the bottom layer, so one expects a signal in both layers. In figure 44, a 2D plot is shown, with the signal in the upper layer on the y-axis and the signal in the lower layer on the x-axis. One can clearly see signals in both layers, and two groups of signals along the axes, meaning almost no signal in one of the layers. In between, there is a gap. This gap can be used to cut on "real" coincidences. An easy cut would be to ask for a sum of top and bottom higher than a threshold. This would lead to a diagonal line in the plot. Another cut would ask for a threshold on each layer, which would cause a horizontal and a vertical line. Or one can apply a product cut, meaning that the product (x-const) · (y-const) has to be beyond a specified value. All three different cuts are shown in figure 44, one clearly sees the advantage of the product cut. The sum-cut and the individual cut can cut away the area at low values, but both do not cut events, which are mainly due to light production in one of the layers, meaning low x-values and high y-values or vice versa. Only the product cut can account for these events.

In figure 45, the pulse height histogram of the lower layer (i.e. the projection to the x-axis of fig. 44) is shown. Without applying a cut, one gets a huge amount of low light events. This may be electrons or γ's coming from the surrounding rock. If one applies the product cut, the muon peak survives the cut almost without a change. This cut can now be applied to select muons which are traversing plastic veto and Cherenkov veto while histogramming the multiplicity of the Cherenkov PMTs. One example is shown in Appendix I.2 in figure 72 on page 105. The low multiplicity bump vanishes, while the part above ~ 20 photomultiplier shows the same behavior as the overall histogram (fig. 46).

Classifying the coincident events in the four different classes, Tab. 6 (page 74) shows how this subset of muons is distributed over the classes. Selecting classes 1 and 2 (i.e. with $\geq 80\,\mathrm{p.e.}$ in the pillbox or > 20 fired PMT in the whole water tank) within the coincident events would loose only 30 out of 4536 events, which means $0.66\,\%$ of this subset of muons. Thus, one can conclude, that most of the muons are populating the classes 1 or 2.

---

[1]Since end of July 2011, the plastic veto is fully equipped and the DAQ is improved. Now, it is possible to have a combined trigger: either a signal in the Cherenkov veto or in the scintillator veto will cause a trigger signal [Fre11]. But for this work, data were recorded, when only the Cherenkov veto triggered.
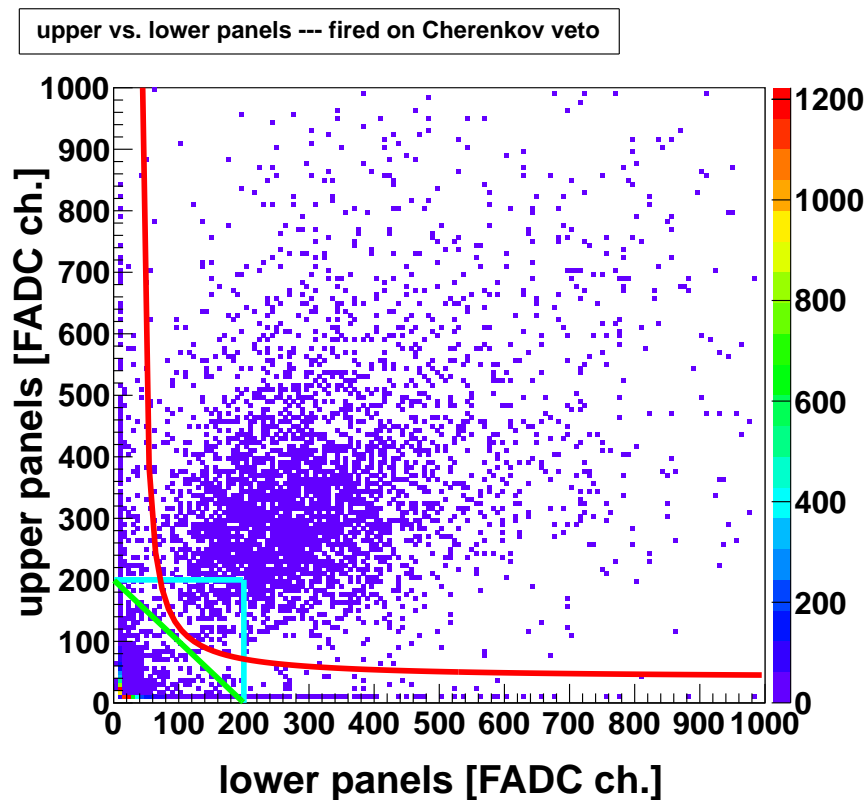
Figure 44: upper vs. lower panel with cuts. The sum of all three panels within one layer is plotted. A sum cut was performed to get rid of a peak at (10,10), which occurs for "no light in both panel layers". Cyan: a fixed cut for each layer individually is set; Green: a sum cut is set; Red: a product cut is set. Both the cyan and the green cut are cutting away the very low events (lower left corner), but the events with only a "high" event in one layer survive the cut, while the red cut also cut away these events.
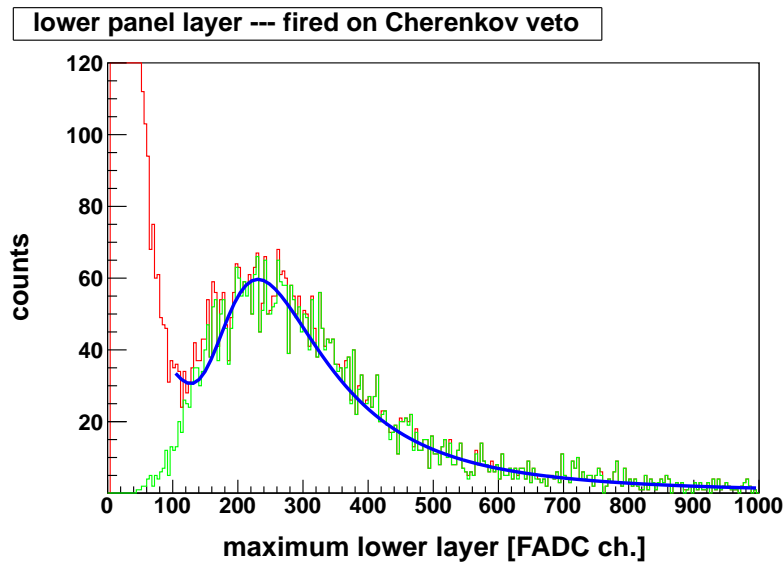
Figure 45: pulse height of the lower panels. In red: all events, in green: events after the product cut. The blue curve is a fit on the green histogram, an exponential function for the remaining background and a Landau distribution for the muons assumed. A nice muon peak shows up, while some events with high entry were cut out, due to a "null event" at the other layer. The maximum of the Landau distribution corresponds to an energy of 6 MeV. The muon rate is $2.26 \, \mu/\text{h}$, which slightly smaller than the expected rate of $3.3 \, \mu/\text{h}$ for the area of $3 \, m^2$.
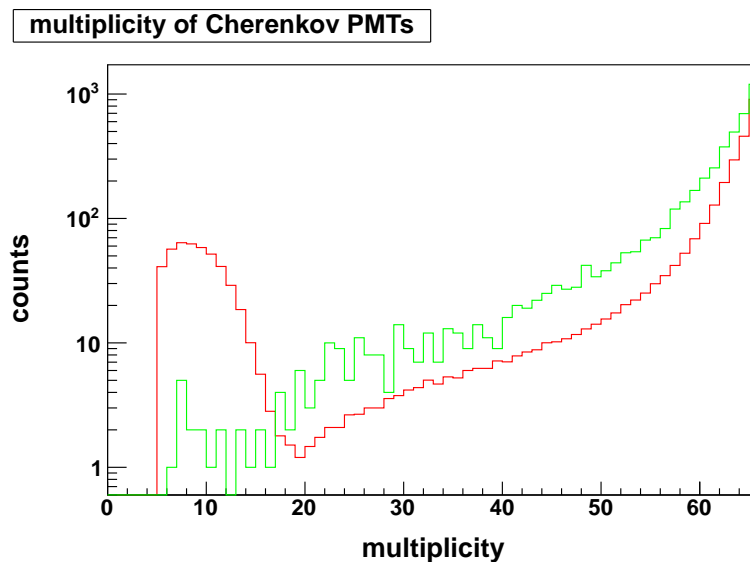
Figure 46: multiplicity of the Cherenkov photomultiplier, with cut on events hitting the panels. red: all events, scaled; green: product cut on panels.

8.4.2 Coincidence between Cherenkov veto and Germanium detectors

To search for coincidences between the Cherenkov veto and the Germanium detectors, a data set from 13th of February 2011 to 15th of March 2011 (30.76 days) was taken from the Ge-DAQ. These data were taken with three Germanium detectors (GTF45, GTF32, GTF112) with a natural abundance of Ge isotopes (i.e. $\sim 8\,\%$ ^{76}Ge) to investigate the background and to test the whole setup. The total mass was 7.622 kg. This leads to an exposure of 0.642 (kg·y). As the Ge-DAQ is using the same hardware as the μ-DAQ, the data structure is the same, nevertheless, the conversion tool, which was developed during this thesis had to be modified to convert the germanium data into the same ROOT structure as the μ-DAQ data. One input channel of the Ge-DAQ is reading out the muon veto trigger signal, thus, in the Germanium data, a rectangular pulse shows up in that channel, if a muon trigger signal was present at the same time as a Germanium signal. This channel is read out passively, a muon trigger does not trigger the Germanium readout.

To find the muon coincident events on the μ-DAQ data, the first step was to search for this rectangular pulse in the Ge data. In figure 47, a typical muon-induced germanium event is shown. The trigger signal of the muon veto is shown in red, the other three lines correspond to the three germanium diodes. As one can see, the muon trigger signal is delayed by 21 μs, this delay is due to the different Pre- and Posttrigger settings in the two DAQ systems, but it is constant for all the runs.

As the DAQ systems record the UNIX time stamp for each event, this information can be used to search for the corresponding event on the μ-DAQ data. One would expect a time offset close to zero, due to some differences in the cable lengths between muon veto detectors and germanium detectors. But in fact, the time offset was around -17.3 seconds, as seen in figure 48. This was due to a wrong setup of the NTP client on the μ-DAQ, thus, the μ-DAQ delivered the wrong time stamp. For later runs, this problem was fixed, leading to a time difference in the range of some μs. As the DAQ also can handle a GPS time signal, a GPS clock was installed in July 2011 for synchronization. This should lead to a time accuracy of around 20 ns [Kih11].

Such coincident events between μ-DAQ and Ge-DAQ are another probe for the muon veto trigger efficiency. With trigger rates of $\approx 1 \cdot 10^{-2}$ cts/s and $\approx 4 \cdot 10^{-2}$ cts/s for the Ge-DAQ and the μ-DAQ respectively, and a recording time duration of 160 μs (Ge-DAQ) and 4 μs (μ-DAQ), random coincidences are very rare (2 events in one year of data taking). In the 30.76 days of data taking, around 100 events were found, so one can conclude that the coincidences found are true coincidences. As one can see in figure 49, where the multiplicity of PMTs of these events is histogrammed, there are no events in the bump region. The distribution follows more or less the high multiplicity region (without the bump). This leads to the conclusion, that muons with energy deposition in the germanium detectors are not the origin of the low multiplicity bump.

Again, also on the coincident events, one can apply the cuts for the four different classes. On page 74, Tab. 6 shows that the events of this Ge coincident subset are distributed over the classes 1 and 2.

All events are either class 1 or class 2 events. All 107 events lead to a muon induced germanium rate of $4.03 \cdot 10^{-5}$ cts/s. Together with the exposure of 0.642 (kg y), one can convert the muon induced germanium event rate to 68.69 cts/(kg y). This is in good agreement with the simulations presented by Markus Knapp in his thesis [Kna09]. There, two simulation campaigns were performed. Campaign I simulated 15 kg Germanium without detailed setup of the surrounding
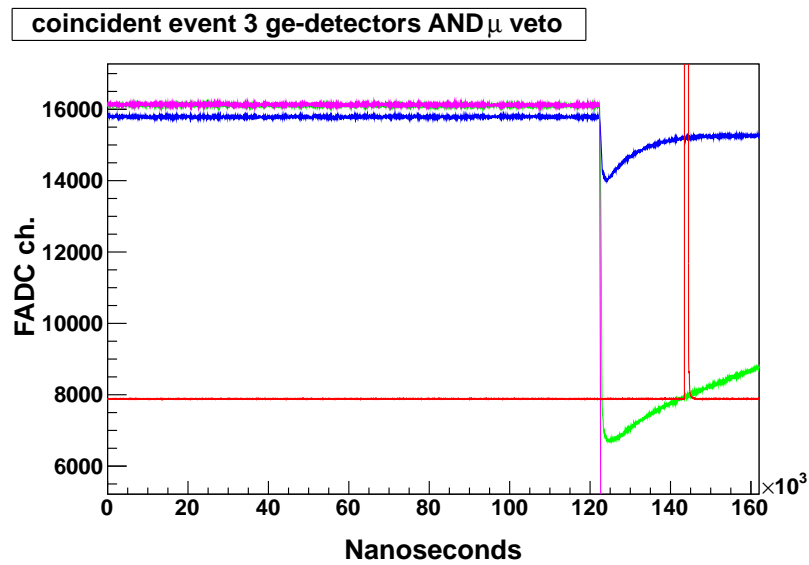
Figure 47: A muon-induced germanium event. In red, the muon trigger is seen, the other lines correspond to one Ge diode each. All three diodes fired, this event would have been cut away by the anti coincidence cut.
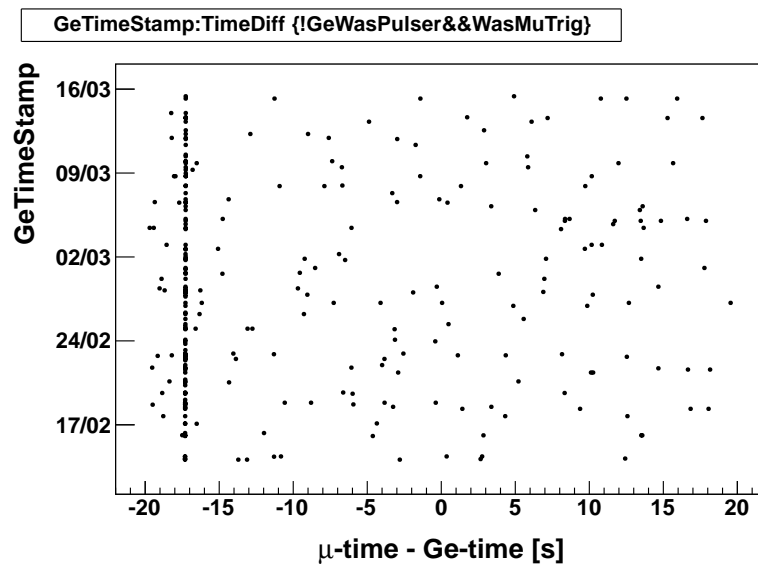

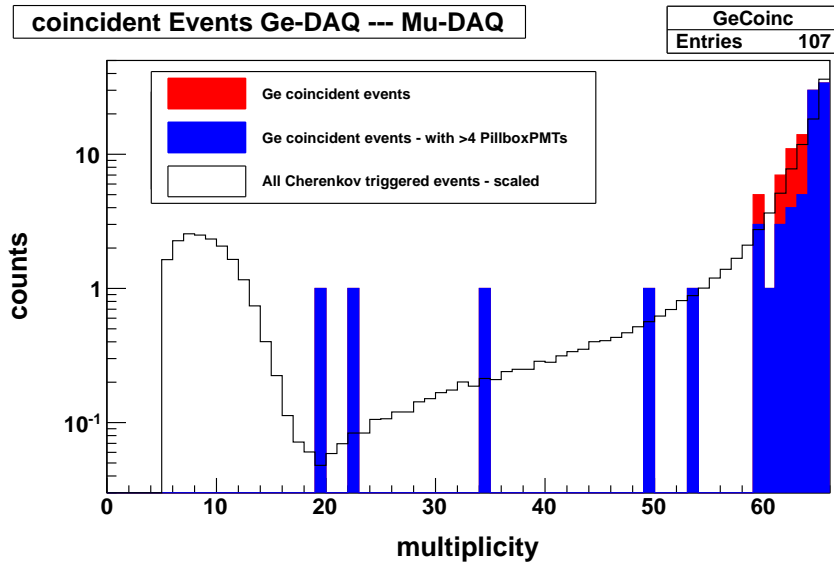Figure 48: Time difference between Ge-DAQ and μ-DAQ.

Figure 49: multiplicity plot for Ge-coincident events. Blue and red: coincident events; black: overall muon-DAQ signals, scaled.

material, thus only the detectors were hung into the liquid Argon. This gave a number of 935 muon induced events per year, which results in a rate of 62.33 cts/(kg y). In Campaign II, a more detailed setup was used, for example, the holders of the detectors were now implemented more realistically. There, 40 kg of Germanium were simulated, leading to 4078 muon induced events per year, which results in 101.95 cts/(kg y). The difference in the two simulations is mainly due to the larger amount of material close to the detectors, since this leads to a larger number of secondary particles. These secondaries could induce an event in the germanium detectors even if the muon itself passed the detectors without energy deposition, leading to an increasing number of muon induced events. The measured rate of muon induced events fits perfectly to the simulated rates. It is close to the results from Campaign I, this is in good agreement to the fact, that also the detector masses are in the same range (7.6 kg in the measurement, 15 kg in the simulation).

8.4.3   Conclusions from the coincidence analysis

Table 6 lists the distribution of the coincident events over classes 1 to 4. Both coincidence subsets are mostly class 1 or 2 events, while the classes 3 and 4 are strongly suppressed. Of course, both coincidences are only subsets. The coincidence between Cherenkov veto and plastic veto only selects muons which are mainly going from top to bottom, while the coincidence between Cherenkov veto and germanium detectors only select muons which have deposited energy in the germanium detectors. But nevertheless, the combination of both results show, that classes 1 and 2 are mainly muons.

Combining the results of both coincidence analysis, one can conclude, that one looses 0.66 % of all detected muons, if one uses classes 1 and 2 as a muon selection cut.

For the entire veto data set (without taking coincidences into account), one looses 14.75 % of the events when cutting on classes 1 and 2. This seems to be a big discrepancy, but one has to keep

Table 6: Summary of class cuts.

class		all	1	2	3	4
cut on multiplicity		—	—	> 20	≤ 20	≤ 20
cut on pillbox light		—	$\geq 80\,\text{p.e.}$	$< 80\,\text{p.e.}$	$> 3\,\text{p.e. AND}$ $< 80\,\text{p.e.}$	$\leq 3\,\text{p.e.}$
no coincidence	events	303049	31050	227304	9734	34961
	contribution [%]	100	10.25	75.01	3.21	11.54
	rate $[10^{-2}\,\text{cts/s}]$	4.2	0.43	3.1	0.13	0.48
with plastic veto	events	4536	344	4162	1	29
	contribution [%]	100	7.58	91.75	0.02	0.64
	rate $[10^{-4}\,\text{cts/s}]$	6.29	0.48	5.77	0.001	0.04
with germanium	events	107	22	85	0	0
	contribution [%]	100	20.56	79.44	0	0
	rate $[10^{-5}\,\text{cts/s}]$	4.03	0.83	3.20	0	0

in mind, that the data revealed a huge bump at low light, which was not seen in simulations. The events in this bump are all in classes 3 and 4.

258354 events in the 83.52 day data survive the cut. If one assumes that those are all muons, taking the efficiency derived with the coincidences, we end up with 259966 muons detected in the Cherenkov veto in this period, or a muon rate of $3.6 \cdot 10^{-2}\,\text{cts/s}$. In [Pan07], a muon rate of $4.2 \cdot 10^{-2}\,\text{cts/s}$ is given.

8.5   Time structure

Histogramming the firing time of each PMT (meaning the first time, a PMT saw light during one event) might reveal additional information for the classification or identification of the different types of events. In figure 50, several histograms are shown. In these figures, the trigger occurs at clock tick 153, indicated by a red dotted line. The DAQ system creates a trigger, when at least five FADCs are firing within 60 ns. The 60 ns are from clock tick 144 to clock tick 150. All histograms are normalized to a "standard event" of this subset of events. In the upper left, the histogram for all events is shown. Most of the PMTs are firing between 150 and 160 clock ticks. The upper right plot shows the histograms of class 1 and class 2 events. The shape of both histograms is quite the same, especially in the "after trigger" part, both are practically the same. The lower right plot are the histograms for classes 3 and 4. Here, a steep step between 144 and 149 clock ticks arises. This step is the coincidence region, here, at least five PMTs on five different FADCs have to fire to cause a trigger. As both class 3 and 4 are events with a low multiplicity, it is obvious that the coincidence region is prominent in these classes. Also here, the shape of both histograms is comparable, but, both histograms differ from the overall histogram. The difference in the shape of classes 3 and 4 compared to classes 1 and 2 indicate that one could think about an

additional cut for a comparison between the signal behaviour in a "pretrigger" region and a region around the trigger time. A quotient of the number of fired PMTs in the pretrigger region to the number of fired PMTs in the trigger region is higher for classes 3 and 4 (around $10^{-3}/1$) than the quotient for the classes 1 and 2 (around $10^{-3}/10$). Nevertheless, one has to keep in mind, that for an event by event discrimination, this quotient could be 0 for a class 1 event, if no PMT fired before the trigger region, which is the same as for the case, if only just the required 5 PMTs fired in the trigger region.

The plot in the lower right of figure 50 shows the histogram of the events which were coincident with the plastic veto. Although this histogram is only for comparison, one nicely sees, that its shape is quite the same as the shapes of the class 1 and 2 histograms.
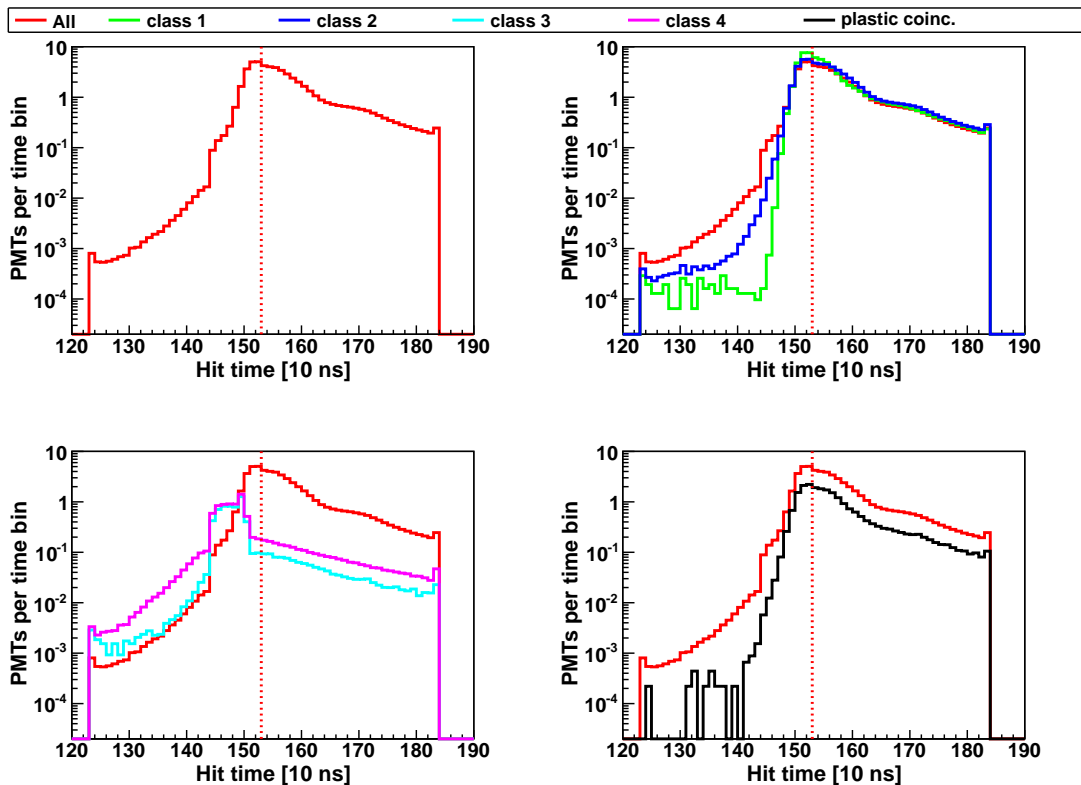
Figure 50: The time structure for the different classes of events are plotted. In red is the time structure of all events, while the other colors indicate sub-classes of events. In black is the curve for the events coincident with the plastic veto. As one can see on the upper right plot, the classes show a similar behavior. Also classes 3 and 4 are similar to each other.

8.5.1 Timing on each event

To have a look on the timing of each event, a small program producing a 2D plot with dots representing the positions of all PMTs was written. The color of the dots indicates the firing

time, while the size represents the integral light this specific PMT has seen. For the plastic pixels, the only color indication is the number of firing layers. The program is described in detail in Appendix A. Fig. 51 shows an event, where 63 PMTs have fired, it also contains the already fully equipped 36 pixels of the plastic veto. PMT 710 in the upper left corner triggered first and also saw the most light. The light then propagates towards the $3/2\,\pi$ and $1/2\,\pi$ region, which can be seen in the "wall" and in the "bottom" plot. The PMTs 104, 205, 308 and 406 registered the light around 300 ns after the first PMT. In addition, two panel pixels also registered a throughgoing muon.

8.5.2   Quotient maximum/integral

In section 8.3, the events were classified through some cuts on either the light in the pillbox or the number of fired PMTs. Figure 52 shows the quotient of the summed maximum per event and the summed integral per event versus the summed integral. Class 1 is well separated from class 3 and 4, while class 2 is overlapping with class 1 and 4. The quotient is at around 1 for a small amount of light. Here, each fired PMT saw the light at once, no reflections occur. These events, one can call "fast events". For events with more light, the quotient drops down since optical reflections get more and more possible and hence, it happens that one PMT sees light at different times. Due to the optical reflections, the collection of the light needs more time, thus these events can be called "slow events". For example the trace shown in the lower right plot in figure 39 shows several pulses, taken alone, this signal would lead to a quotient of around 0.24. The 30 events, which were coincident events between the Cherenkov veto and the plastic panels and were classified as class 3 and 4 all have a relatively high quotient of 0.85 or above. Thus, due to the broad spread around a quotient of 1, especially for low light events, and as the quotient for these 30 events is so close to 1, no cut in the quotient would select these events.

8.5.3   Conclusions form the timing structure

The time structure of the four different classes shows a clear difference for the bunch of events in the different classes. Nevertheless, a event-by-event analysis might lack due to the small number of channels. The quotient maximum/integral is a promising tool, since it gives a handle for discrimination between "fast signals" and "slow signals". In figure 52, one nicely sees, that for events with more and more light (thus, for more and more likely muons), this quotient drops down. Also, one sees that there are class 3 events which also show a small quotient. So, maybe, in this class, there are still some hidden muons. The coincidence analysis between Cherenkov veto and the preliminary plastic veto showed, that there were 30 coincident events classified as class 3 or 4 events. A first look on these events showed, that their quotient is relatively large (more than 0.85), which indicates that these are no real muons. But a further analysis with the fully equipped plastic veto as muon trigger for the Cherenkov veto might reveal muons in the classes 3 and 4 and might also give a good value for a possible cut.

8.6   Calibration

As described already in chapter 6, the PMTs were calibrated with the diffuser balls. This gives the opportunity to calibrate the integral light in the water tank to a muon track length.
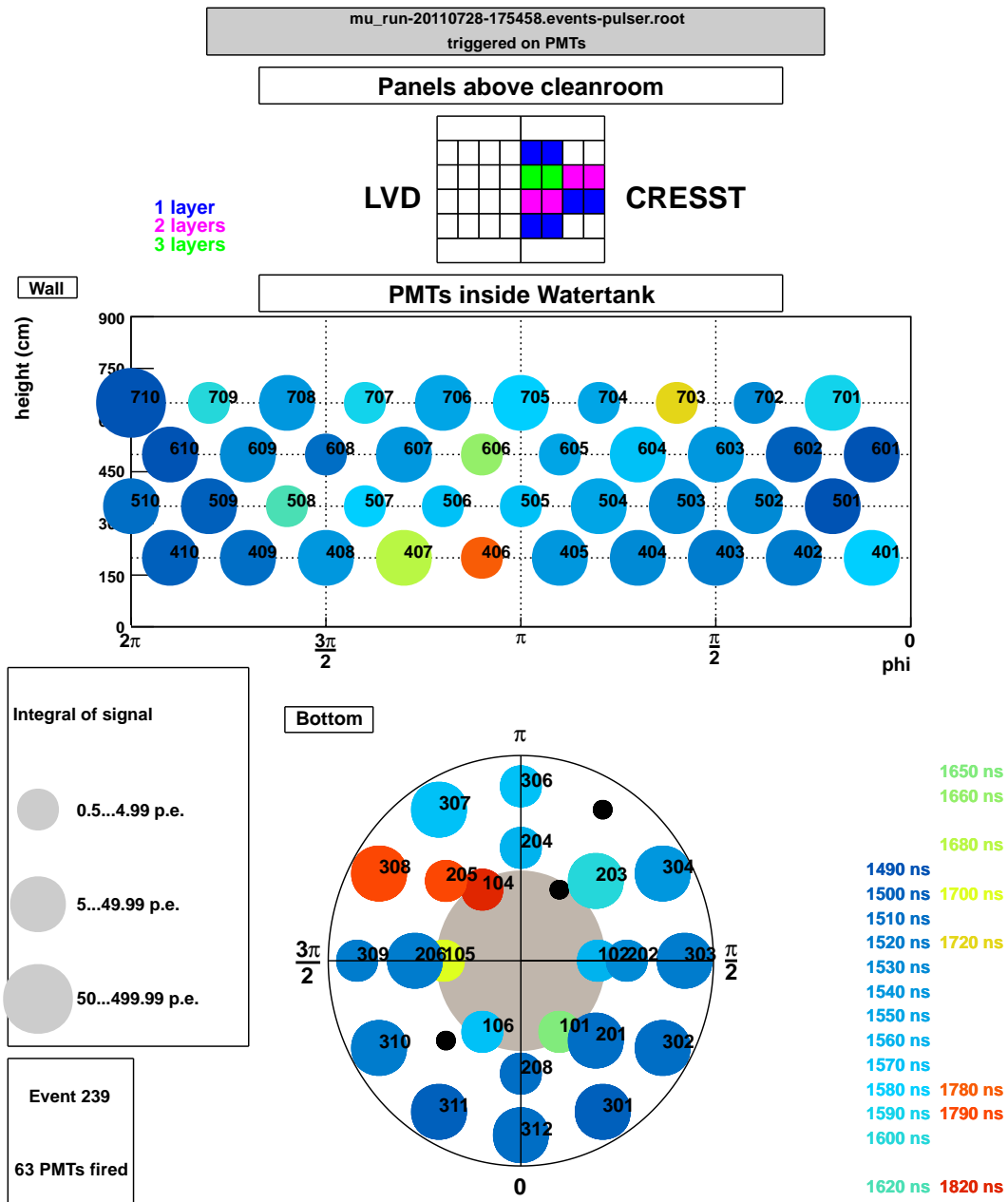
Figure 51: Example for an event. All 65 PMTs have fired. Each point corresponds to one PMT, color indicates the hit time, size corresponds to the amount of light. Also, two pixels of the panels have fired. As there are three layers of plastic scintillators, a horizontal stripe corresponds to one panel, where a vertical stripe corresponds to two layers of panels.
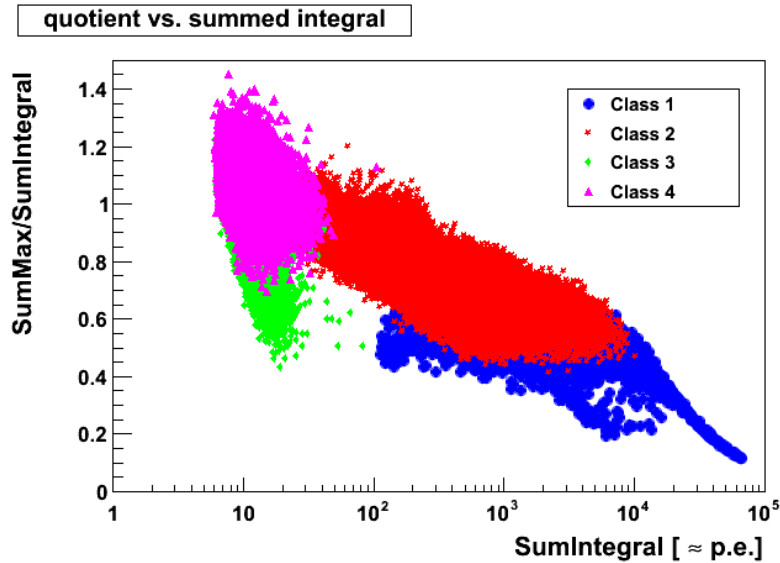
Figure 52: Maximum/Integral vs. Integral of all events. This plot shows the quotient between the recorded maximum of one event and the recorded integral versus the recorded integral. For events with a high integral, this quotient is around 0.1 - 0.2, while for a small integral, it is at around 1.

8.6.1   Light inside the water tank

As it was shown in chapter 2.4.2, a muon with an energy of 270 GeV traversing through water produces around 270 photons per cm through the Cherenkov effect. Due to several effects as reflections, wave length shifting, absorption, quantum efficiency of the PMTs, the PMTs would not detect all of these 270 photons. But it should be possible to derive an effective factor f_{eff} which contains all these factors to convert the amount of light detected in the water tank to a muon track length.

To get this "effective factor" f_{eff}, one can take the "pillbox" as the ruler, since it is quite separated from the rest of the water tank. As shown in ref. [Ahl93], most of the muons at LNGS come from an elevation of 60°, the mean travel path length through the 1.5 m high pillbox is around 1.8 m. Thus, in average one would expect 48600 photons to be produced for a "standard muon" traversing the pillbox. The coverage of the surface with the cathodes of the PMTs in the pillbox is the same as for the whole water tank ($f_{surface} = 0.005$). This leads to 243 photons, which reach the PMTs. As one can see in figure 54, the number of photoelectrons detected inside the pillbox vary from one single p.e. to several hundreds. Assuming, that muons traversing the pillbox are the only effect producing a huge amount of photoelectrons, one can conclude, that the highest peak is made by muons. This peak has a distribution from 100 p.e. to 300 p.e., with a mean value of 170 p.e.. A comparison between the recorded 170 ± 50 p.e. and the expected 243 p.e. leads to the conclusion, that $f_{eff} = 0.7 \pm 0.2$. The mean free path length of light in water is in the order of 10 m, and the mean track length in the pillbox is in the range of 2 to 3 m. Thus, a photon produced in the pillbox could be reflected 4 to 5 times, especially as the VM2000 is covering all surfaces and
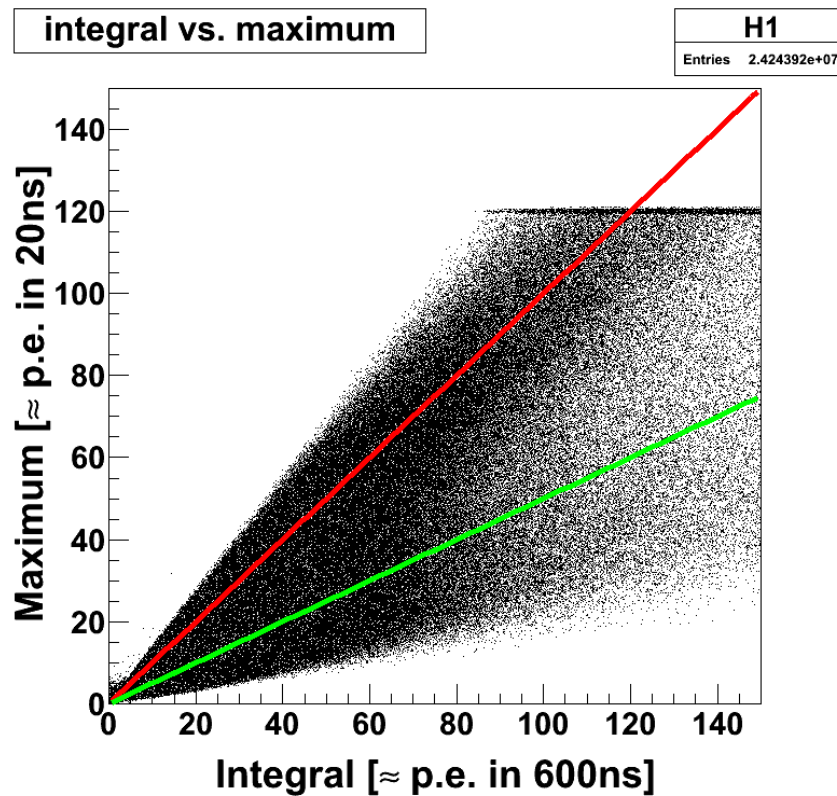
Figure 53: Integral vs. Maximum of the recorded single PMT pulses. The maximum is the amount of light registered within 20 ns around the first pulse of the PMT, while the integral is the amount of light registered on the PMT within 600 ns around the trigger time. The red line indicates a correlation of maximum = integral, which means, that the PMT "saw" light at one time, while the green line indicates maximum = 1/2×integral, meaning that the light arrived at the PMT at (several) different times.

has a high reflectivity. This balances out the quantum efficiency of a PMT, which is typically in the range of 20 %. Those both estimations also lead to an effective factor in the same order of magnitude.
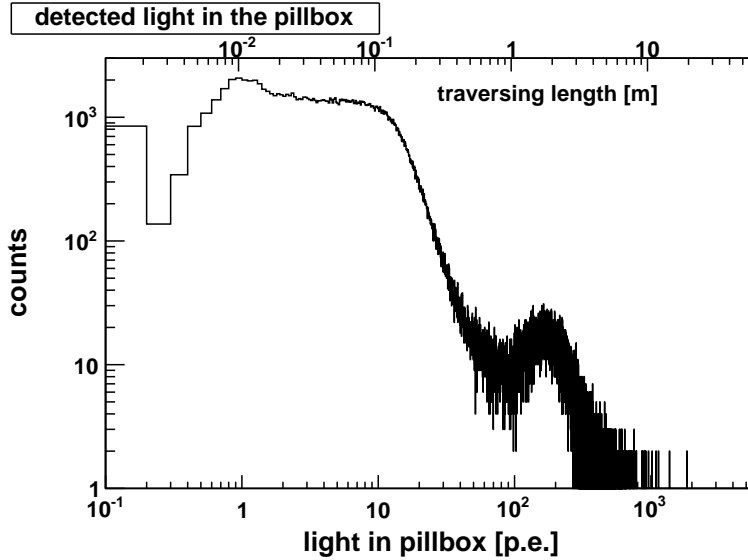
Figure 54: integral light in the pillbox.

So, the overall reduction factor f calculates to:

$$f = f_{surface} \cdot f_{eff} = (3.5 \pm 1.0) \cdot 10^{-3}$$

With f derived from the light inside the pillbox, one can calculate the expected amount of photo-electrons for a muon track of one meter. While a muon is traveling through one meter of water, 27000 photons are produced, so, one would expect around 90 ± 30 photoelectrons for a 1 m muon track (or 0.9 ± 0.3 p.e./cm). This is in good agreement with the results form the Borexino experiment, which achieved a p.e. yield of 2-3 p.e./cm [Pan07]. This is higher than in GERDA, but the Borexino veto has a PMT coverage of 1 % where the GERDA muon veto has a coverage of 0.5 %. A muon traversing the whole water tank from top to bottom from zenith angle (≈ 9 m) would produce around 243000 photons. These events should be recorded easily. But what about muons which are only scratching an edge of the water tank, only traveling some centimeters in water? These muons might populate the "low multiplicity bump". This question will be answered in Section 8.7.4. But before, a short look on three other possible explanations for the "low multiplicity bump" will be presented.

8.7   The low multiplicity bump

In this section, several ideas about the origin of the previously mentioned "low multiplicity bump" are presented. In this bump, which corresponds to class 3 and 4, around 45.000 events were recorded during the 83.52 days of measurement, which is comparable to a count rate of $6.2 \cdot 10^{-3}$ cts/s. Several different ideas to explain the bump are presented, reaching from random

coincidences between several photomultipliers via Cherenkov effect due to electrons to scintillation of the VM2000 and muons with a short track in the water tank.

8.7.1   Random coincidence of Cherenkov photomultiplier

To investigate the origin of the "low multiplicity bump", random coincidences between the photomultiplier as a possible explanation have to be considered. In this subsection, the rates of random coincidences will be calculated to check this hypothesis. As described in chapter 5, the GERDA muon veto does not trigger on a set of single photomultiplier, the trigger is realized with the majority trigger of the installed FADCs. The "trigger out" of one FADC is active, if at least one of the 8 channels on the board matches the trigger criteria, i.e. a FADC gives a trigger, if one or more channels of the FADC fired. The "trigger out" of all FADCs are fed into the MPIC module (Sec. 5.1.3), which determines, if more than a specified number of different FADCs fired within a given time window. If so, a trigger pulse is created, which stops the data acquisition for this event. To get the random coincidence rate of the FADC trigger, one needs the trigger rate of each single FADC and the criteria chosen. For a rough guess, one also can take the mean trigger rate of the photomultipliers and the number of photomultipliers per FADC, and calculate the mean FADC trigger rate. Measurements in Tübingen taken before the shipment to LNGS showed a mean trigger rate of $R_{PMT} = 2834\,\mathrm{cts/s}$ for the PMTs (see Tab. 5). As there are 65 PMTs distributed to 10 FADC, one can take $R_{FADC} = 6.5\,\mathrm{PMTs/FADC} \cdot 2834\,\mathrm{cts/s} = 18421\,\mathrm{cts/s}$ as a start value for each FADC. An upper limit for a random coincidence of x FADCs out of Y FADCs (R_{Y-x}) within a time window of τ is then calculated according:

$$R_{Y-x} = \binom{Y}{x} \cdot R_{FADC}^x \cdot \tau^{x-1} \tag{8.1}$$

The trigger criterion for the Cherenkov veto was given by 5 FADCs out of 10 FADCs within 60 ns, which gives:

$$R_{10-5} = \binom{10}{5} \cdot R_{FADC}^5 \cdot \tau^4 = 6.93 \cdot 10^{-6}\mathrm{cts/s} \tag{8.2}$$

With the online time of the measurement of 83.52 days, one would expect 50 events due to random coincidences of 5 FADCs, which is 1000 times less than measured in the bump and thus far away to be a realistic explanation for the bump.

The random coincidence rate for "more than 5 FADCs fired" is three orders of magnitude less, so it is negligible.

As the PMTs are grouped in FADCs, and the trigger is based on "x FADCs have fired", the number of fired PMTs does not have to be the same as the number of fired FADCs. The trigger criterion was "5 FADCs fired within 60 ns", So, an event with six firing PMTs on 5 FADCs would also fulfill the trigger criterion. Four of the fired FADCs are housing one fired PMTs each, while one FADC houses two of the fired PMTs. Formula 8.1 has to be modified.

First, one needs the random rate of two PMTs on one FADC, R_{2PMT7} for the FADCs with seven PMTs and R_{2PMT6} for the other FADCs:

$$R_{2PMT7} = \binom{7}{2} \cdot R_{PMT}^2 \cdot \tau = 10.12\mathrm{cts/s} \text{ and } R_{2PMT6} = \binom{6}{2} \cdot R_{PMT}^2 \cdot \tau = 7.23\mathrm{cts/s} \tag{8.3}$$

In addition, one needs the random rate of four firing FADCs out of the remaining nine FADCs:

$$R_{9-4} = \binom{9}{4} \cdot R_{FADC}^4 \cdot \tau^3 = 3.13 \cdot 10^{-3} \text{cts/s} \qquad (8.4)$$

For the rate "six photomultiplier on five FADCs", one has to multiply these two values (for two PMTs on one FADC, one can take the higher value R_{2PMT7}). To get the overall rate, one has to multiply this with 10, to account for the permutation of the "double hit FADC" through all ten FADCs.

$$R_{6PMT-5FADC} = 10 \cdot R_{2PMT7} \cdot R_{9-4} \cdot \tau = 1.90 \cdot 10^{-8} \text{cts/s} \qquad (8.5)$$

The random rate of 6 photomultiplier firing on 6 FADCs (R_{10-6}) is a factor of 3 lower ($6.38 \cdot 10^{-9}$ cts/s), both rates are way too low to explain this bump. Both rates together would contribute with 0.18 counts during the data acquisition time.

As rates of random higher multiplicities steeply decrease, random multiplicities are not responsible for the "bump".

8.7.2   Cherenkov effect due to electrons

As described in chapter 2.4.2, a charged particle traversing the water tank with a velocity larger than $3/4\,c$ is causing emission of light due to polarization of the water molecules. Electrons reach this velocity when they have an energy of 772.6 keV, so, if there are electrons of at least 772.6 keV inside the water tank, these would also lead to Cherenkov effect. Such electrons could be created by the photoeffect of a γ from a radioactive decay in the steel tank. The highest γ-line in natural decay chains is the 2.615 MeV line of ^{208}Tl. Thus assuming this γ undergoes photoeffect with an electron, this electron will be the origin of Cherenkov photons for only ca. 1.5 cm (Equation 2.6), leading to around 400 photons being produced. With the coverage and effective factor given above, this leads to 1.4 p.e.'s. As the trigger is at more than 5 PMTs fired (i.e. more than 5 p.e.), Cherenkov light due to electrons will not be seen by the detector, and cannot be the explanation for the "bump".

8.7.3   Scintillation of VM2000

The foil VM2000 mounted on nearly every surface of the water tank is wavelength shifting. A UV photon excites a molecule of the foil, which is emitting optical photons when de-exciting. The exact composition of the foil is not known since it is a manufacturer secret. A possible explanation for the "low multiplicity bump" might be scintillation of the foil due to incident ambient γ radiation, α particles or neutrons. But since there is no information available for scintillation of the foil, only a rough guess is possible.

For this guess, one can take results from investigations of the CRESST[2] collaboration. The dark matter experiment CRESST wants to detect the hypothetical dark matter particle WIMP through direct hits of this WIMP in a CaWO$_4$ crystal. If energy is deposited, the temperature of the crystal increases by a small amount of some μK, and in addition, this crystal scintillates.

---

[2]**C**ryogenic **R**are **E**vent **S**earch with **S**uperconducting **T**hermometers, located as next neighbor to GERDA in LNGS.

Thus, an energy deposition creates a phonon and a photon signal. The detectors consist of a 300 g CaWO$_4$ crystal with a superconducting thermometer attached to measure the temperature increase, a light absorbing wafer with attached superconducting thermometer measures the light output. To collect most of the light, these modules are encapsulated in VM2000. Due to quenching, CRESST can discriminate between γ and e$^-$-like events, events caused by interactions with the atomic shell (no quenching) and α, neutron or WIMP-like events, caused by interactions with the nucleus. Here, the quenching leads to less light as the comparable energy deposition due to electrons or γ's.

As shown in [Lan10], an α particle with 5.3 MeV (produced in the decay $^{210}Po \rightarrow^{206} Pb + \alpha$), impacting on the VM2000 foil produces the same amount of light as a 80 keV γ or electron depositing the energy in the CaWO$_4$. In CRESST, this is used to get rid of the signal produced by the lead atom impacting the CaWO$_4$ crystal, since without the foil, only the lead atom would be seen as an event in the recoil band.

But this scintillation event can also be used to estimate the amount of light produced by an α impacting on the foil.

For CaWO$_4$, around 5 % of the energy deposited by a γ or electron is re-emitted as optical light. In this case, the 80 keV γ mentioned above would lead to 4 keV, which are released as photons, the same amount of light is produced by an α particle impacting on the VM2000 foil. As optical photons have energies around 3 eV, this means, that around 1300 photons are produced. Together with the factor f $= 3.5 \cdot 10^{-3}$, derived in Section 8.6.1, this leads to 4.5 p.e. registered in the GERDA μ-DAQ. This is slightly below the region of the "low multiplicity bump". But as this is just a rough guess, lacking detailed measurements of the scintillation properties of VM2000, this guess still gives the idea that scintillation of VM2000 due to incident α-particles might be a good candidate for these events. In the bump below 20 fired PMTs, 44567 events are present. If all of these events would be caused by α particles depositing their energy in the VM2000, one ends up with an α rate of $6.2 \cdot 10^{-3}$ cts/s.

To compare this value with the radioactivity of the stainless steel tank, one first has to calculate the surface of the water tank, the cryostat and the pillbox. To get an approximation, one can simplify the geometry by taking just cylinders. The surface amounts to 500 m^2 stainless steel. The range of an α particle with 5.3 MeV in iron is 10.4 μm [Ber05], this gives the effective thickness of the steel one has to take into account. α particles from a deeper position would be shielded by the steel itself. This gives a volume of 5200 cm^3 stainless steel or 40 kg, which would contribute to α radiation. In [Man08], the radioactivity of the stainless steel for the GERDA tanks have been determined, giving an upper bound of of less than 2 mBq/kg due to the decay chain of ^{228}Th. Taking this number and the 40 kg estimated above, one would expect 80 mBq. Thus, if one α out of 10 leads to a scintillation of the VM2000, this would be enough to explain the "low multiplicity bump".

We consider α decays as the most plausible explanation for the bump.

8.7.4   Short muon tracks

In section 8.6.1, a value for "p.e. per meter muon track" was calculated (90 $\pm$ 30 p.e./m). Thus, one can rescale a histogram of the amount of light detected into a histogram of the path length of a muon. In figures 54 and 55, the integral light in the pillbox and in the whole water tank is plotted with two abscissas, one for the light detected and the other for the path length. In the pillbox

(fig. 54), there is the broad peak at around 1.8 m, which was used to define the effective factor for the light detection. One also sees a huge bump at short distances (between 10 cm and 1 m). In the respective plot for the whole water tank, figure 55, one nicely observes a steep drop at $\approx$ 10 m, corresponding to the maximal track length for a traversing muon (i.e. a geometrical cutoff). Also here, a huge bump at low intensities, corresponding short tracks (10 - 30 cm) is visible. The huge amount of these events would lead to the conclusion, that (if these events are muon events), several muons are only having short tracks in the water tank, just scratching the edge of the water tank. To derive the amount of muons which produce less than around 30 p.e. (equivalent a track length of less than around 30 cm), the simulations were used. For the simulation, the GERDA setup was strongly simplified. A cylinder with 5 m radius and 9 m height simulated the water tank, while the cryostat was represented by another concentric cylinder of 2 m diameter and 5.60 m height. Muons are produced starting in a disk with 20 m diameter, 8.10 m above the center of the cryostat. For each muon, a randomized starting point in the disk together with a randomized path direction and energy is defined according to the muon spectrum measured by the MACRO experiment [Ahl93]. If the muons reached the water tank, their entrance and exit points are calculated, both for the water tank and for the cryostat and also the track length inside the water tank was calculated. In figure 56 the simulated track length of muons is histogrammed. Also here, a steep drop at $\approx$ 10 m is visible due to the geometrical cutoff. In addition, three bumps are visible at 3.5 m, 7 m and 9 m, which are all due to geometric reasons. These bumps are not visible in the measured light histogram, figure 55, as those geometric issues are compensated by the reflectivity and wave length shifting properties of the VM2000 foil. Nevertheless, the huge bump at short distances, which is prominent in the measured light histogram vanishes in the simulated data, leading to the conclusion, that these events are not caused by muons.
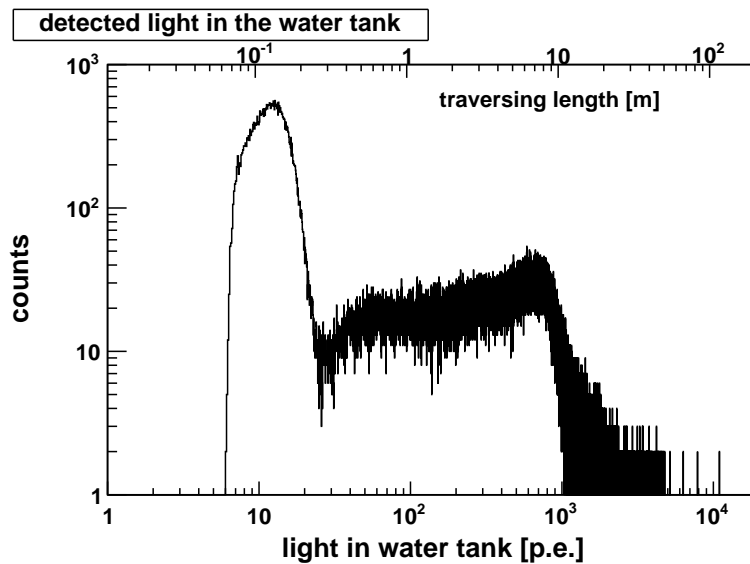
Figure 55: integral light in the water tank.

Table 7 summarizes the results of the analysis of the simulated muons. Figure 57 shows the entry and the exit points on the water tank surface of muons with a track length of < 32 cm. As one sees, most of the muons are traversing the water tank at the upper or the lower border of the
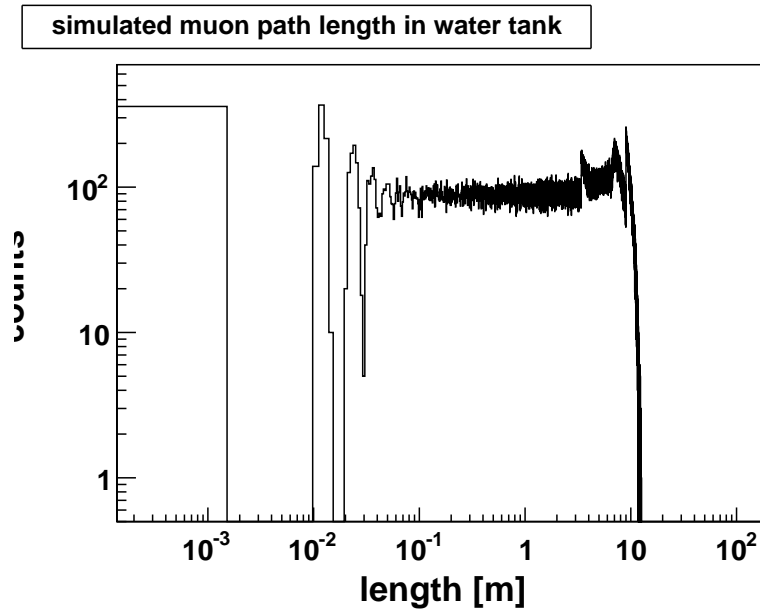
simulated muon path length in water tank

Figure 56: Path length of simulated muons. The path length was calculated only geometrically, no reflection was included.

water tank cylinder, only a small amount of muons are scratching the lateral surface. Nicely seen are "double points", where one point is the entrance and the other corresponds to the exit point of the muon which come almost tangential to the cylinder. In the simulated spectrum with only muons, only 2.32 % are muons with a track less than 32 cm. During data taking, 303049 events were recorded, the corresponding 2.32 % would be 7019 events. In fact, there are around 45000 in the region which corresponds to less than 32 cm, a factor of 6 more than expected. Thus, "short track muons" alone can not explain the "low light bump".

Table 7: simulated muons.

	events	%
All muons	8491197	972%
hit water tank	873581	100%
hit cryostat	170658	19.5%
length in water tank $< 32\,\mathrm{cm}$	20223	2.32%
($32\,\mathrm{cm} \triangleq 30\,\mathrm{p.e.}$)		
length in water tank $\geq 32\,\mathrm{cm}$	853358	97.69%
length in water tank $\geq 60\,\mathrm{cm}$	835109	95.60%
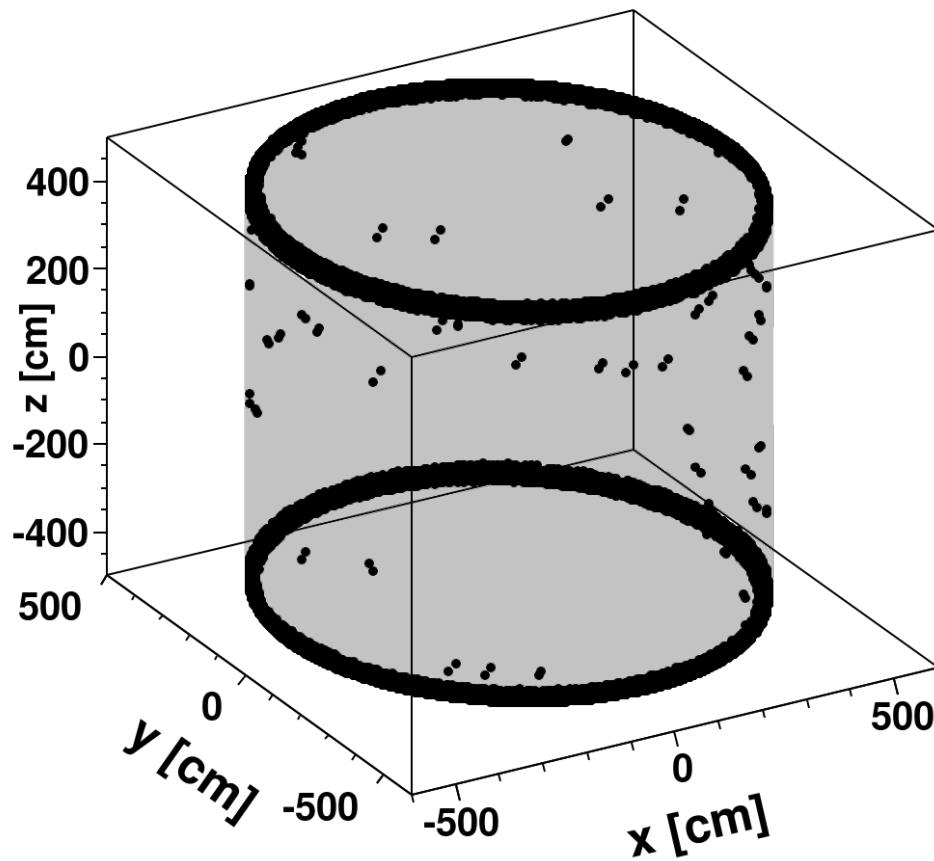
Figure 57: Entrance and exit points of simulated muons with short tracks in the water tank. The water tank is indicated as the gray area. A muon is represented by two points, the entrance and the exit point. Most of the muons with a short track are scratching the tank at the borders, the black circles. Only a small amount traverses the water tank on the lateral surface, which are seen as "double points". In total, the entrance and exit points of more than 20000 muons are plotted, this corresponds to almost 3 years of data taking.

8.7.5   Hit pattern

If the origin of the bump was a light leak or something spatially limited, one would expect to have "hot spots" when looking in the hit pattern. Figure 58 shows the summed hit pattern for events with up to 20 p.e.'s. Due to the spacial separation, it is more likely, that such events occur in the pillbox. Thus, for this plot, these PMTs were taken out of the analysis. Except of one noisy PMT (509), no clustering or pattern becomes visible. Thus, the origin of the low multiplicity bump is not concentrated in a special volume inside the water tank. This might be a hint that ambient radioactivity for example from the steel of the water tank is responsible for this bump.
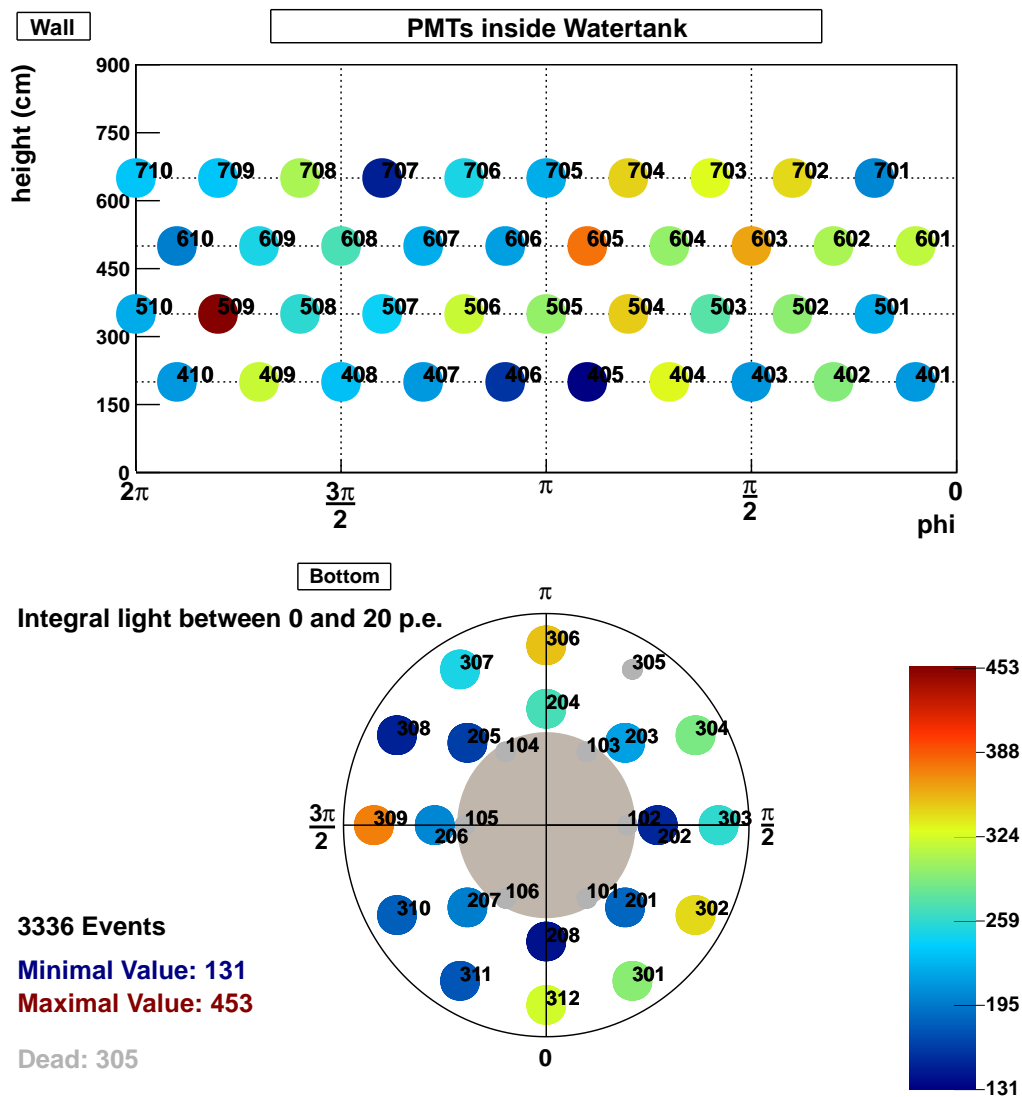
Figure 58: Hit pattern for events with less than 20 p.e.: no hot spot becomes visible, also no clustering.

Also the histogram of the light, a PMT collected if not more than 20 PMTs fired (fig. 59) and the histogram of the rate, how often a PMT fired (under the assumption, not more than 20 PMTs

fired, figure 60) only reveal the pillbox PMTs and PMT 509 to have fired more often than the others.
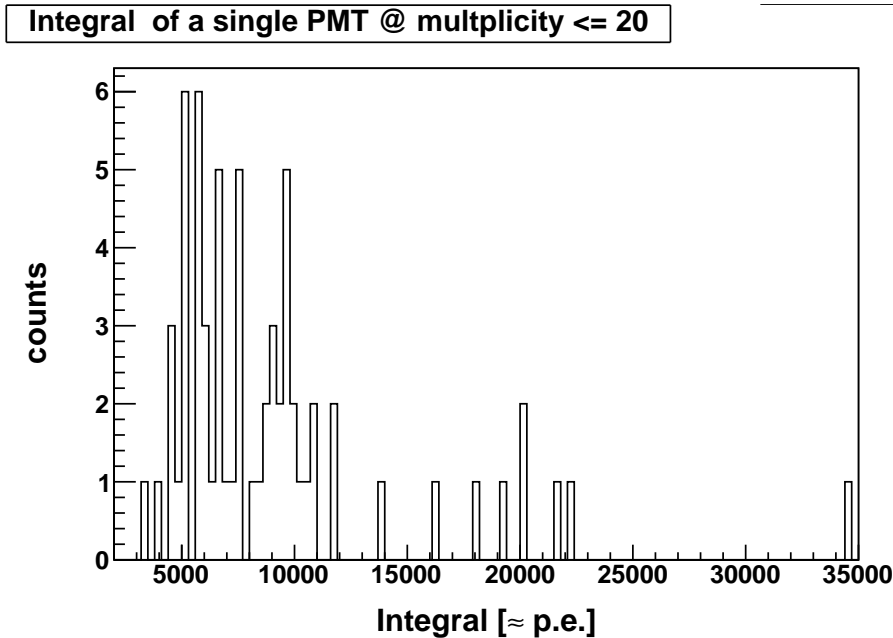
Figure 59: Summed intensity histogram of the individual PMTs. This histogram is drawn for the sum off all events with ≤ 20 PMTs. One clearly sees 9 PMTs saw more light than the others. 6 of them are the pillbox PMTs, since this volume is well separated from the rest, and since it is quite small, light produced inside could be reflected several times before reaching a photocathode. The other three are distributed through the water tank, thus, there is no obvious hot spot.

This leads to the conclusion, that there is no locally concentrated light source for the "low multiplicity bump", since no region and no single PMT is responsible for the low multiplicity bump. An α contamination in the steel of the water tank is a good explanation for such a homogeneously distributed production of low light.

8.8   Final muon cut

In Section 8.7, it could be shown, that even without a final explanation for the "low multiplicity bump", a relatively simple cut on the integral light recorded (≥ 30 p.e.) suppresses this bump without cutting too many muons.
As one can see in Tab. 8, the ≥ 30 p.e. cut gives an event rate of $3.6 \cdot 10^{-2}$ cts/s or 2.15 cts/min, and also the cut ≥ 60 p.e. gives an event rate of 2.11 cts/min, which is in good agreement with the simulated 2.5 cts/min calculated in [Pan07], where only muons with 60 cm track length in the water tank were taken into account.
The impact of a cut on ≥ 30 p.e. on the events classified as muons (i.e. classes 1 and 2) is almost negligible. After a cut on ≥ 30 p.e., the data include all events, which formerly were classified as

rate of a single PMT @ multplicity <= 20
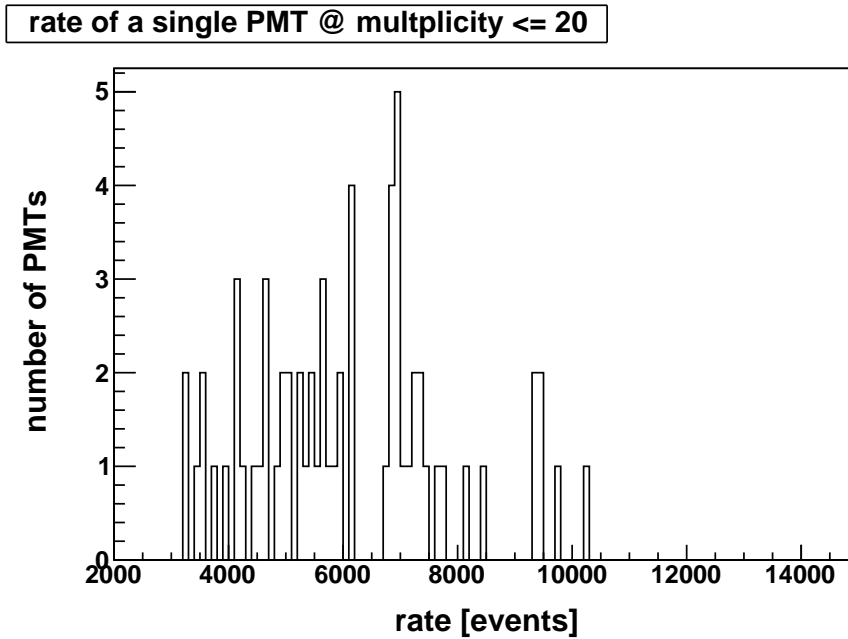
Figure 60: rate histogram of the individual PMTs. This histogram is drawn for a trigger of ≤ 20 PMTs. For each PMT, it is calculated, how often the PMT fired. 8 PMTs fired more than 8000 times. 6 of them are the pillbox PMTs, while the upper most is the noisy PMT "509".

class 1 or 2, except 226. This means, 99.91 % of class 1 or 2 events survive the cut. In addition 16 events of class 3 and 134 events of class 4 also survive the cut. Thus, 99.94 % of the events selected by a cut ≥ 30 p.e. are muons, and 0.06 % are contaminations. In Table 9, the result of the cut for the different classes are listed, figure 61 shows the corresponding histogram. Most of the class 1 and 2 events survive the cut, while most of the class 3 and 4 events do not. The efficiency for this cut, $\epsilon_{interpr}$, is then calculated to $\epsilon_{interpr} = 0.9991 \cdot 0.9994 = 0.9985$. Thus, the final muon cut is defined: **all events with ≥ 30 p.e.**.

Table 8: rate of events for different cuts.

cut	# events	rate (1/min)
no cut	303049	2.52
≥ 30 p.e.	258278	2.15
≥ 60 p.e.	253625	2.11

Table 9: Comparison of the $\geq 30\,\mathrm{p.e.}$ cut for the different classes.

	class 1	class 2	class 3	class 4
All events	31050	227304	9734	34961
$< 30\,\mathrm{p.e.}$	0	226	9718	34827
$\geq 30\,\mathrm{p.e.}$	31050	227078	16	134
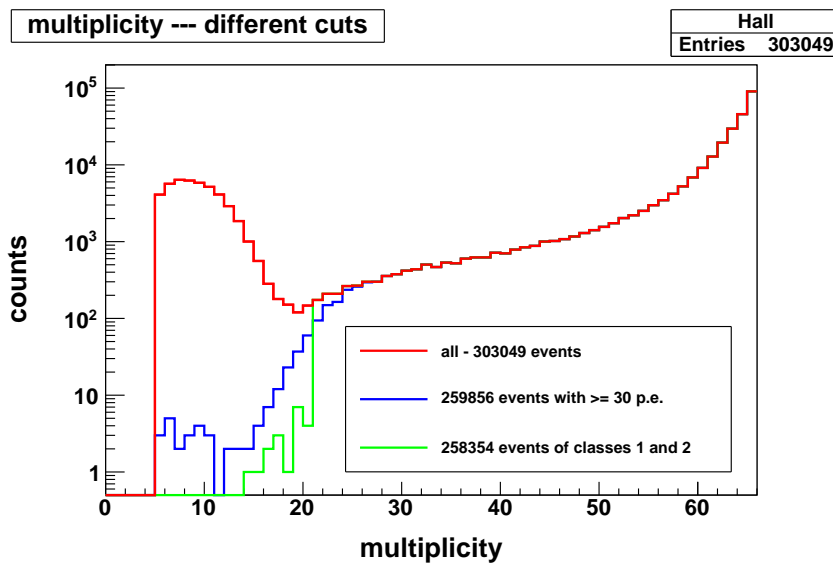
Figure 61: red: all events, blue: all events with $\geq 30\,\mathrm{p.e.}$, green: all events of the classes 1 and 2. The structure above a multiplicity of 20 PMTs remains almost the same with all cuts, while the bump at low multiplicities is strongly suppressed with both cuts.

8.9   Muon veto efficiency

In the preceding section, the final muon cut was defined. To calculate the muon veto efficiency ϵ, basically three different parts need to be calculated.

- geometrical factor: As described in Section 8.7.4 and summarized in Table 7 therein, 97.7 % of the muons reaching the water tank have a track length of > 32 cm. This length corresponds to 30 p.e..

- combinatorial factor: what is the possibility, that 30 p.e. are distributed on less than 5 FADCs? An answer to this question is given in the following subsection.

- interpretation factor: an offline cut ≥ 30 p.e. as chosen before loses 0.01 % of the muons classified as class 1 or 2. In addition, 0.06 % of the events surviving the cut are events of class 3 or 4. All together, the interpretation factor is 99.85 % (see Tab. 9 and the calculation on page 89).

As both the geometrical and the interpretational factor are described in section 8.7.4 and section 8.8, only the combinatorial factor is described in the following subsection.

8.9.1   Some combinatorics

Taking a given amount of photoelectrons, which have been detected, one has to look at the possibility, that a muon traversing the water tank is NOT been detected. Of course, this is more likely for muons with a short track in the water tank. In section 8.7.4, it could be shown, that most of the events with less than 30 p.e. do not correspond to muons, and those muons, which are contributing to the bump, are muons which are only scratching the water tank. As it was shown in section 8.6.1, one centimeter path length corresponds to 0.9 ± 0.3 detected photo electrons. Thus, these 30 p.e. correspond to 32 cm track length. If one take these 30 p.e. as an offline threshold, one can calculate the possibility, that a "32 cm muon" will not be seen by the Cherenkov veto. This can happen, if the 30 p.e. are distributed over less than 5 FADCs, since this was the hardware trigger threshold for the events. Here, the assumption is done that the photons are distributed isotropically, thus, the p.e. are also distributed isotropically. In reality, the Cherenkov photons are not distributed isotropically, but, as the surface of the water tank is covered with a highly reflective foil, the assumption of isotropic distribution is a good first pass assumption. To calculate the probability "k p.e. are distributed on n FADCs", one could think of it as an urn problem with 10 balls corresponding to the 10 FADCs, each ball is numbered to be identified. The number of photo electrons is represented by how many times a ball is drawn, with replacement of the ball. In which sequence the balls are drawn out the urn is not relevant, thus, the overall number of possible distributions is calculated by (after [Bro08]):

$$\binom{n+k-1}{k}$$

We have $n = 10$ balls in the urn, and $k = 30$ times, a ball is drawn out and replaced right afterwards.
This gives $\binom{39}{30} = 211915132$ possible combinations. Now, we try to find a recursive way to derive the amount of possible combinations for "x out of 10 FADCs are chosen in 30 times".

- In the next step, one has to calculate the number of combinations, which fulfill the criterion "only (and exact) one FADC is hit". There are $\binom{10}{1} = 10$ possibilities, that exactly one FADC out of ten is hit, which means, all 30 p.e. are registered on this FADC.

- The next step is "exactly two FADCs are hit". $\binom{10}{2} = 45$ possible combinations of two FADCs can be chosen out of 10. Thus, for the very first two rounds of drawing a ball, there are 45 possible events. For the rest of the rounds ($k_2 = 28$), only the possible combinations are relevant, where only $n_2 = 2$ FADCs are present, and 28 times, one of these is chosen ($\binom{2+28-1}{28} = 29$). The overall number of possible combinations is then calculated to:

$$\binom{10}{2} \cdot \binom{2+28-1}{28} = 45 \cdot 29 = 1305$$

.

- For "exactly three FADCs are hit", the two binomial coefficients calculate to $\binom{10}{3}$ and $\binom{3+27-1}{27}$, which gives the number of

$$\binom{10}{3} \cdot \binom{3+27-1}{27} = 120 \cdot 406 = 48720$$

possible events.

- The number of possible events for "exactly x FADCs are hit" is thus calculated to

$$\binom{10}{x} \cdot \binom{x+(k-x)-1}{k-x} = \binom{10}{x} \cdot \binom{k-1}{k-x}$$

.

To get the specific probabilities, these numbers have to be divided by the number of all possible events $\binom{39}{30}$. In Table 10, a summary is given. As one can see, the trigger "30 p.e. hit at least 5 FADCs" leads to a detection efficiency of 99.61 %. Of course, the same can be done for different amount of photo electrons. In figure 62 the "detection inefficiency" is plotted versus the number of detected photoelectrons. Indicated in red is 99.56 %, the efficiency given by simulations for muons with an energy deposition in the germanium detectors [Kna09].

This cut can now being applied for the coincident events, described in section 8.4. Tab. 11 compares the different cuts one can apply.

8.9.2   Overall muon efficiency

As the combinatorial factor is calculated as 99.61 %, all three factors are known. The overall muon efficiency can be calculated, taking the values ϵ_{geom} from Table 7 on page 85 and $\epsilon_{interpr}$ from page 89.

$$\epsilon = \epsilon_{geom} \cdot \epsilon_{combi} \cdot \epsilon_{interpr} = 0.9769 \cdot 0.9961 \cdot 0.9985 = 0.9717 \tag{8.6}$$

This is the efficiency to detect and identify **all** muons, which are hitting the water tank, despite of the track length or the interaction with the germanium detectors, taking the cut on 30 p.e.. In the simulations, however, a number of 99.56 % was given [Kna09]. But there, the efficiency

Table 10: detection efficiency for 30 p.e.'s on x FADCs.

x FADCs	$\binom{10}{x}$	$\binom{30-1}{30-x}$	number of possible solutions	probability	probability for $\geq$ x FADCs
0	1	0	0	0	1
1	10	1	10	4.71887e-08	1
2	45	29	1305	6.15813e-06	1
3	120	406	48720	0.000229903	0.99999
4	210	3654	767340	0.00362098	0.99976
5	**252**	**23751**	**5.98525e+06**	**0.0282436**	**0.99614**
6	210	118755	2.49386e+07	0.117682	0.96789
7	120	475020	5.70024e+07	0.268987	0.85022
8	45	1.56078e+06	7.02351e+07	0.33143	0.58123
9	10	4.29214e+06	4.29214e+07	0.202541	0.24980
10	1	1.0015e+07	1.0015e+07	0.0472595	0.04726
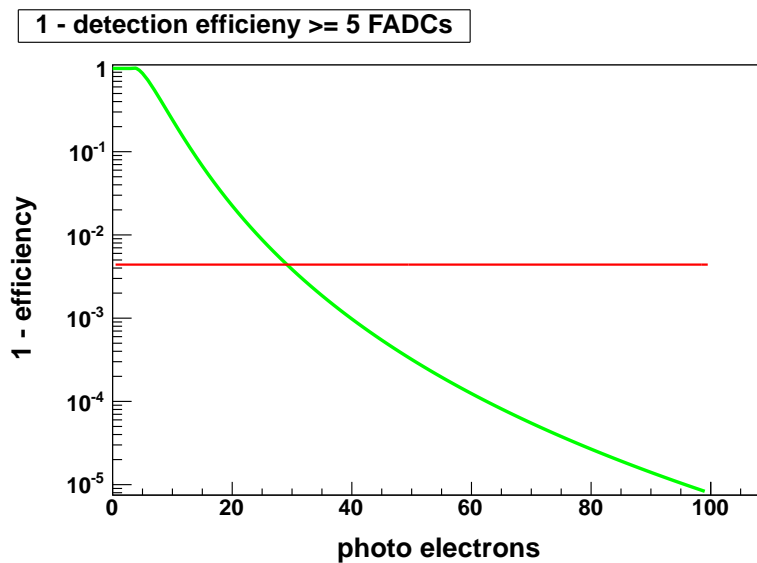
Figure 62: (1 - detection efficiency) for x photoelectrons to be detected on at least 5 FADCs is plotted. The red line corresponds to an efficiency of 99.56 %, which was given by simulations [Kna09].

Table 11: Comparison between classes and p.e.-cut

Cherenkov & plastic			
cut	# events	%	rate (cts/s)
all events	4536	100	$6.29 \cdot 10^{-4}$
classes 1+2	4506	99.34	$6.24 \cdot 10^{-4}$
$\geq$30 p.e.	4503	99.27	$6.24 \cdot 10^{-4}$

Cherenkov & Germanium			
cut	# events	%	rate (cts/s)
all events	107	100	$4.03 \cdot 10^{-5}$
classes 1+2	107	100	$4.03 \cdot 10^{-5}$
$\geq$30 p.e.	107	100	$4.03 \cdot 10^{-5}$

was calculated for muons with energy deposition in the germanium detectors. And in addition, the simulations were performed only for muons with a track length of more than 60 cm in water. Thus, the simulated efficiency is higher than the efficiency given here!

Nevertheless, if one tries to compare simulations and measurements, one should cut on muons of $\geq$ 60 cm track length. If the procedure of calculating the efficiency is repeated for muons with > 56.64 p.e. ($\triangleq$60 cm track length), assuming, these are 100 % of all muons, one arrives at 99.98 % ($\epsilon_{geom} = 1$, $\epsilon_{combi} = 0.9998$, $\epsilon_{interpr} = 1$). This is in fact more comparable and much closer to the simulated efficiency.

In Section 8.6.1, a conversion factor is given, to calculate the mean amount of photo electrons per track length. Assuming to have a muon with 60 cm track length, 56.64 p.e. are expected to be registered in average. As this is the average value, of course, there will be several of these muons with less than 56.64 p.e., but statistically 99.9926 % of all muons with 60 cm track length in the water tank would survive a cut of $\geq$ 30 p.e.. The combinatorial and the interpretational factors remain the same, thus, for muons with 60 cm track length in the water tank, the efficiency is calculated as:

$$\epsilon = 0.999926 \cdot \epsilon_{combi} \cdot \epsilon_{interpr} = 0.999926 \cdot 0.9946 = 0.9945 \leq 0.9946 \qquad (8.7)$$

For muons with a track length of more than 60 cm, this value increases, since it gets more unlikely to register less than 30 p.e.. This value is practically the same as the simulated 99.56 %. But once more, here, the efficiency is given for **all** muons with a track length of 60 cm, while the simulated value only accounts for muons with energy deposition in the germanium detectors.

Chapter 9

Conclusion

The very first data of the GERDA muon veto have been presented. By recording a large number of events in the water tank, it could be shown that that the setup works properly. Muons have been identified. Nevertheless, an enhancement at low light became visible. Up to now, the origin of these events could not be clearly identified. Several possible explanations as for example random coincidences of the PMTs were taken into account but all failed to explain the whole bump.

Coincidences between plastic veto and Cherenkov veto as well as between germanium detectors and Cherenkov veto could show, that most of the bump has no muonic origin. For the scintillation of VM2000, only a rough estimation could be presented, since up to now, there are no measurements investigating this. But this is at the moment the best explanation as the rough estimation is in the same order of magnitude as the bump properties. Measurements of the scintillation of VM2000 are urgently needed.

It could be shown, that the low light bump is equivalent to short track muons with less than 30 cm in water, but is caused by another (yet unidentified) physical process. Muons with a track length of less than 30 cm were never included in the simulations for the muon-induced background of the germanium diodes, since those muons and their secondary particles have no effect for the germanium diodes. For the simulations, a track length cut was applied for track lengths of > 60 cm.

In this work, the analysis revealed a rather simple cut of ≥ 30 p.e. to be suitable to suppress the bump sufficiently. A muon detection efficiency of 97.17 % for all muons hitting the water tank could be reached by using only the Cherenkov veto. Comparing the results with the input selection of the simulations, a muon detection efficiency of 99.98 % could be determined. Thus, the (online) hardware trigger of five FADCs, in connection with an offline additional trigger of ≥ 30 p.e. leads to a very promising muon detection efficiency.

Several tasks still have to be attached. First, the scintillation properties of VM2000 have to be studied, as this is the most promising candidate for the low light bump. Afterwards, a simulation of the scintillation of VM2000 due to radiation coming from the stainless steel tanks together with the light propagation in the water tank should test the hypothesis of the origin of the low multiplicity bump.

With the data derived from the VM2000 measurements, new extensive simulation of all muons (not only those muons depositing energy at the germanium diodes) have to be performed. There, the reflecting, wavelength shifting and scintillating properties of VM2000 will be implemented and the muon track length will be recorded. And, for all muons hitting the water tank, the full

Cherenkov chain should be performed, even for the muons only scratching the water tank. With these results, a comparison of the simulated data with the experimental ones should give a more detailed muon detection efficiency.

In addition, the plastic veto is now fully installed. Thus, the data taken with the full set of plastic panels can reveal an additional handle to pin down a "standard muon event". Maybe, also other tests can be performed with the plastic veto together with the remaining spare plastic panels as an external trigger for the Cherenkov veto. One can think about using the plastic veto and the additional panels to determine a muon track path through a part of the water tank. With data derived from that, one certainly can improve the track length calculations presented in this work.

Appendix A

Appendix

I   Display Tools

As written in chapter 5.3.2, several software functions have been developed. In the following pages, all functions are described.

I.1   GERDAPlotPrograms

During development, two ROOT files were developed, both with several plot functions which could be used to create the different plots. The first file was first mainly used for the Cherenkov veto only, then extended for the preliminary plastic veto. Finally, some corrections were done to account for the full equipped plastic veto. Its functions are described in this section. For the different functions, the user has to specify several parameters. If not further specified, $<rootfile>$ is the filename (with absolute or relative path), $<number\ of\ event>$ is the event, which has to be plotted, the number of the PMT under examination is given with $<PMT>$ (in accordance to the nomenclature described in chapter 4.3.2).

In addition, some "interactive" functions have been developed. Since printing them on paper is quite complex, here, just a brief explanation is given.

- Traces(<rootfile>,<number of event>):
  This is basically the same as "PlotTrace" (fig. 64), with one difference: the traces of all PMTs are plotted one by one, the user has just to press a key to switch to the next PMT.

- CreateMovie(<rootfile>,<number of event>):
  A .gif-movie is created, the event in a temporal resolution. For each clock tick, a picture is done, and these pictures are connected to one file. In section I.3, a web site is given, where one can find the several different types of movies.

- CreateMovieEvents(<rootfile>,<number of event to start>,<number of event to stop>):
  In the resulting .gif-movie, each event is represented by one picture, which are then added to this movie. Also an example of such a movie can be found on the web site given in section I.3.

97
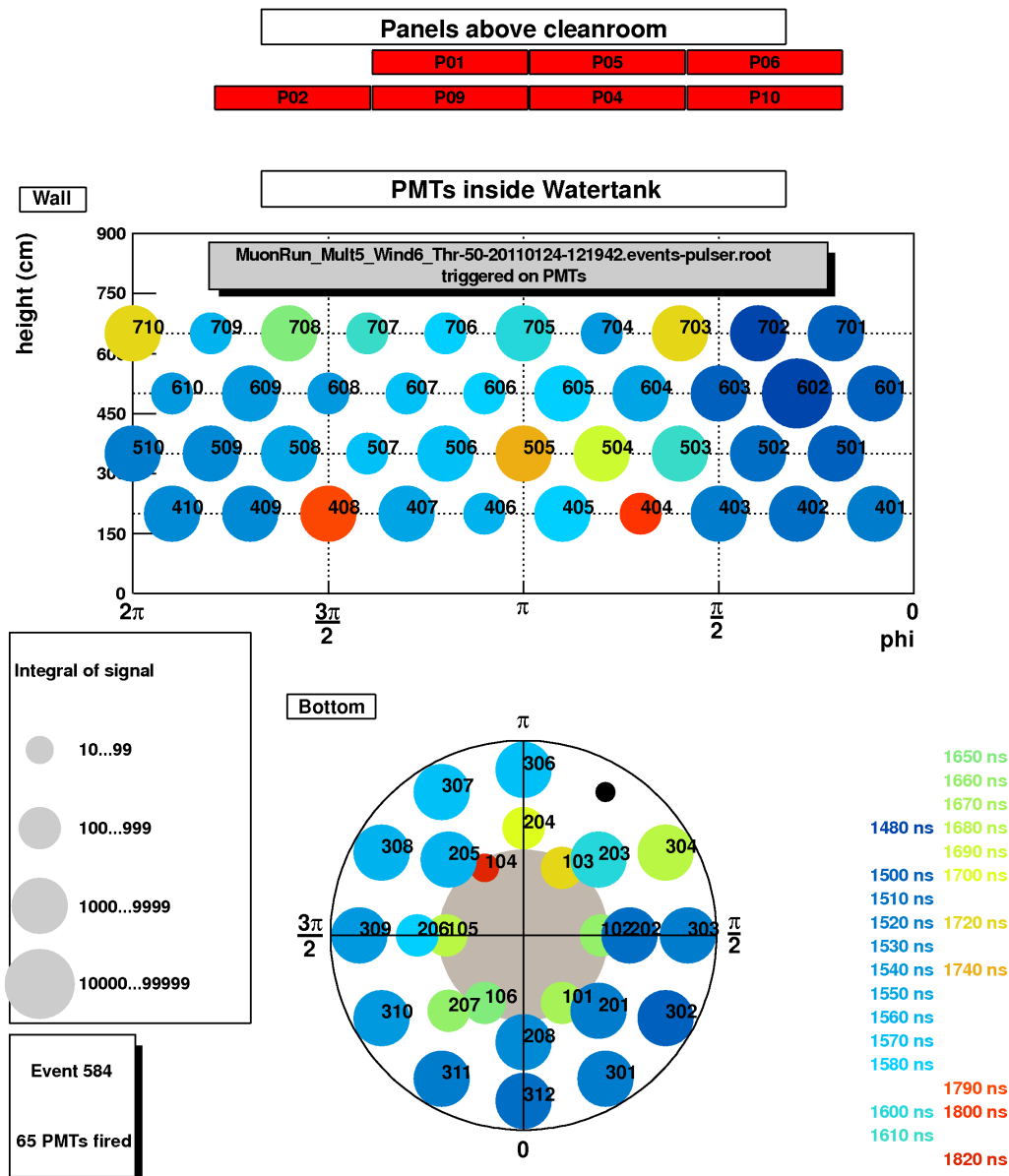
Figure 63: **PlotEvent(<rootfile>,<number of event>, <output filename>)**: This program plots a "muon map" of one event, a drawing of the water tank (a rectangular represents the wall, a circle represents the bottom). In this drawing each PMT position is marked by a colored dot. The color indicates the time, the PMT fired, and the size of this dot is a measure for the Intensity, this PMT recorded. By giving an output name, the plot is saved into a file. The type of the output file is just chosen by the ending. In this example, a full hit event is shown. A large dark blue circle corresponds to a PMT, which fired early and saw a lot of light. In the upper right area of the "wall", one sees a cluster of six huge blue dots, in the middle, PMT 602 is located. This cluster might be a Cherenkov cone of the primary particle.
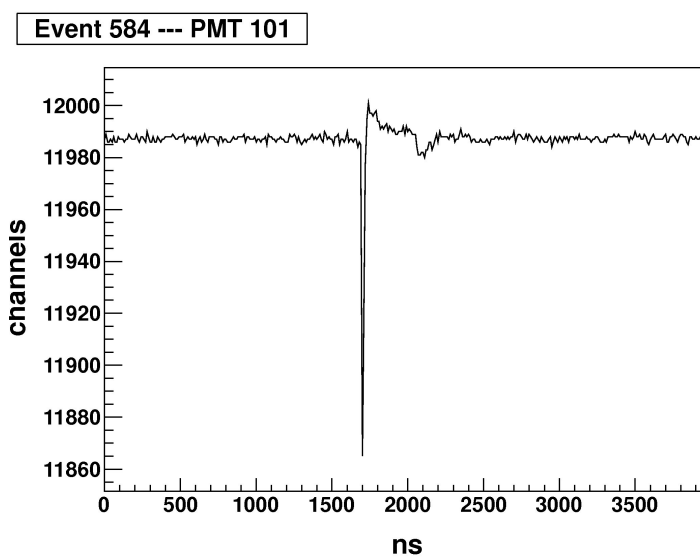
Figure 64: **PlotTrace(<rootfile>,<number of event>, <PMT>)**;The Trace of one PMT is plotted.
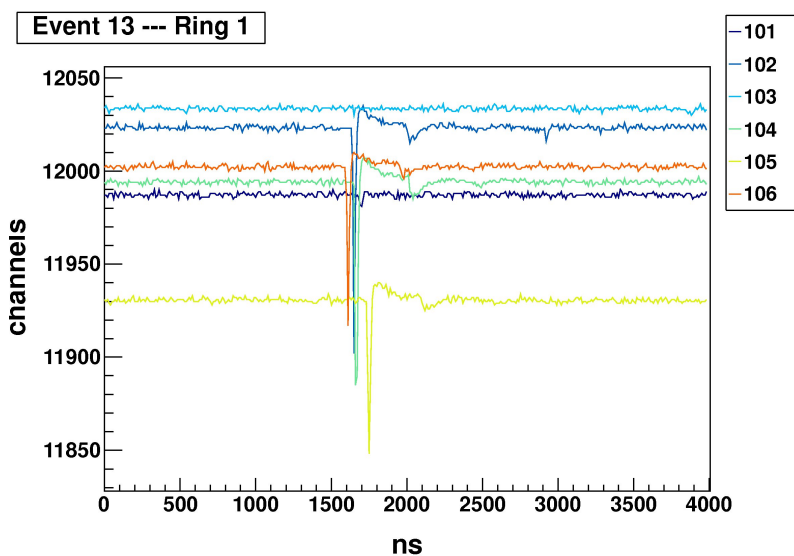
Figure 65: **PlotRing(<rootfile>,<number of event>,<number of ring>)**. "number of ring" is "1" for the pillbox, "2" for the inner bottom ring, "3" outer bottom ring, "4...7" for the rings on the wall, and "8" for the plastic panels. This program produces a plot of the traces of all PMTs contained in the specified ring. In this case, the ring 1, the "pillbox" is plotted. Four PMTs recorded a light pulse, but PMT 101 and 103 did not record light.
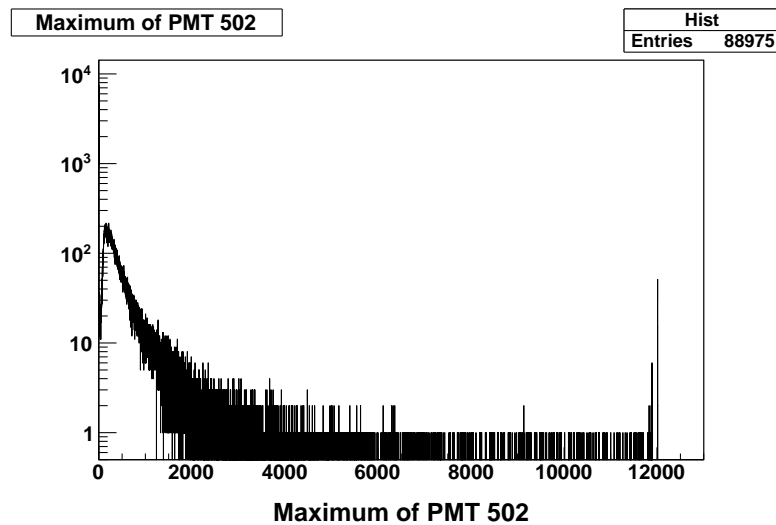
Figure 66: **HistogramVariable(<rootfile>,<name of variable>, <PMT>)**: To plot histograms of different variables, this function can be used. The possible names are *"Integral"*, *"Hit"*, *"Max"*, *"HitTime"*, *"SumIntegral"*, *"SumIntegralAll"*, *"SumMax"*, *"firedPMTs"*, *"firedPillboxPMTs"*, *"sincelast"*, *"PanelHit"*, *"PanelIntegral"*, *"PanelHitTime"*, *"PanelMax"*. Here, as an example, the histogram of the maximum of one PMT. (100 correspond to one s.p.e.)
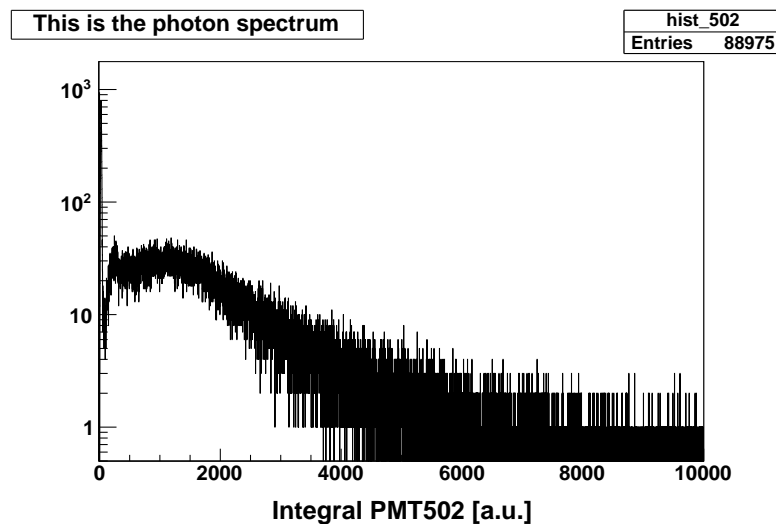
Figure 67: **PlotHisto(<rootfile>, <PMT>)**: While converting, for each PMT, a histogram or the pulse integral is created. With this function, one plots this histogram. 200 corresponds roughly to one single photo electron.
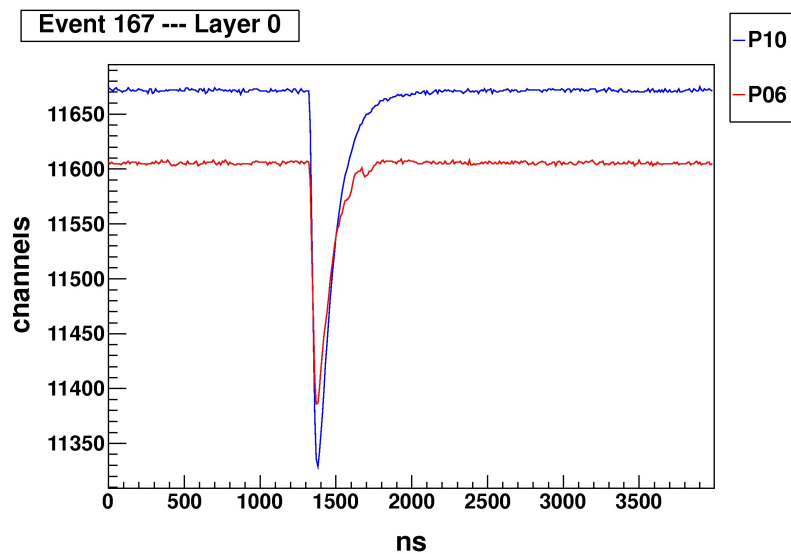
Figure 68: **PlotTracePanel(<rootfile>,<number of event>,<number of layer>):** The two traces of the panels corresponding to layer "0...3" are drawn.In blue, the lower panel is drawn and in red the upper panel.
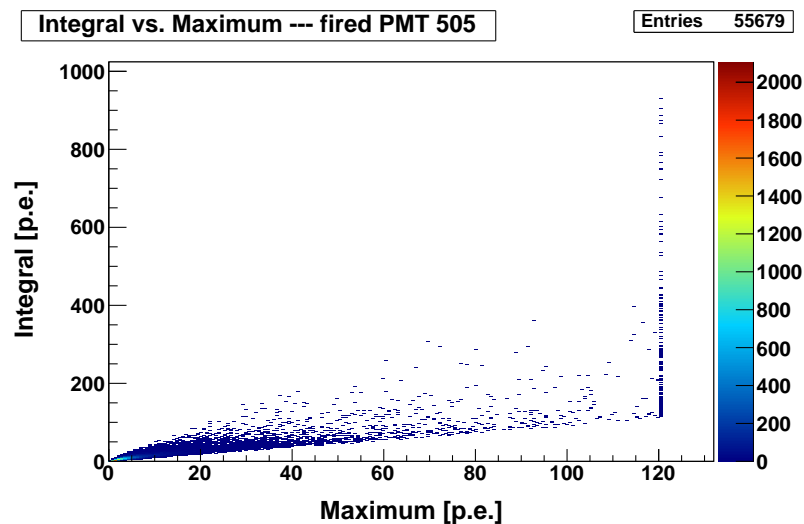
Figure 69: **PlotIntegralMaximum(<rootfile>,<PMT>):** To get an idea bout the linearity of the integral and the maximum, this function can be used. It creates a 2D-Plot of Integral vs. Maximum of one PMT. The maximal value for maximum is at around 120 p.e. due to the restrictions by the FADC, while the integral delivers much more informations.
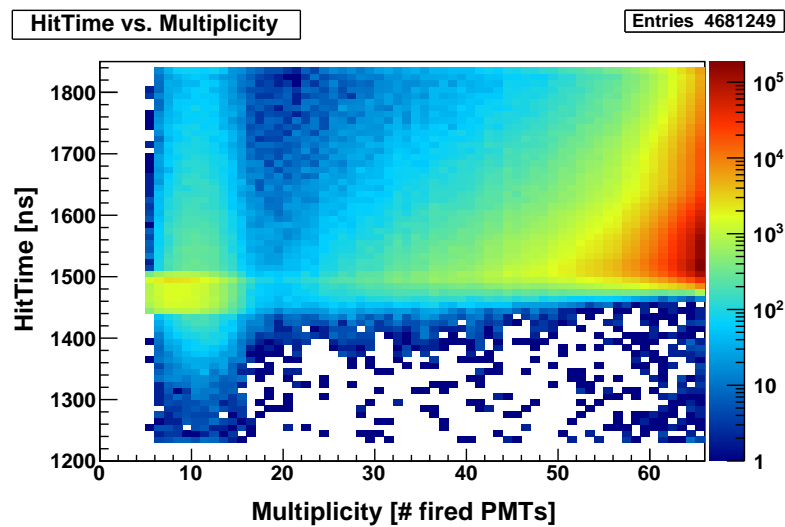
Figure 70: **PlotHitTimeMultiplicity(<rootfile>)**: A 2D-Plot is created, on x-axis is the number of fired PMTs (multiplicity), on y-axis the time, when the PMTs have fired. Here, one clearly sees a thick band at hitting times between 1440 ns and 1500 ns. The delayed trigger occurs at 1530 ns, so, this region is the region, where the coincident pulses occur. Of course, some small amount of pulses occur before the trigger time, and a lot of pulses occur after this time.
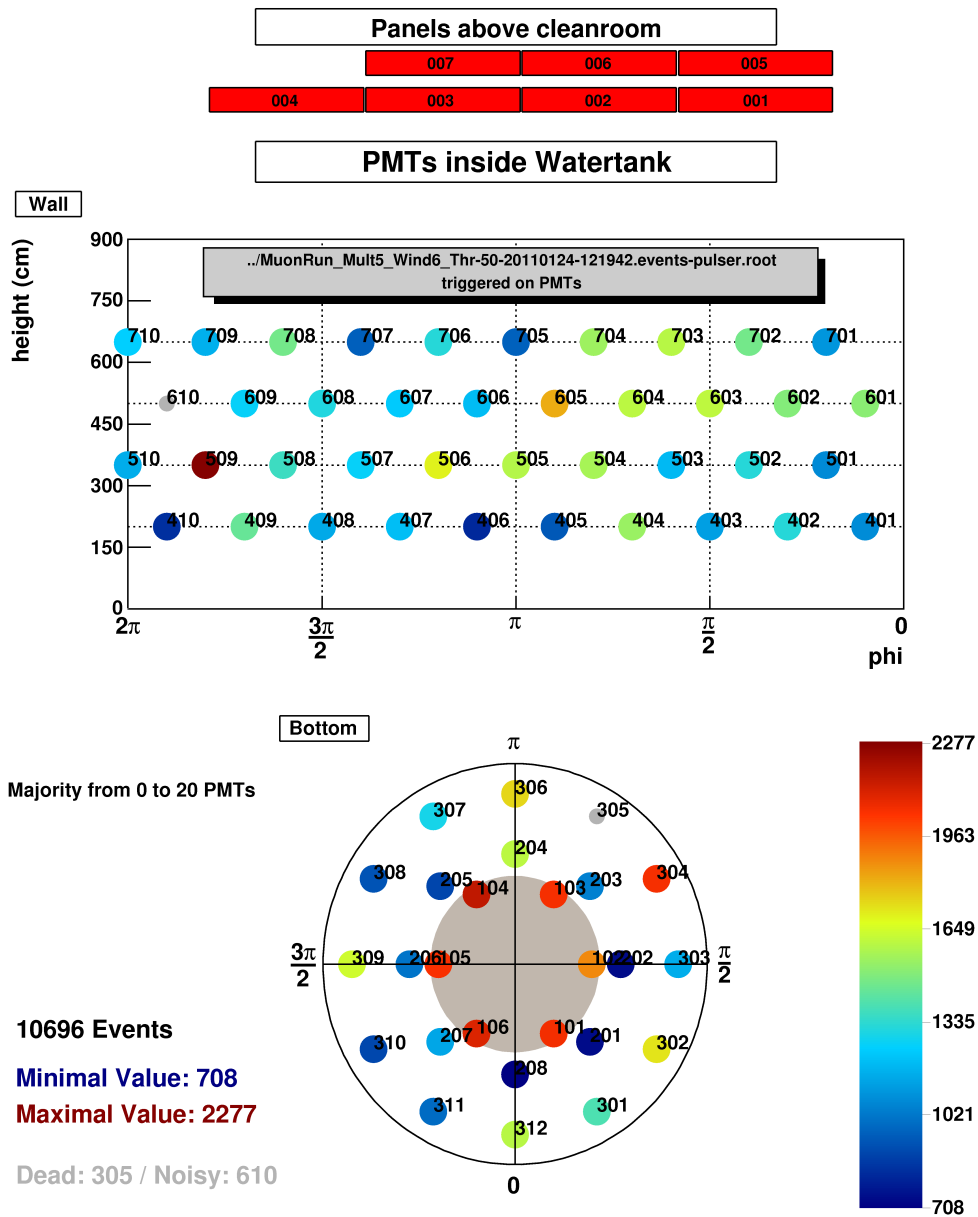
Figure 71: **PlotMulti(<rootfile>, <name of variable>, <lower multiplicity>,<upper multiplicity>)**: A muon map is created, the variable can be chosen between Integral, Maximum, the HitTime and the Boolean, if the PMT fired or not. Also cuts can be performed on the multiplicity. Here, one can see different behaviour of different PMTs. For this example, the Boolean information if the PMT fired or not was chosen. The multiplicity was set from 0 to 20. One sees, that the pillbox-PMTs fired relatively often. This is because the pillbox volume is relatively good separated from the rest. Thus, if a light producing event occurs in the pillbox, it is more likely that only a small fraction of all PMTs saw some light, namely one to six.

I.2   GERDA_3D-Plots

The second ROOT- file was developed, when the full setup of the plastic scintillator was available. It just contains a routine to create a 3D view of one event. A static plot, saved as *.png file is created (fig. 72), as well as two animated *.gif files. One animation shows the temporal development of the event, the second animation shows the full event in a rotation, examples of these movies can also be found at the website given in section I.3.

I.3   Web Site

As animations are not so easy to be included in a print out, examples of all the previously described animated *.gif files can be found on this web page:
`http://www.pit.physik.uni-tuebingen.de/jochum/dbd/veto_events_eng.html`
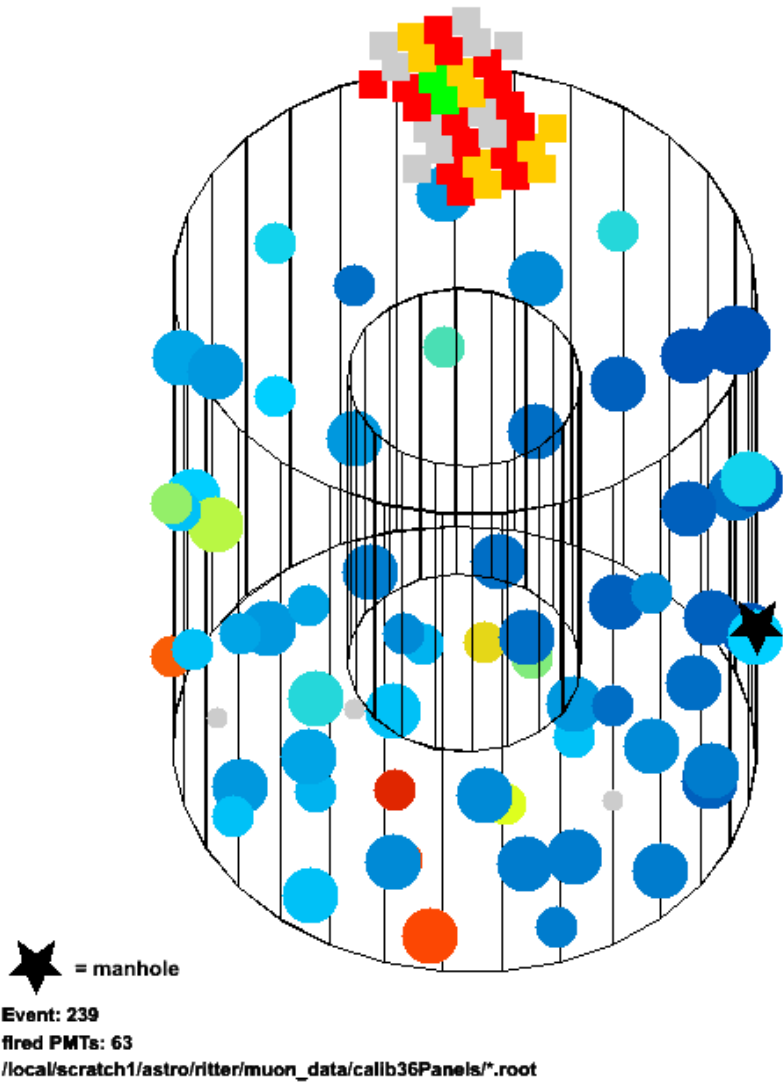
Figure 72: An example for a 3D view of a muon event is shown. The Cherenkov veto is indicated as a large cylinder, with the simplified cylinder for the cryostat inserted. Each PMT gets a colorized point, where the color represents the hit time and the size the amount of light. The plastic veto is indicated as squares, each square is one pixel, color indicates the amount of layer which have fired. One nicely sees, that 63 PMTs fired, and also two pixels.

II PMT list

The nomenclature of the installed PMTs is described in chapter 4.3.2. Here, a small table is given with all the information stored in the GERDA database.

Table 12: Summary of PMT data. [a]: Gain tested with LED; [b]: Only Gain of $1 \cdot 10^7$ possible; [c]: "water cable", damaged cable, no PMT installed; [d]: Voltage for wanted gain differ much from test in Tübingen and data from LNGS.

PMT number	Capsule serial	Volts @ $2 \cdot 10^7$ Gain measured ('09)	Volts @ 75-95 FADC Gain	exact FADC channels	DCTS @ a= $2 \cdot 10^7$ [CDS] given	DCTS @ a= $2 \cdot 10^7$ [CDS] measured ('09)	Splitterbox	HV card_slot	FADC num_channel
101[b]	30	1435	2150	41.5	3400	663.92	07	0_06	01_01
102	28	1480	1480	79.5	8200	4621.62	42	3_05	06_01
103	14	1635	1645	79.7		3662.93	35	2_10	05_01
104[a]	24	1430	1450	83.7	7000	3313.07	28	2_03	04_01
105[a]	69	1370	1380	78.7		2919.88	21	1_08	03_01
106	44	1400	1400	75.1	4200	1268.9	14	1_01	02_01
201	27	1740	1730		5300	1053.19	62	4_11	09_02
202[d]	51	1425	1750	77.9	7930	1204.8	55	4_05	08_02
203	48	1670	1710	79.9	7400	9084.56	48	3_11	07_02
204	17	1560	1560	87.0	7000	2067.17	41	3_04	06_02
205	76	1500	1500	84.7	2500	2718.14	34	2_09	05_02
206[a]	45	1700	1740	80.1	8400	2455.07	27	2_02	04_02
207	52	1540	1540	92.4	4500	1322.22	20	1_07	03_02
208	22	1610	1610	83.3	8800	2352.66	69	5_05	10_02
301	81	1630	1620	89.9	3700	2910.81	05	0_04	01_03
302	66	1930	1930	79.7	3600	3032.85	26	2_01	04_03
303	55	1750	1740	89.4	2750	3257.52	19	1_06	03_03
304[a]	33	1760	1770	85.0	3380	2794.46	13	1_00	02_02
305[c]	25	1590	1590		1100	2307.37	68	5_04	10_03
306	64	1880	1880	86.9	700	1250.04	61	4_10	09_03
307	40	1810	1810	90.4	2800	1514.74	06	0_05	01_02

PMT number	Capsule serial	Volts @ $2 \cdot 10^7$ Gain measured ('09)	Volts @ 75-95 FADC Gain	exact FADC channels	DCTS @ a= $2 \cdot 10^7$ [CDS] given	DCTS @ a= $2 \cdot 10^7$ [CDS] measured ('09)	Splitterbox	HV card_slot	FADC num_channel
308	70	1790	1790	79.6	8300	1172.12	54	4_04	08_03
309	82	1800	1800	94.7	8400	8602.6	47	3_10	07_03
310	63	1460	1460	81.4	2000	1981.83	12	0_11	02_03
311	60	1700	1700	77.3	5400	2167	40	3_03	06_03
312	13	1615	1615	84.2	8500	4597.52	33	2_08	05_03
401	43	1495	1495	86.2	7700	6991.62	60	4_09	09_04
402	3	1530	1530	84.7	8550	1931.67	53	4_03	08_04
403	57	1590	1590	79.2	1630	1584.79	46	3_09	07_04
404	47	1640	1640	91.5	1612	853.4	39	3_02	06_04
405	75	2100	2100	33.6	2800	652.775	32	2_07	05_04
406	9	1670	1670	94.5	2820	1451.14	25	2_00	04_04
407	78	1705	1705	83.7	7700	748.542	18	1_05	03_04
408	32	1890	1900	75.9	4000	812.975	11	0_10	02_04
409	72	1890	1890	88.6	500	806.933	04	0_03	01_04
410[a]	54	1600	1630	86.7	720	1879.72	67	5_03	10_04
501	56	1670	1670	87.7	2000	2995.32	03	0_02	01_05
502	4	1530	1530	86.3	6700	1866.13	66	5_02	10_05
503	31	1650	1650	90.1	1990	3490.44	59	4_08	09_05
504	20	1635	1635	89.9	2900	521.983	52	4_02	08_05
505	49	1500	1500	85.1	4360	1712.59	45	3_08	07_05
506	73	1615	1615	76.9	1200	831.93	38	3_01	06_05
507	23	1750	1750	75.5	8700	1378.7	31	2_06	05_05
508	68	1625	1625	79.2	2700	1572.43	24	1_11	04_05
509	12	1700	1690	87.9	2820	1568.36	17	1_04	03_05
510[a]	8	1640	1640	77.5	4200	2297.39	10	0_09	02_05
601	61	1520	1510	93.7	1300	2790.23	23	1_10	04_06
602	77	2080	2080	88.2	2400	2792.53	16	1_03	03_06
603[a]	34	1630	1650	81.1	8830	3415.07	09	0_08	02_06
604[a]	29	1630	1640	83.7	3290	3459	02	0_01	01_06

PMT number	Capsule serial	Volts @ $2 \cdot 10^7$ Gain measured ('09)	Volts @ 75-95 FADC Gain	exact FADC channels	DCTS @ a= $2 \cdot 10^7$ [CDS] given	DCTS @ a= $2 \cdot 10^7$ [CDS] measured ('09)	Splitterbox	HV card_slot	FADC num_channel
605	38	2050	2050	80.6	6600	3581.9	65	5_01	10_06
606	6	1610	1610	83.0	900	2358.4	58	4_07	09_06
607	58	1590	1590	79.7	3000	4951.06	51	4_01	08_06
608[a]	67	1800	1810	77.5	2600	1346.24	44	3_07	07_06
609[a]	37	1550	1560	78.9	8100	3359.7	37	3_00	06_06
610	36	1715	1725	77.3	5040	3478.8	30	2_05	05_06
701[a]	41	1870	1880	75.6	3300	3965.62	36	2_11	06_07
702	50	1770	1770	91.1	400	1471.97	29	2_04	05_07
703	10	1600	1600	91.9	8000	3281.16	22	1_09	04_07
704	11	1700	1700	86.6		5225.48	15	1_02	03_07
705	26	1540	1540	80.2	7700	5285.61	08	0_07	02_07
706[a]	71	1540	1560	82.2		5568.07	01	0_00	01_07
707	15	1995	1995	85.7	900	5865.88	64	5_00	10_07
708	46	1490	1480	89.3	1100	2636.8	57	4_06	09_07
709	35	1535	1535	87.9	8700	8085.81	50	4_00	08_07
710	42	1520	1520	92.7	9900	3879.97	43	3_06	07_07

Bibliography

[3Ma]   3M, *DF2000MA_ b.pdf*, VM2000 data sheet.

[3Mb]   3M, *S32 5 micrun glass bubbles*.

[Aal02]   C. E. Aalseth et al., *The Igex 76ge Neutrinoless Double-Beta Decay Experiment: Prospects for Next Generation Experiments*, Phys. Rev. **D65**, 092007 (2002).

[Abt04]   I. Abt et al., *A New Ge-76 double beta decay experiment at LNGS: Letter of intent*, hep-ex/0404039.

[Ack11]   N. Ackerman et al., *Observation of Two-Neutrino Double-Beta Decay in Xe-136 with EXO-200*, ArXiv e-prints (2011).

[AEE08]   Frank T. Avignone, III, Steven R. Elliott and Jonathan Engel, *Double Beta Decay, Majorana Neutrinos, and Neutrino Mass*, Rev. Mod. Phys. **80**, 481 (2008).

[Ahl93]   S. P. Ahlen et al., *Muon astronomy with the MACRO detector*, Astrophys. J. **412**, 301 (1993).

[Ang08]   G. Angloher, M. Bauer, I. Bavykina, A. Bento, A. Brown et al., *Commissioning Run of the CRESST-II Dark Matter Search*, 0809.1829, * Brief entry *.

[Arn08]   C. Arnaboldi et al., *Results from a search for the $0\nu\beta\beta-decay$ of ^{130}Te*, Phys. Rev. **C78**, 035502 (2008).

[Ash03]   V. D. Ashitkov et al., *Liquid argon ionization detector for double beta decay studies*, nucl-ex/0309001.

[Bak05]   A. M. Bakalyarov et al., *Results of the experiment on investigation of Germanium-76 double beta decay*, Phys. Part. Nucl. Lett. **2**, 77 (2005).

[Bar11a] A. S. Barabash, *75 years of double beta decay: yesterday, today and tomorrow*, 1101.4502.

[Bar11b] A. S. Barabash, *Double Beta Decay: Historical Review of 75 Years of Research*, Phys. Atom. Nucl. **74**, 603 (2011).

[Bar11c] A. S. Barabash et al., *Low background detector with enriched $^{116}CdWO_4$ crystal scintillators to search for double β decay of ^{116}Cd*, Journal of Instrumentation **6**, 8011 (2011).

[Ber05]   M.J. Berger, J.S. Coursey, M.A. Zucker and J. Chang, *ESTAR, PSTAR, and AS-TAR: Computer Programs for Calculating Stopping-Power and Range Tables for Electrons, Protons, and Helium Ions (version 1.2.3)*, online, U.S. National Institute of Standards and Technology, 2005, (accessed 27 September 2011) Available from: http://physics.nist.gov/Star.

[Bet36]   H.A. Bethe, Rev.Mod.Phys. **8**, 139 (1936).

[Bro08]   Il'ja N. Bronšejn, *Taschenbuch der Mathematik*, 7., vollst. überarb. und erg. aufl. Aufl., Deutsch, 2008.

[Bud09]   Dušan Budjáš, *Germanium detector studies in the framework of the GERDA experiment*, PhD thesis, Universität Heidelberg, 2009.

[CAEa]   CAEN S.p.A., *Technical information manual V895*, V895 Technical Information Manual.

[CAEb]   CAEN S.p.A., *Technical information manual V925*, V925 Technical Information Manual.

[CAEc]   CAEN S.p.A., *Technical information manual V976*, V976 Technical Information Manual.

[CAE02]   CAEN S.p.A., *Technical Information Manual V560*, V560 Technical Information Manual, 2002.

[CAE03]   CAEN S.p.A., *Technical Information Manual V265*, V265 Technical Information Manual, 2003.

[CAE08]   CAEN S.p.A., *Technical Information Manual A2818*, A2818 Technical Information Manual, 2008.

[CAE09]   CAEN S.p.A., *Technical Information Manual V2718, VX2718 and VN2738*, V2718, VX2718 and VN2738 Technical Information Manual, 2009.

[Che08]   Mark C. Chen, *The SNO+ Experiment*, 0810.3694.

[CK06]   A. Caldwell and K. Kröninger, *Signal discovery in sparse spectra: A Bayesian analysis*, Phys. Rev. D **74**, 092003 (2006).

[COB10]   *COBRA LNGS Annual Report*.

[Cos]   *cosmic-rays.jpg*, http://www.scifun.ed.ac.uk/card/card-left.html.

[CPE]   *chart_2006_4.jpg*, http://www.cpepweb.org/chart_2006_4.jpg.

[Dav02]   Raymond Davis Jr., *Nobel Lecture*, 2002, The Nobel Foundation.

[DKT85]   M. Doi, T. Kotani and E. Takasugi, *Double beta Decay and Majorana Neutrino*, Prog.Theor.Phys.Suppl. **83**, 1 (1985).

[ET a]   ET Enterprise Ltd., *9350KB.pdf*, 9350KB data sheet.

[ET b]   ET Enterprise Ltd., *9354KB.pdf*, 93504B data sheet.

[Fae11]   A. Faessler, *Double Beta Decay, Nuclear Structure and Physics beyond the Standard Model*, ArXiv e-prints (2011).

[Fre]   Kai Freund, PhD thesis, Universität Tübingen, in preparation.

[Fre11]   Kai Freund, private communication, 2011.

[GER]   *GERDA-Modell_web.jpg*, ttp://www.mpi-hd.mpg.de/gerda/index.html.

[GJK05] Andre de Gouvea, James Jenkins and Boris Kayser, *Neutrino mass hierarchy, vacuum oscillations, and vanishing U/e3/*, Phys. Rev. **D71**, 113009 (2005).

[Gru05]   Claus Grupen, *Astroparticle Physics*, 1. Aufl., Springer, 2005.

[Gui11]   V. E. Guiseppe for the Majorana Collaboration, *The Majorana Experiment*, ArXiv e-prints (2011).

[INF]   INFN, *Map of LNGS*, http://www.lngs.infn.it.

[Kap85]   J. S. Kapustinsky et al., *A fast timing light pulser for scintillation detectors*, Nuclear Instruments and Methods in Physics Research A **241**, 612 (1985).

[Kih11]   Thomas Kihm, private communication, 2011.

[KK01a] H. V. Klapdor-Kleingrothaus et al., *Evidence for Neutrinoless Double Beta Decay*, Mod. Phys. Lett. **A16**, 2409 (2001).

[KK01b] H. V. Klapdor-Kleingrothaus et al., *Latest Results from the Heidelberg-Moscow Double Beta Decay Experiment*, Eur. Phys. J. **A12**, 147 (2001).

[KK04]   H.V. Klapdor-Kleingrothaus et al., *Search for neutrinoless double beta decay with enriched 76Ge in Gran Sasso 1990-2003*, Physics Letters B **586**, 198 (2004).

[KKK06] H. V. Klapdor-Kleingrothaus and I. V. Krivosheina, *The evidence for the observation of 0nu beta beta decay: The identification of 0nu beta beta events from the full spectra*, Mod. Phys. Lett. **A21**, 1547 (2006).

[Kna09]   Markus Knapp, *Design, Simulation und Aufbau des GERDA-Myonvetos*, PhD thesis, Universität Tübingen, 2009.

[Lan10]   R.F. Lang et al., *Discrimination of recoil backgrounds in scintillating calorimeters*, Astroparticle Physics **33**, 60 (2010).

[Mac11]   Ana Amelia B. Machado, private communication, 2011.

[Maj37]   Ettore Majorana, *Teoria simmetrica dellélettrone e del positrone*, Nuovo Cimento (1937).

[Man08] W. Maneschg et al., *Measurements of extremely low radioactivity levels in stainless steel for GERDA*, Nuclear Instruments and Methods in Physics Research Section A: Accelerators, Spectrometers, Detectors and Associated Equipment **593**, 448 (2008).

[Mei10]   Georg Meierhofer, *Neutron capture on 76-Ge*, PhD thesis, Universität Tübingen, 2010.

[Mos05] M. Moszyński et al., *Characterization of CaWO4 scintillator at room and liquid nitro-gen temperatures*, Nuclear Instruments and Methods in Physics Research Section A: Accelerators, Spectrometers, Detectors and Associated Equipment **553**, 578 (2005).

[MP]   R. N. Mohapatra and Palash B. Pal, *Massive Neutrinos in Physics and Astrophysics*, 3 Aufl., World Scientific Publishing Company.

[Nak10] K. Nakamura et al., *Review of particle physics*, J. Phys. **G37**, 075021 (2010).

[NNDC08] Brookhaven National Laboratory National Nuclear Data Center, *NuDat (Nuclear Structure and Decay Data)*, March 18, 2008 2008.

[ORT]   ORTEC Advanced Measurement Technology, Inc, *Electronics Standards and Definitions*, Electronics Standards and Definitions.

[Oßw07] Claudia Oßwald, *Die Szintillationseigenschaften von einkristallinem CaWO4 bei unter-schiedlichen Temperaturen*, thesis (Zulassungsarbeit), Universität Tübingen, 2007.

[Pan07] L. Pandola et al., *Monte Carlo evaluation of the muon-induced background in the GERDA double beta decay experiment*, Nuclear Instruments and Methods in Physics Research Section A: Accelerators, Spectrometers, Detectors and Associated Equipment **570**, 149 (2007).

[Pov09] Bogdan Povh, *Teilchen und Kerne: eine Einführung in die physikalischen Konzepte*, 8. aufl. Aufl., Springer, Berlin, 2009.

[Sai]   Christof Sailer, PhD thesis, Universität Tübingen, in preparation.

[Sch11] Bernhard Schwingenheuer, *Ar42 concentration + background for runs 10+11*, GERDA collaboration meeting Feb. 2011, 2011.

[Shi08] Yu. Shitov, *Supernemo: A Next Generation Project to Search for Neutrinoless Double Beta Decay*, 0807.3078.

[Sin95] Balraj Singh, *Nuclear Data Sheets Update for A = 76*, Nuclear Data Sheets **74**, 63 (1995).

[Str04] Struck Innovative Systeme GmbH, *sis3300_ greta_ v110.pdf*, SIS 3300/3301 user manual, 2004.

[Str10] Christian Strandhagen, *Messung der Szintillationseigenschaften von CaWO4 bei tiefen Temperaturen*, diploma thesis, Universität Tübingen, 2010.

[Sum]   Summers Optical, *Lensbond*.

[SZ08]   Mark Shirchenko and Daniya Zinatulina, private communication, 2008.

[Wac]   Wacker Chemie AG, *SilGel 612 A & B*.

[Wei35] Carl Friedrich von Weizsäcker, *Zur Theorie der Kernmassen*, Zeitschrift für Physik **96**, 431 (1935).

List of Figures

List of Tables

Danke

An dieser Stelle bleibt mir nur noch, "Danke" zu sagen...

... meinen beiden Betreuern Prof. Dr. Josef Jochum und Prof. Dr. Peter Grabmayr, dafür, dass sie es mir überhaupt ermöglicht haben, an einem so interessanten Projekt mitzuarbeiten. Und dass sie immer zu erreichen waren, wenn ich mal eine Frage hatte.

... der ganzen GERDA-Kollaboration für all die interessanten, mitunter hitzigen Diskussionen während der Kollaborations-Treffen, aber auch für die vielen netten Abende, die wir gemeinsam am LNGS bei Arrosticini, Tiramisu und Wein hatten.

... Dr. Markus Knapp, Prof. Dr. Tobias Lachenmaier, Pia Lachenmaier, Claudia Oßwald, Sabine Schulze, Dr. Giuseppe Testa für die vielen Spieleabende! Das müssen wir unbedingt wieder öfter machen!

... Daniel Greiner, der zwar auch bei den anderen Freunden und Mitspielern aufgeführt werden müsste, sich aber eine extra Nennung verdient hat, weil er zu meiner frechen Frage, ob er mit mir Jungenschaft (und später dann Jugendkreis) machen würde nicht "nein" gesagt hat.

... meinen GERDA-Mitdoktoranden Dr. Georg Meierhofer, Kai Freund, Raphael Falkenstein und Alexander Hegai für die Mithilfe beim Einbau, die Übernahme der Aufgaben und die vielen anregenden Gespräche.

... to Dr. Bayarto Lubsandorzhiev, it was always a pleasure to discuss with you and learn from your experience.

... meinen (Ex-)Bürokollegen Andrea Hagen, Katharina von Sturm und Mikail Bolatekin, dass sie es mit mir ausgehalten haben, auch wenn ich mich mal wieder über meine eigene Programmierprobleme oder über dieses komische ROOT aufregen musste.

... allen anderen Kollegen und Freunde aus der AG Jochum: Michael Bauer, Gerhard Deuter, Sebastian Diebold, Dennis Dietrich, Marc Pfeifer, Markus Röhling, Klemens Rottler, Christof Sailer, Christopher Schmitt, Dr. Stephan Scholl, Lee Stokes, Christian Strandhagen und Igor Usherov-Marshak für die Kaffeerunden, die Gespräche, das Pub-Quiz, das Grillen, ...

... der Elektronik-Werkstatt mit ihrem Leiter Herrn Schreyer, die so manche knifflige Aufgabe super gelöst haben.

... der Feinmechaniker-Werkstatt mit ihren Leitern Herrn Brodbeck und Herrn Stockmaier, die ebenso häufig kleinere und größere Aufgaben von uns bekommen haben, und diese trotzdem schnell und zuverlässig erfüllt haben.